**Universidade do Minho**
Escola de Engenharia

Francisca Araújo Guedes Machado

# Low Intensity Focused Ultrasound Modulation of Neuronal Circuits Activity

outubro de 2019

Low Intensity Focused Ultrasound Modulation of Neuronal Circuits Activity
Francisca Araújo Guedes Machado
UMinho | 2019

**Universidade do Minho**
Escola de Engenharia

Francisca Araújo Guedes Machado

# Low Intensity Focused Ultrasound Modulation of Neuronal Circuits Activity

Dissertação de Mestrado
Mestrado Integrado em Engenharia Biomédica
Ramo de Eletrónica Médica

Trabalho efetuado sob a orientação do
**Professor Doutor Paulo Mendes Mateus Mendes**
e do
**Doutor Ricardo José da Silva Magalhã**

outubro de 2019

## DIREITOS DE AUTOR E CONDIÇÕES DE UTILIZAÇÃO DO TRABALHO POR TERCEIROS

Este é um trabalho académico que pode ser utilizado por terceiros desde que respeitadas as regras e boas práticas internacionalmente aceites, no que concerne aos direitos de autor e direitos conexos.

Assim, o presente trabalho pode ser utilizado nos termos previstos na licença abaixo indicada.

Caso o utilizador necessite de permissão para poder fazer um uso do trabalho em condições não previstas no licenciamento indicado, deverá contactar o autor, através do RepositóriUM da Universidade do Minho.

**Atribuição-NãoComercial-CompartilhaIgual**
**CC BY-NC-SA**

https://creativecommons.org/licenses/by-nc-sa/4.0/

# Acknowledgments

The successful completion of this work would not have been possible without the input of a number of people that through their skills, insight and motivation have certainly elevated the final result.

Firstly, I would like to thank Professor Paulo Mendes for the continuous guidance in the development of this master's dissertation as well as the confidence deposited in me. I would also like to thank Doctor Ricardo Magalhães for is support and availability.

Furthermore, I would like to thank Professor Nuno Sousa for welcoming me at the Life and Health Sciences Research Institute (ICVS), as well as allowing me to work in such a collaborative and positive environment which fosters constructive comments and enthusiasm in the pursuit of learning.

I would like to thank the Neurospin (CEA Saclay) research team, in particular Doctor Benoit Larrat for having received and accompanied me during this process.

A word of gratitude for the funding provided by the Foundation Callouste Goulbenkian (Project "Envelhecimento cognitivo saudável – proporcionar saúde mental no progresso biológico do envelhecimento").

I am deeply indebted to Doctor Patrícia Monteiro and Doctor Luís Jacinto for all their hard-working support and encouragement. Their contribution was twofold. Both from a technical and pedagogical standpoint that permitted the planning and execution of experimental protocols in the electrophysiology field. Also, their advices regarding the structure and scientific rigour during the composition of the project.

A special thank you to those closest to me, namely my family. To my Mother, Father, Brother and Godmother, for their unconditional love and care. Last but not least, a heartfelt thank you to Sérgio.

## STATEMENT OF INTEGRITY

I hereby declare having conducted this academic work with integrity. I confirm that I have not used plagiarism or any form of undue use of information or falsification of results along the process leading to its elaboration.

I further declare that I have fully acknowledged the Code of Ethical Conduct of the University of Minho.

# Resumo

O uso de ultrassons focados (FUS) corresponde a uma técnica de neuromodulação não invasiva que ganhou destaque nas últimas décadas devido à sua capacidade de modificar reversivelmente a atividade neuronal com alta precisão espacial. Como tal, FUS foi reconhecido como um forte candidato para a substituição de técnicas convencionais de neuromodulação, como a estimulação cerebral profunda (DBS) e a estimulação magnética transcraniana (TMS) no tratamento de doenças neurológicas humanas. Contudo, a falta de protocolos padronizados e de consenso na comunidade científica relativamente aos mecanismos responsáveis pelas respostas neuronais induzidas por FUS, representam barreiras críticas ao avanço desta técnica para ensaios clínicos.

O objetivo principal da presente dissertação de mestrado foi a implementação de um sistema de ultrassons capaz de fornecer ultrassons focados de baixa intensidade (LIFUS) a circuitos neuronais, utilizando fatias de cérebro *ex vivo*. Um protocolo experimental foi desenvolvido com base na literatura de neuromodulação por ultrassons, de forma a permitir o estudo de uma ampla gama de parâmetros de sonicação, juntamente com os resultados subsequentes da modulação na atividade neuronal.

Com o intuito de verificar as alterações induzidas pelos ultrassons na atividade elétrica dos neurónios alvo, um novo protótipo de registo eletrofisiológico, baseado em tétrodos, foi desenvolvido para registar a atividade neuronal extracelular em fatias de cérebro de forma econômica e reproduzível. Adicionalmente, um novo algoritmo de classificação de disparos neuronais semi-supervisionado foi desenvolvido para isolar neurônios, possibilitando a análise da resposta de neurónios individuais ao LIFUS. O novo protótipo e o algoritmo de classificação foram validados com estimulação optogenética, utilizada como controlo positivo para verificar a capacidade do novo protótipo de registar alterações na atividade evocada por estímulos externos.

Em suma, este estudo forneceu uma base de engenharia, desde a especificação e instalação de um novo sistema de ultrassons até ao desenvolvimento de novas ferramentas para registar e analisar a atividade neuronal em resposta a estímulos externos – para futuras investigações sistemáticas e reproduzíveis dos efeitos neuromodulatórios do LIFUS. Este estudo será essencial para promover o LIFUS como uma via de tratamento de distúrbios neurológicos ou psiquiátricos humanos.

**Palavras-chave**: neuromodulação, ultrassons, ultrassons focados, eletrofisiologia, tétrodos, classificação de disparos neuronais.

# Abstract

Focused ultrasound (FUS) is a non-invasive neuromodulation technique which has gained momentum over the past few decades due to its capability of reversibly modifying neuronal activity with high spatial accuracy. Therefore, FUS has been remarked as a strong candidate for replacing conventional neuromodulation techniques such as deep brain stimulation (DBS) and transcranial magnetic stimulation (TMS) in the treatment of human neurologic diseases. Nonetheless, the lack of standardized protocols and consensus in the scientific community regarding the mechanisms behind FUS-induced neuronal responses represent critical barriers to the advancement of this technique into clinical trials.

The primary goal of this master's dissertation was to implement an ultrasound system capable of delivering low intensity focused ultrasound (LIFUS) to neuronal cells in, *ex vivo* rodent brain slices. An experimental protocol was developed based on an extensive revision of ultrasound neuromodulation literature, that allows the study of a broad range of sonication parameters and the subsequent modulation outcomes on neuronal activity.

In order to verify the ultrasound-induced modifications in the electrical activity of the targeted neurons, a new electrophysiology recording prototype, based on tetrodes, was developed to record extracellular neuronal activity in brain slices in a cost-effective and reproducible manner. Moreover, a new semi-supervised spike sorting algorithm was developed to isolate single neurons, allowing the analysis of the individual neuron's response to LIFUS. Both the new prototype and spike sorting algorithm were validated with optogenetic stimulation, used as a positive control to verify the prototype's ability to record alterations in evoked activity by external *stimuli*.

In conclusion, this study provided an engineering foundation, from the specification and installation of a new US system to the development of new tools to record and analyze neuronal activity in response to external *stimuli* – for future systematic and reproducible investigations of LIFUS neuromodulatory effects. In particular, the developed framework will allow future promising research, including the unveiling of possible mechanisms of action for LIFUS on neuronal activity but also the optimization of sonication parameters in order to obtain safer and controllable neuromodulation. This research will be essential in order to advance LIFUS as a route for the treatment of human neurologic or psychiatric disorders.

**Keywords**: neuromodulation, ultrasound, focused ultrasound, electrophysiology, tetrodes, spike sorting.

# Table of Contents

# List of Figures

# List of Tables

# List of Acronyms

**AD** Alzheimer's Disease.

**AP** Action Potential.

**BLS** Bilayer Sonophore.

**BBB** Blood Brain Barrier.

**BOLD** Blood Oxygen Level Dependent.

**CNS** Central Nervous System.

**CAP** Compound Action Potential.

**CW** Continuous-Wave.

**DBS** Deep Brain Stimulation.

**DC** Duty Cycle.

**DF** Duty Factor.

**EEG** Electroencephalography.

**EMG** Electromyography.

**ET** Essential Tremor.

**FF** Far Field.

**FUS** Focused Ultrasound.

**FDA** Food and Drug Administration.

$f$ – Frequency.

**fMRI** Functional Magnetic Resonance Imaging.

**GBD** Global Burden of Disease.

**HIFUS** High Intensity Focused Ultrasound.

**HH** Hodgkin-Huxley.

**LFP** Local Field Potentials.

**LIFUS** Low Intensity Focused Ultrasound.

**MRI** Magnetic Resonance Imaging.

**MI** Mechanical Index.

**MEA** Microelectrode Array.

**MEPs** Motor Evoked Potentials.

**MRgFUS** MRI-Guided Focused Ultrasound

**MUA** Multi-Unit Activity.

**NF** Near Field.

**NICE** Neuronal Intramembrane Cavitation Excitation.

**N** Number of Cycles per Pulse.

**OCD** Obsessive-compulsive Disorder.

**PD** Parkinson's Disease.

**PNS** Peripheral Nervous System.

**PD** Pulse Duration.

**PII** Pulse Intensity Integral.

**PRF** Pulse Repetition Frequency.

**PRP** Pulse Repetition Period.

**PW** Pulsed Wave.

**rTMS** Repetitive Transcranial Magnetic Stimulation.

**SNR** Signal-to-Noise Ratio.

**SUA** Single-Unit Activity.

**SSEP** Somatosensory Evoked Potential.

$\mathbf{I_{SPPA}}$ Spatial Peak, Pulse-Average Intensity.

$\mathbf{I_{SPTA}}$ Spatial Peak, Time-Average Intensity.

$\mathbf{I_{TA}}$ Temporal-Average Intensity.

**tDCS** Transcranial Direct Current Stimulation.

**tFUS** Transcranial Focused Ultrasound.

**TMS** Transcranial Magnetic Stimulation.

**US** Ultrasound.

**VNS** Vagus Nerve Stimulation.

**VEP** Visual Evoked Potentials.

# Chapter 1

# Introduction

## 1.1. Neural Signaling

The vertebrate nervous system can be organized into two major subdivisions: central and peripheral nervous systems (CNS and PNS respectively). The CNS includes the nerves in the brain, brainstem, cerebellum and spinal cord (structures protected within the skull and vertebral canal of the spine); while the PNS comprises all the remaining nerves in the body that exist outside these structures, carrying information between the CNS and the body (muscle, glandular cells and other organs) [1].

The nervous system is composed of two types of cells: neurons and the neuroglial cells. Neurons are highly specialized, and excitable cells, capable of receiving, generating and propagating electrical impulses (action potentials or spikes) throughout the nervous system. This is possible due to the presence of ion channels (macromolecular proteins) in the neuron's plasma membrane, that allow the selective passage of ions and subsequent generation of an action potential (AP) or train of spikes. Glial cells are structural and functional support cells that contribute to neuronal physiology [1, 2].

Neurons can be classified according to morphological, connectional, molecular and physiological characteristics and consequently, grouped into cell-types which enables the systematic study of neuronal circuits that perform a certain role. Therefore, these nerve cells can be grouped according to their function: afferent (transmit sensory information towards the CNS), efferent (transmit information from the CNS to the body) and interneurons (regulate the activity of a neuronal circuit, within a small spatial area). Additionally, neurons also can be classified based on which neurotransmitters they synthesize and/or release. Neurotransmitters are neurons' secretory product involved in impulse transmission over the nervous system. The most commonly neurotransmitters found in the mammalian brain are glutamate (excitatory amino acid) and gamma-Amynobutyric acid (GABA) (inhibitory amino acid), among others.

Neurons are generally characterized by three major regions: (1) - the soma (or cell body) that holds the cell's nucleus and is responsible for ensuring the structural integrity and function of a neuron; (2) -

dendrites, which are specialized extensions from the cell body that arborize profusely and transmit information from the dendritic arborization towards the soma; (3) - axon, which is also a specialized extension from the cell body that conducts information away from the soma through its terminals, allowing the communication with other neurons. Moreover, the main receptive area of neurons comprises the cell body and dendrites, that receive multiple synaptic contacts from other neurons; while the main transmission area is composed by the neuron's axon [1, 2]. Figure 1 depicts the typical neuron's morphology, in both Purkinje (one of the largest neurons in the brain, found in the cerebellum) and pyramidal cells (excitatory cells found in the cerebral cortex, hippocampus and amygdala regions).

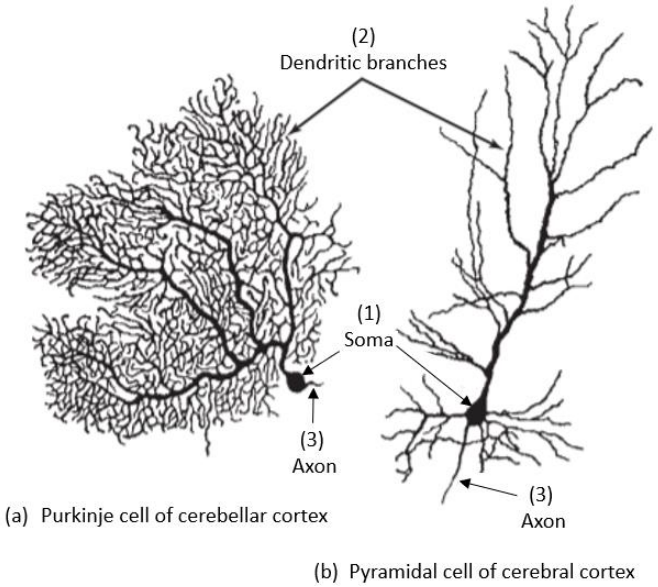


Figure 1 – Morphology of neurons with distinct shapes, adapted from [1]. (a) – morphology of a Purkinje cell of the cerebellar cortex (left). (b) – morphology of a pyramidal neuron of the cerebral cortex (right).

In the CNS, neurons communicate with each other through synapses, which correspond to interneuronal connections where information is conveyed from one cell to the other (typically between the axon of a neuron and the dendrite or soma of the target cell – axodendritic and axosomatic synapses, respectively). Hence, the transmission and processing of information in the nervous system are conducted through neuronal circuits, i.e., neurons connected together.

Synapses can be distinguished as of electrical and chemical nature. Electrical synapses (or gap junctions) enable the direct propagation of the electrical signals without the need of chemical transmitters, but through a mechanical and electrical junction between two extremely close neurons. Although less frequent than chemical synapses, electrical synapses result in a fast and bidirectional transmission, where the ionic current (generated by the propagation of the action potential) can flow in both directions over

the gap junction. In turn, chemical synapses are morphologically characterized by a presynaptic nerve terminal, synaptic cleft (space between the connected cells) and a postsynaptic membrane (formed by the dendrites or cell body of the target cell) (Figure 2). In this example, the propagation of an action potential to the axon terminals induces the depolarization of the presynaptic terminal and consequently, results in the influx of calcium ions ($Ca^{2+}$) through voltage-gated channels and in the generation of an action calcium potential, which can trigger the secretion of neurotransmitters (exocytosis) into the synaptic cleft. Next, the released neurotransmitters activate the receptors of the postsynaptic neuron's membrane, causing the influx of ions and subsequent modification of the membrane potential of the postsynaptic cell. Figure 2 portrays the multiple steps of chemical synapses, where the information is conveyed between the presynaptic terminal and the postsynaptic cell through the release of neurotransmitters that activate the opening and closing of ion channels, depolarizing the postsynaptic cell [2, 3].

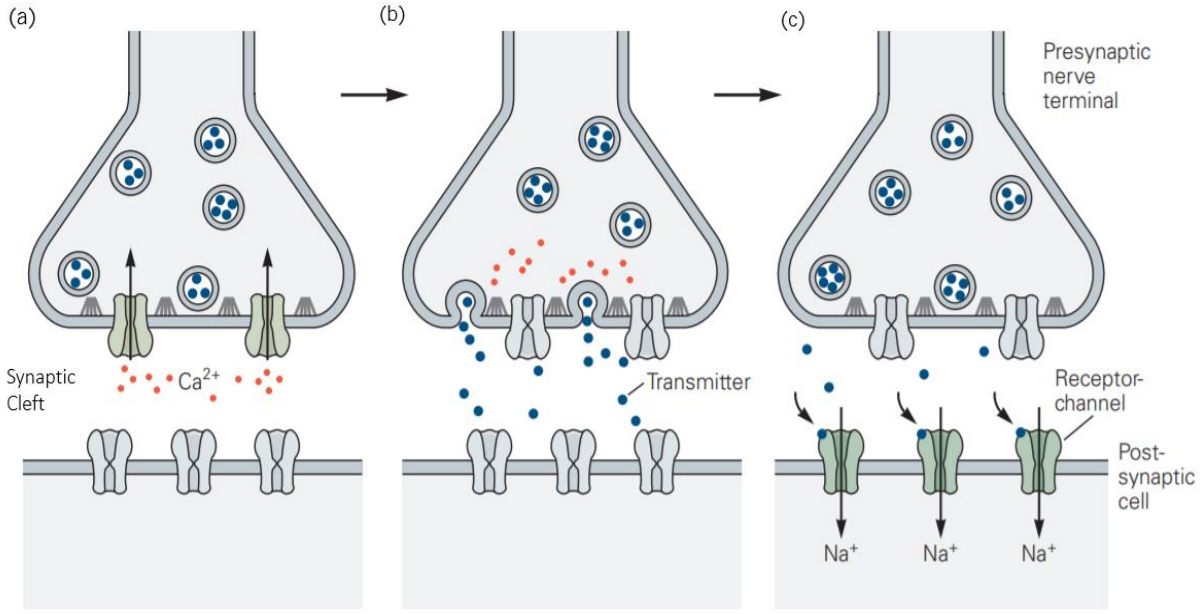


Figure 2 – Stages of chemical synapses, adapted from [4]. (a) - Influx of $Ca^{2+}$ in the presynaptic nerve terminal. (b) – Secretion of neurotransmitters into the synaptic cleft. (c) – Binding and recognition of neurotransmitters by the postsynaptic cell's receptors, leading to the influx of ions and depolarization of the postsynaptic cell.

### 1.1.1. The Resting Membrane Potential and Action Potential

The potential across the neuron's plasma membrane is generated by differential distributions of ions between the intracellular and extracellular environments, in particular as a result of unequal concentrations of sodium ($Na^+$) and potassium ($K^+$) ions, maintained through the opening and closing of ionic channels of the cell's membrane [1, 2].

In the absence of a stimulus, when the neuron is at rest it generates a potential denominated as resting membrane potential, predominantly determined by the movement of $K^+$, $Na^+$ and $Cl^-$ through passive ion channels. The ions are moved according to their concentration gradient to maintain a constant distribution of ions across the membrane and consequentially, the equilibrium potential (or Nernst equilibrium potential), in which the ionic flux in one direction (as a result of diffusion forces) is equal to the one in the opposite direction (due to electric forces). This equilibrium potential can be calculated through the Nernst equation (Equation 1 [1]), where the membrane potential by which any ion is at equilibrium is influenced by its concentration outside the cell ($[ion]_o$) and inside the cell ($[ion]_i$) , as well as by other factors (gas constant – $R$, temperature – $T$; valence of the ion – $z$; Faraday's constant – $F$).

$$E_{ion} = \frac{RT}{zF} . \ln\left(\frac{[ion]_o}{[ion]_i}\right) \quad (1)$$

The resting membrane potential is negative and quantitatively characterized between −60 and −80 mV inside versus outside, considering that these values are very close to the $K^+$ Nernst potential to which the membrane is predominantly permeable (the intracellular concentration of $K^+$ is much higher in comparison to other ions). The cell's membrane is least permeable to $Na^+$, yet the passive diffusion of $Na^+$ into the cells leads to the modification of the membrane potential to a slightly positive one in comparison to the $K^+$ Nernst potential; these cation influx is later counterbalance by the active efflux of $Na^+$ and influx of $K^+$ to the intracellular space by the $Na^+$–$K^+$ pump, leading to hyperpolarization and active maintenance of the resting membrane potential [1, 2].

Action potentials are generated when a stimulus-surpasses a certain intensity threshold, leading to the depolarization of the membrane of excitable neurons. This stimulus can result from the propagation of synaptic information (i.e. electrical current generated by an action potential initiated in a neuron and propagated into another through electrical or chemical synapses) or electrical currents applied experimentally, for example. During depolarization, the $Na^+$ permeability is increased rapidly and transiently, leading to the activation of $Na^+$ voltage-gated channels and a large positive ion influx. Therefore, the membrane potential becomes more positive, producing the rising phase of the AP curve illustrated in Figure 2 (a). This is followed by repolarization, in which a slow and prolonged increase in $K^+$ permeability, as well as the activation of $K^+$ voltage-gated channels occurs as to restore the membrane potential to its resting state. During the falling phase of the AP, the $Na^+$ voltage-gated channels are inactivated, and a brief period of hyperpolarization occurs , where the membrane potential becomes more

negative than its resting state, as a result of the active efflux of positive ions ($K^+$). Once the $K^+$ channels close, the membrane potential is restored to its resting state through the $Na^+$–$K^+$ pump [2, 3].

The generation of action potentials and the dynamics of membrane currents can be described according to the model developed by Hodgkin-Huxley, illustrated in Figure 2 (b). In this model, the membrane's lipidic bilayer is represented as a capacitor ($C_m$), considering that the membrane is enclosed by two conductive media (intracellular and extracellular spaces); while the opening and closing of $Na^+$ and $K^+$ voltage-dependent ion channels are characterized by the conductances $g_{Na}$ and $g_K$. The Nernst equilibrium potential for each ion is represented by the voltages $E_{Na}$ and $E_K$. Hence, if a current $\mathrm{I_t}$ (electrical stimulus) is applied to an excitable membrane, it may result in the accumulation of charge or the leak of current through the membrane's channels. These leak channels are characterized by the voltage-independent conductance $g_L$ and voltages $E_L$ This model assumes that the cell is isopotential (uniform membrane potential throughout the whole cell) [5].

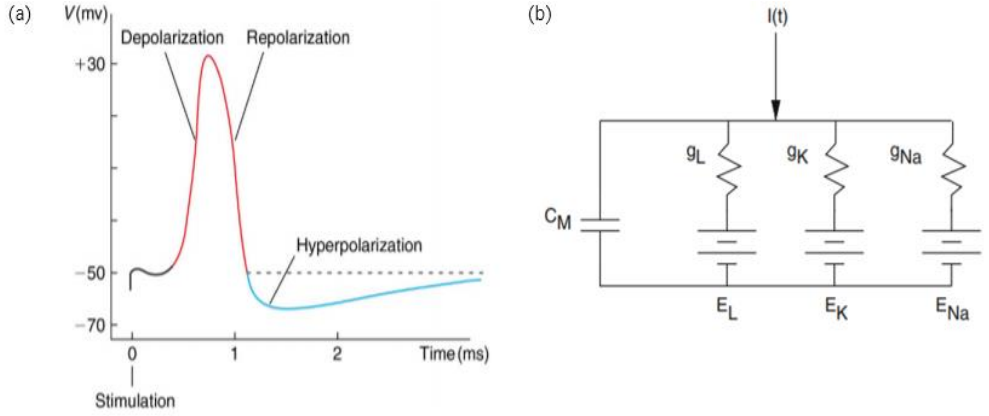


Figure 3 – Action potential. (a) – Action potential of the giant axon of a squid in response to stimulation (depolarizing current pulse), adapted from [2]. (b) – Equivalent circuit of the model developed by Hodgkin and Huxley concerning action potential generation, according to the obtained observations from the squid giant axon, adapted from [5].

Immediately after the generation of an action potential by a neuron there is a refractory period, which can be characterized as an absolute or relative. In the absolute case the spiking neuron is inexcitable regardless of the supplied ionic current while on the relative case the neuron requires an increased flow of ionic current in order to generate a second action potential, i.e., it presents a higher firing threshold. The absolute refractory period results from the inactivation of the $Na^+$ voltage-gated channels; whereas the relative refractory period arises after the membrane hyperpolarization and the absolute refractory period (when some of the $Na^+$ voltage-gated channels reopen as a response to a

second depolarization). The refractory period influences the conduction of the electric impulse, preventing its reverberation and thus, the action potentials are propagated unidirectionally in the axon terminals [1].

Information is therefore transmitted over the nervous system by the propagation of action potentials through the neuron's dendrites and axons. The rate of impulse conduction is influenced by myelination, i.e., by the coating of the axon with myelin (multiple layers of glial membranes) which functions as an electric insulator. Therefore, myelinated neurons are characterized by high impulse propagation velocities, being less prone to the occurrence of current leaks through the axon and thus, the distance by which the electrical impulse is propagated increases without amplitude reduction [1, 2] .

### 1.1.2. Electrophysiology

The electric activity of nerve cells and neuronal populations can be monitored and recorded by electrophysiology techniques in multiple brain regions, enabling the classification of neurons and the functional study of single neurons or neuronal ensembles. Electrophysiology techniques can be employed for the analysis of neurons in both *in vitro* (cell cultures and *ex vivo* brain slices) and *in vivo* models (intact brain in animal models), facilitating not only the assessment of the activity of ion channels in isolated neurons but also a better understanding of the influence of the neuronal ensemble activity on responses to complex stimulus or animal behavior, for example. Furthermore, in combination with neuromodulation techniques (later explored in subchapter 1.2), electrophysiology studies also allow the monitoring and analysis of the evoked activity of neurons, as a response to the delivery of an external stimulus [6].

Electrophysiology techniques can be distinguished according to the position of the recording device (electrode) in relation to the studied neural cell or ensemble (Figure 4): (1) – intracellular recording, where the electrode is placed inside the target cell; (2) – patch-clamp recording, in which the electrode is positioned close to the target neuron's membrane, forming a high-resistance seal with a patch of the membrane, allowing the study of single ion channels; (3) – extracellular recording, where the electrode(s) is(are) placed in proximity to the target neuron.

Additionally, extracellular signals can be recorded by single or multiple electrodes, namely by measuring the potential difference between the recording electrode's tip and a reference electrode (placed in a distant position in comparison to the recording site). These measurements can then be analyzed to reach a further comprehension of the mechanisms behind the generation of extracellular fields from local neural circuits.

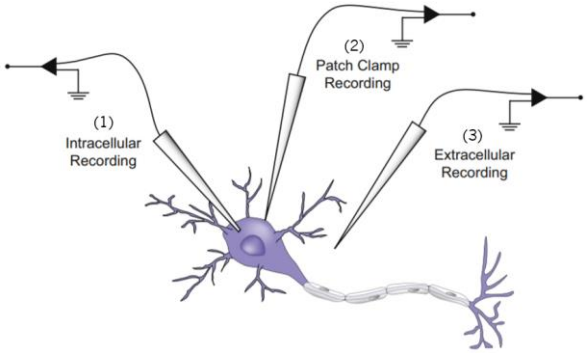


Figure 4 – Electrophysiology techniques adapted from [6]. (1) - intracellular recording. (2) - patch clamp recording. (3) - extracellular recording.

Extracellular signals are typically separated into two spectra: local field potentials (LFP) and multi-unit activity (MUA). LPF corresponds to the low-frequency component (below 100 Hz) of the recorded signal, composed by a myriad of cellular processes which change membrane voltage including, but not limited to, synaptic activity, subthreshold oscillations and distant spiking activity of a neighboring local population to the recording electrode; while the MUA represents the high-frequency component (from 300 up to 6000 Hz) of the raw signal, namely the spiking activity (with potential discriminable and sortable spikes) of a local population in proximity to the recording electrode. Furthermore, the recording of a neuronal population provides spatiotemporal information that enables the isolation of individual neuron's (also termed single units) activity through spike sorting algorithms and the characterization of its spontaneous or evoked activity [6, 7].

The use of several electrodes to measure extracellular activity in multiple sites can be accomplished by means of tetrodes, microelectrode arrays (MEAs) and silicon probes (Figure 5). Tetrodes correspond to four microwires twisted together, capable of recording the activity of multiple neurons with low cost, comparatively to the remaining electrode technologies. MEAs are high-density electrode arrays which can be both manufactured by the alignment of several microwires in a matrix configuration or through silicon microtechnology and metal–oxide–semiconductor (CMOS) technology (which enables the compacted combination of recording electrodes with integrated circuits). MEAs are characterized by stable mechanical and geometric properties. Alike MEAs, silicon probes are also fabricated through silicon microtechnology and typically exhibit a linear arrangement of electrode sites along a shank (or multiple shanks) [6, 8]. Planar CMOS arrays are typically used in *ex-vivo* slice electrophysiology while tetrodes, silicon arrays and probes are typically used in *in-vivo* animal model experiments.

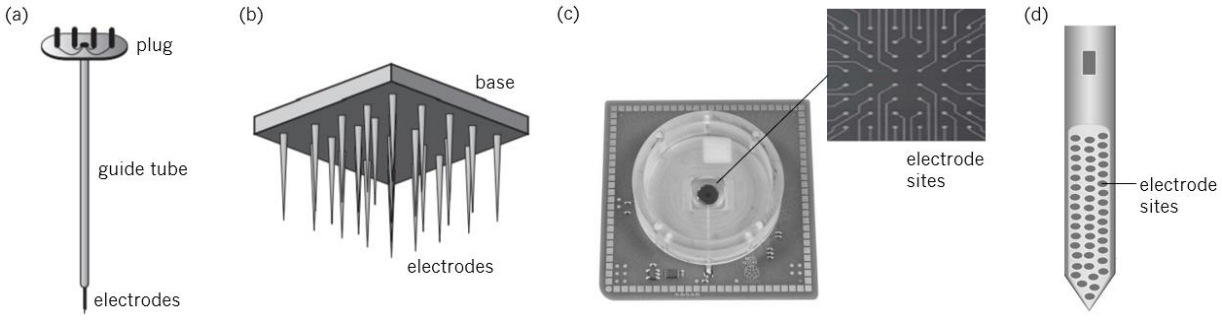


Figure 5 – Recording electrodes, adapted from [6, 8]. (a) – tetrode. (b) – 3D silicon microelectrode array used in vivo models (UTAH electrode array), fabricated by silicon microtechnology. (c) – planar microelectrode array used in vitro models fabricated by CMOS technology. (d) - silicon probe tip.

Regardless of the recording technology used, the impedance of the recording electrode/electrode site is a main limiting factor to obtaining good signal-to-noise ratio (SNR) recordings from extracellular activity. The impedance ($Z$) of an electrode is a measure of both its electrical resistance ( $R$) and reactance ($X$) – which includes inductive ($X_L$) and capacitive ($X_C$) reactance. In particular, $R$ is characterized by factors such as the electrical resistivity, length and the cross-sectional area (which is equivalent to diameter) of the wire (Equation 2 and 3 [9]). A smaller diameter implicates a reduced surface area of the exposed tip by which current can flow, resulting in a high resistance and thus in a high impedance electrode (> 1 MΩ).

$$Z = R + jX\ , X = X_L + X_C \qquad (2)$$

$$R = \rho \frac{l}{A}\ (\Omega) \qquad (3)$$

Regarding extracellular recordings, smaller diameter electrodes (12 μm) offer good unit isolation by restricting the recording area to a few proximate neurons, requiring a close distance to the cells' membrane in order to record its activity. However, these measurements are affected by thermal noise (which is proportional to impedance) and through the activity of distant neurons to the recording site (background activity), which can be superimposed on the signal of interest, contributing to a low signal-to-noise ratio (SNR) and to a challenging signal analysis [10, 11]. Nevertheless, electrodeposition of conductive metals to the electrodes can help improving the SNR and appropriate grounding/referencing of the complete system can reduce the influence of noise sources.

## 1.2. Neuromodulation Techniques

Neuromodulation techniques involve the use of electric, chemical, magnetic, acoustic or photonic stimulation through implantable or non-implantable devices, as to modify (excite or suppress) the activity of specific neurons, neuronal networks or functions. Several neuromodulation techniques have been employed with therapeutic and research purposes, in particular for the treatment of neurological or psychiatric disorders as well as for the functional study of neurons and neuronal networks of the CNS and PNS, respectively.

One of the most commonly employed neuromodulation techniques since the nineteenth century is Deep Brain Stimulation (DBS), which in human trials delivers controlled electric impulses to the brain using surgically implanted electrodes, connected to a pulse generator (pacemaker-like device) positioned subcutaneously in the patient's chest. This method has proven to be a non-pharmacotherapeutic option for difficult-to-treat essential tremor (ET), PD, dystonia and, was consequently acknowledged by the United States Food and Drug Administration (FDA) as a treatment for such neurologic diseases (1997, 2002 and 2003, respectively) [12]. Medtronic DBS systems have also been FDA approved as therapy devices for reducing symptoms in patients with drug-resistant OCD and epilepsy (2009 [13] and 2018 [14], respectively). Despite its low rates of mortality and morbidity, the need for invasive surgery to implant electrodes into deep brain regions makes it a less attractable neuromodulation procedure, presenting acute safety risks like intracranial hemorrhage, hardware-related infections and malfunctions [15].

Incompatibility issues with imaging techniques such as MRI may also arise with concurrent DBS, since the electromagnetic fields of the MR-scanner can interfere with the electrodes during the stimulation process, potentially leading to heating and subsequent edema in the neighboring cells to the electrodes. However, a few studies have proven that with the right safety measures, MRI examinations can be carried out without producing electrical damage or other related side effects [16, 17]. Yet another drawback of DBS is its spatial specificity, i.e., the extent of the stimulation site, that can vary between the order of several micrometers or millimeters, depending on factors such as the electrodes size, geometry, placement and polarity as well as the stimulation parameters (*stimuli* frequency and duration). Moreover, since the brain is not a homogenous conduction medium (anisotropic), the distribution of the electric field can be altered and difficult to predict, which can lead to the co-activation of neighboring cells to the targeted brain region [18].

Electric neuromodulation can too be achieved with vagus nerve stimulation (VNS), which intermittently stimulates the left vagus nerve (less likely to provoke bradycardia since it conducts fewer

fibers to the heart in comparison to the right vagus nerve) through surgically attached electrodes, connected to a pulse generator embedded in the patient's chest. This technique was FDA approved in 1997 as a therapy for epilepsy, as to suppress the frequency of partial-onset seizures of patients of 12-year-old or more and, in 2005 for the treatment of major depressive disorder (MDD) [19]. Later on, with the intuit of removing the need for surgical intervention and its inhering risks, transcutaneous VNS (tVNS) was developed as a non-invasive technique for stimulating the auricular branch of the vagus nerve using surface electrodes (placed in the patient's external ear) [20].

Likewise, Transcranial Magnetic Stimulation (TMS) has demonstrated to be a successful treatment for diseases as medication-resistant depression [21], and is being studied for the treatment of epilepsy, OCD, and among other disorders [22, 23]. TMS resorts to electromagnetic induction by placing an insulated electromagnetic coil in the patient's scalp, which generates a strong pulsating magnetic field (delivered with minimal impedance through the skull), which in turn induces electrical currents in the brain. Single pulses of induced electric current can depolarize brain regions and generate action potentials, whereas a long train of pulses – repetitive TMS (rTMS) - can promote a transient modulation of cortical excitability of the targeted areas and other functional connections, as well as motor responses. Alike DBS, the distribution of the generated electric field is also affected by the nonuniformity of the conduction medium (brain tissue), being that the induced currents are also influenced by the coil positioning and neuronal orientation [24, 25].

Transcranial direct current stimulation (tDCS) is another non-invasive neuromodulation technique, that operates through a saline-soaked pair of surface sponge electrodes (anode and cathode), which induce weak direct currents (DC) (typically under 1 mA) in the brain and consequentially, a prolonged and transient modulation of cerebral cortical functions. Contrary to TMS, rather than evoking action potentials, this method alters the discharge threshold and synaptic strength by polarizing the membrane potential of nervous cells, considering that neuronal excitability is increased by anodal stimulation (depolarization) and decreased by cathodal stimulation (hyperpolarization). The neurostimulation success is affected by parameters such as the current density, stimulation duration as well as the electrodes' position and polarity [26, 27].

Both TMS and tDCS represent non-invasive and safe approaches for neurostimulation; nonetheless, they are hindered by a diminished penetration in deep brain regions as well as a low spatial resolution (on the order of centimeters); considering that the intensity of the magnetic and electric field decreases with a rise of distance between the targeted tissue regions and the stimulation devices (coil and surface

electrodes, respectively) [18, 27]. A few compatibility issues can also arise by the simultaneous use of an electromagnetic coil and MRI, in specific challenges such as the positioning of the TMS system inside the MR-scanner environment and possible interactions between the MR coil and the TMS device during image acquisition. Additionally, TMS also presents a high-power consumption, high cost and can potentially provoke adverse effects such as seizures. In turn, tDCS can provoke side effects such as skin lesions and burns, considering that these reactions are determined by the type of stimulation (anodal or cathodal) along with the *stimuli* intensity and duration [28, 27].

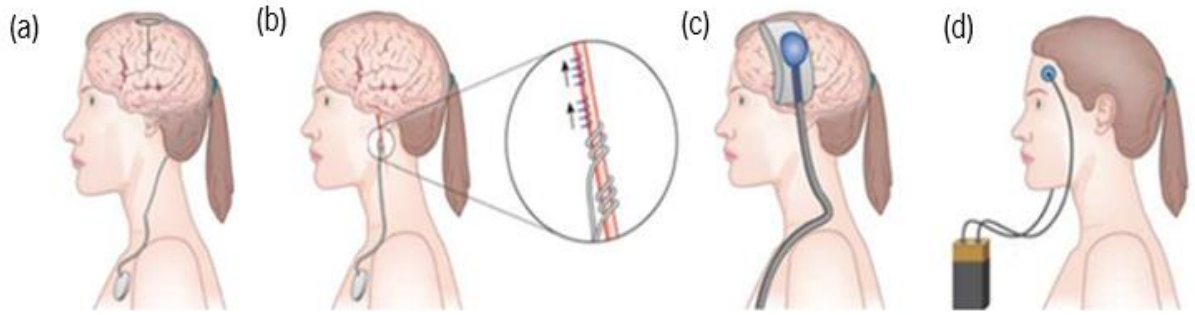


Figure 6 – Current neuromodulation techniques, adapted from [27]. (a) - DBS – surgically implanted electrode connected to a pulse generator. (b) - VNS – surgically implanted electrodes, fixed to the left vagus nerve and connected to a pulse generator. (c) - TMS – electromagnetic coil placed in the patient's scalp. (d) - tDCS – anodal and cathodal stimulation with surface electrodes connected to a DC source (battery).

### 1.1.1. Optogenetics

In a novel and complex approach, which at the time of writing is only available in animal models in experimental contexts, optogenetic techniques combine light emission (with specific wavelengths) and the genetic targeting of neuronal cells with opsins - transmembrane light-activated proteins inserted into specific cells using transgenic technology, that control ion-conductance and the firing of APs by eliciting cell depolarization or hyperpolarization. Optogenetics has demonstrated outstanding temporal and spatial resolutions in animal protocols (Figure 7 a), for activating or suppressing neuronal activity with specific cell-targeting [29, 30]. Connectivity studies can be accomplished through the integration of a mapping technique such as fMRI – optogenetic functional magnetic resonance imaging (ofMRI) - allowing the monitorization of precise, specific and optical targeting of neuronal circuits along with the global brain function. Nonetheless, the need for genetic manipulation and minimally invasive interventions still pose ethic and safety obstacles for human optogenetic neuromodulation [29].

The light-sensitive proteins (opsins) are membrane channels that modify the neuron's activity (in which they are expressed) when exposed to light at specific wavelengths. The opsin genes are separated in two distinct superfamilies - microbial opsins (type I) and animal opsins (type II), where both types contain retinal (a vitamin A-related organic cofactor) as to convert light into energy, that undergoes a conformational change by which these opsin proteins are later designated as rhodopsins [31]. Examples of the most widely used optogenetic actuators are the microbial opsins *Chlamydomonas reinhardtii Channelrhodopsin-2* (ChR2) and *Natronomonas pharaonis halorhodopsin* (NpHR), which function as ion flow modulators and, by manipulating the cell's membrane potential can control its excitability (Figure 7 b). The most commonly used opsin is ChR2 which is a blue light-activated (approximately 470 nm) nonspecific cation channel. This opsin has been successfully used to induce spiking activity in ChR2-expressing neurons, with high temporal precision (on the scale of milliseconds) and cell specificity [32]; whereas NpHR is a yellow light-activated (approximately 580 nm) chloride pump, and has been used to inhibit neuronal activity [33]. ChR2 and NpHR can be simultaneously expressed in the same neuronal cell in view of enabling the bidirectional modulation of neuronal activity, since they present separation of the activation light wavelength. In turn, animal opsins are used for biochemical control, namely through the conversion of G protein-coupled receptors (GPCRs) into optoXRs - light-activated (approximately 500 nm) regulators that modify the activity of intracellular signaling pathways when illuminated. There are several strategies for opsin expression, such as the use of viral vector targeting systems or of transgenic animals [34, 31].

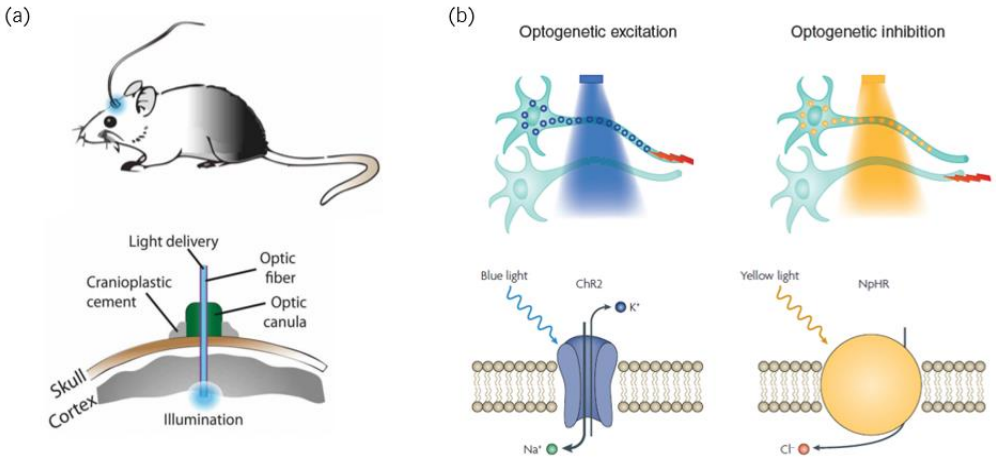


Figure 7 - Optogenetic neuromodulation. (a) - Light delivery in a mice model through a surgically implanted optic cannula attached to the animal's skull, adapted from [35]. (b) - Optogenetic excitation (left) with blue light, that results in the activation and opening of ChR2, leading to $Na^+$ influx and subsequent cell's depolarization; optogenetic inhibition (right) with yellow light of microbial opsins-expressing neurons, which results in the activation and opening of NpHR, leading to the $Cl^-$ influx and subsequent cell's hyperpolarization, adapted from [34, 36].

### 1.1.2. Ultrasound Neuromodulation

Comparatively to the described techniques, ultrasound neuromodulation (UNMOD) is a non-invasive method with a high spatial resolution (in the order of millimeters in diameter), capable of reversibly modulating, i.e., excite or suppress both superficial and deep brain regions with the delivery of acoustic waves through the skull and tissue.

Advances in the US transducer technology enabled the ability of delivering focused ultrasound (FUS), i.e., focal delivery of acoustic waves in a precise location and depth of the target tissue without the modulation of neighboring brain regions (Figure 8). Moreover, through the integration of a compatible sonication setup with MRI, it is possible to achieve a brain-mapping system, namely an MRI-guided focused ultrasound (MRgFUS) [37]. This system enables an enhanced precision, real-time targeting and monitorization of the sonicated structures; however in order to obtain both anatomical and functional information, a functional magnetic resonance imaging (fMRI) acquisition should be coupled with the experimental setup. Thus, clinical results of sonication can be characterized by venous blood oxygenation level-dependent (BOLD) signals, which are connected to the activation or suppression of neuronal activity [38].

High intensity FUS (HIFUS) has been employed in human trials and later, in 2016 and 2018 FDA approved as a treatment route for movement disorders such as essential tremor (ET) [39] and tremor-dominant Parkinson's disease (PD) [40], respectively; namely through thermal ablation of the tremor-mediating brain areas with MRgFUS thalamotomy. HIFU has also been used in the treatment of CNS diseases such as epilepsy [41] and OCD [42], yet it has not been FDA approved. In turn, low intensity FUS (LIFUS) has demonstrated the ability to reversibly modulate neuronal activity in both *in vitro* and *in vivo* models, in the absence of tissue ablation [43, 38]. Moreover, FUS has also been employed for target drug delivery through the disruption of the the protective blood-brain barrier (BBB), which represents a major obstacle for conventional methods such as immunotherapeutic drug delivery [44].

UNMOD is not without hurdles or engineering challenges. One of the biggest obstacles of *in vivo* experiments for transcranial FUS (tFUS) is the subject's skull, producing phenomena like phase aberration in the focusing and a lower energy transmission efficiency due to factors such as the brain's heterogeneity and acoustic impedance mismatches between the interfaces: skin-skull and skull-brain. Therefore, FUS transmission and its feasibility in modulating specific neural networks are hindered by the modifications and uniformities of the ultrasound beam patterns. To overcome this issue, recent studies have used numerical and experimental compensation techniques such as multi-element transducers, compensation

software (computed tomography (CT) correction algorithms) and simulations [45]. Furthermore, little is known on what are the mechanism through which ultrasound (US) modulates neuronal activity and thus, further basic research at the individual neuronal cell level is needed.

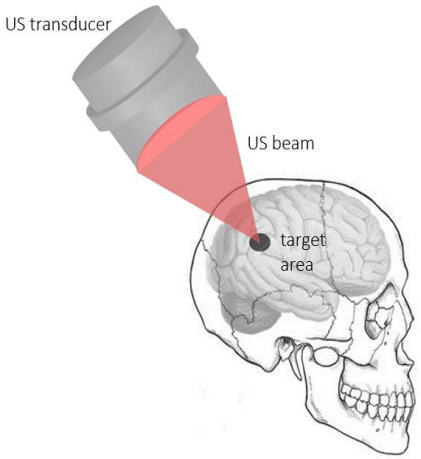


Figure 8 – Illustration of transcranial ultrasound neuromodulation with the use of a focused US transducer.

## 1.3. Motivation and Contextualization

According to a recent Global Burden of Disease (GBD) study [46], millions of people worldwide suffer from a neurological or psychiatric disorder. Furthermore, as of 2017, approximately 4.4% of the world's population was estimated to be affected by depression, which is one of the most widespread neuropsychiatric diseases and a major source of disability and death [47]. The global burden of mental health diseases increased over the last years due to factors such as population growth and aging, leading to higher morbidity and mortality rates [48]. Hence, for the past few decades there has been a growing interest and need for the development of novel neuromodulation techniques as a route of treatment for such illnesses of the central nervous system (CNS).

Focused ultrasound stimulation has emerged as a potential substitute for the aforementioned neuromodulation techniques (subchapter 1.2), namely by providing a transcranial modulation of specific cortical functions without the need for surgical intervention (craniometry and electrode implantation), ionizing radiation or genetic manipulation, along with a high spatial accuracy [49]. In light of the numerous advantages of FUS comparatively to conventional methods, the current work was directed towards the investigation of the modulatory effects of low intensity FUS in individual neuronal cells, in particular in *ex vivo* brain tissue since it represents a simple model for the study of the possible mechanisms underlaying US neuromodulation at both the neuronal population and individual cell levels. For this purpose, a review

of the pioneering literature as well as the selection of the ultrasound system for modulating neural circuits were first performed. Moreover, an *ex vivo* stimulation protocol was developed to study the neuromodulatory effects of ultrasound, coupled with electrophysiological recordings to measure the targeted tissue's electric activity before and after US stimulation. This protocol describes the implementation of ultrasound neuromodulation by defining the stimulus waveform parameters as well as the characterization of the delivered acoustic intensity.

Considering that the modulatory effects of ultrasound stimulation and subsequent induced alterations in the rate of spontaneous spiking activity can be measured through electrophysiology recordings; as a first step to record extracellular neuronal activity in brain slices at a low-cost but in an accurate and reproducible way, a new recording prototype based on tetrodes was developed in this dissertation. Additionally, to ascertain the recording prototype's ability to record not only spontaneous activity but also detect small changes in evoked activity by external stimuli, optogenetic stimulation – a technique that allows the modulation of the activity of genetically modified neurons via light delivery – was used as validation. Furthermore, in order to study the response of individual neurons a new semi-supervised spike sorting algorithm was developed and tested to separate spiking activity from background activity and noise as well as to isolate and classify single neurons. The recording and analysis framework developed in this dissertation will be tested with FUS in a system that was also assembled during this dissertation work.

## 1.4. Objectives and Contributions

The present master's dissertation primary objectives were the selection and assembly of an ultrasound system along with the development of a recording and analysis framework that allows the study of the effects of FUS in individual neuronal cells in *ex vivo* brain tissue. For that purpose, the following contributions were made:

- Specification and assembly of an ultrasound system based upon literature review;
- Development of an experimental protocol for ultrasound neuromodulation of *ex vivo* brain slices;
- Development and implementation of a new low-cost and re-usable prototype to record extracellular activity in *ex-vivo* slices;
- Validation of the developed recording method to successfully measure the modulatory effects on neuronal activity upon presentation of an external stimulus, by means of extracellular electrophysiology recordings and optogenetic neural manipulation;

- Development of a new spike sorting algorithm that allows the analysis of single-unit activity (SUA) of neuronal ensembles recorded in brain slices.;

## 1.5. Structure

This dissertation begins in Chapter 1 by introducing a theoretical background used as a framework during the current study, namely an overview of the neuroscience field by characterizing the nervous cell and synaptic transmissions, along with a brief portrayal of electrophysiological recording techniques. Moreover, this chapter presents a description of the neuromodulation field and its applications, summarizing the strength and weaknesses of current techniques.

Following, Chapter 2 is dedicated to ultrasound neuromodulation, first providing a description of basic ultrasonic principles and next a literature review of UNMOD, exploring in detail *ex vivo* and *in vivo* stimulation protocols used in pioneering literature. Additionally, possible mechanisms underlaying US neuromodulation are discussed in this chapter.

Chapter 3 describes the implemented ultrasound setup and experimental protocol for modulating *ex vivo* brain slices, based on the reviewed UNMOD literature, in which processes such as the selection of acoustic parameters, calibration and positioning of the US transducer are exploited. The protocols for preparing the studied *ex vivo* brain slices as well as the electrophysiology recordings setup, for future validation of the neuromodulation effects of ultrasound, are also presented in this chapter. Furthermore, this chapter describes the design and conception of a novel brain slice extracellular recording prototype along with a detailed description of the newly implemented semi-supervised spike sorting algorithm. The setups and protocols implemented during extracellular recordings of evoked activity (while using opto stimulation) are included in this chapter.

Chapter 4 details the results of the experiments carried out for the preparation of this dissertation. The results include the development and testing of the new extracellular recording prototype. Likewise, the MUA and SUA analysis of the recorded data with tetrodes are also presented for evoked activity.

Chapter 5 presents a discussion of the reviewed UNMOD literature, constrains in selecting the stimulation acoustic parameters and the anticipated results of ultrasound neuromodulation of *ex vivo* brain slices, along with the discussion of the results obtained in Chapter 5; while Chapter 6 summarizes the main findings of this work and possible future directions for this project.

# Chapter 2

# Ultrasound Neuromodulation

## 2.1. Overview of Ultrasound Physics

Ultrasound (US) is a mechanical wave that propagates through medium such as air, water and tissue, with a frequency higher than the human auditory threshold (above 20 kHz). Moreover, US waves propagate through the compression and rarefaction of the medium's constituent particles, i.e., by the formation of high pressure (compression) and low-pressure (rarefaction) areas as the particles oscillate with regard to their resting position. US can be categorized as longitudinal or transverse waves, in which the direction of the particles' oscillation is characterized as parallel or perpendicular to that of wave propagation, respectively [50, 51].

The wavelength ($\lambda$) corresponds to the distance between two oscillating particles, with identical positions and movement phase in the pressure wave (Figure 9 a). According to Equation 4 [50], the wavelength is determined by the speed of sound ($c$) in the propagation medium and by the waveform frequency ($f$). The speed of sound is influenced by characteristics of the medium as well as the nature of the propagation wave.

$$\lambda = \frac{c}{f} \qquad (4)$$

The waveform frequency is characterized as the number of cycles per unit of time. As shown in Equation 5, the period ($T$) corresponds to the time needed to complete a single cycle, i.e. the required time for one particle of the medium in which the US is propagated to complete a single oscillation (Figure 9 b). Hence, the waveform period is mathematically described as the inverse of the frequency [50].

$$T = \frac{1}{f} \qquad (5)$$

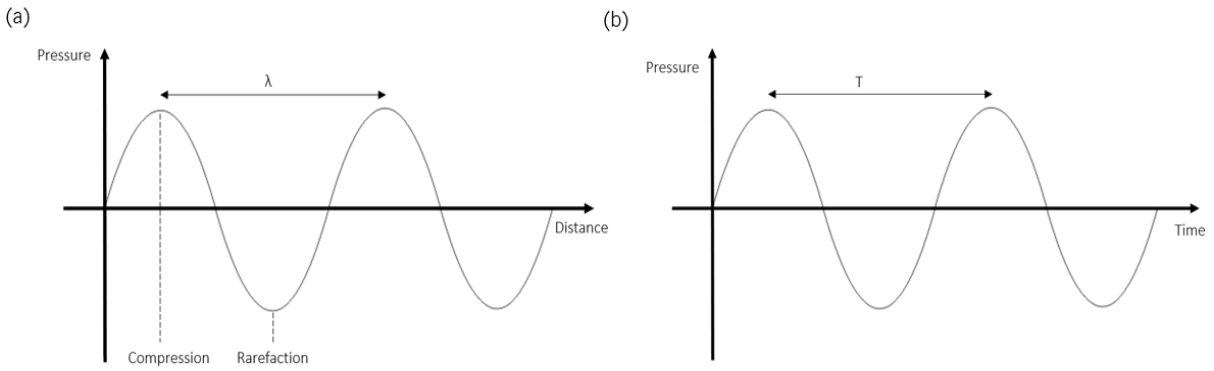


Figure 9 – Spatial (a) and temporal (b) periodicity of a longitudinal US pressure wave, where λ and T correspond to the wavelength and period of the waveform, respectively.

When propagating between two medium with acoustic impedance ($Z_0$) mismatch US is reflected (a portion of the acoustic wave propagates back towards the first medium - echoes) and refracted (a portion of the acoustic wave is transmitted towards the second medium) at the interface. Therefore, the higher the impedance mismatch, the larger the amount of reflected acoustic energy. The acoustic impedance is a function of the propagation medium density ($\rho$) and speed of sound ($c$), as illustrated in Equation 6 [52].

$$Z_0 = \rho c \quad (6)$$

Absorption and scattering of acoustic waves are the two primary mechanisms responsible for US attenuation, i.e., energy loss during the interaction between the acoustic waves and the propagation medium. The absorption of US energy results in heat deposition in biological tissue and potential irreversible tissue damage; whereas the scattering of acoustic waves occurs due to the propagation in inhomogeneous mediums, namely by the interaction between the US and the propagation medium's objects with smaller dimensions than the wavelength of the transmitted acoustic wave. The US attenuation coefficient ($\alpha$) exhibits a power law frequency dependence, represented in Equation 7 as a function of the acoustic frequency ($f$), considering that $\alpha_0$ and $m$ (typically within the range of 1 -2 (tissue-water)) are influenced by the propagation medium. According to this equation, the US energy attenuation is minimized by reducing the acoustic frequency [53].

$$\alpha(f) = \alpha_0 \cdot |f|^m \quad (7)$$

An ultrasound transducer is capable of transmitting and receiving US waves, i.e., generate acoustic waves through the conversion of electrical energy into mechanical energy (air pressure) by means of a piezoelectric effect, and the opposite process. As illustrated in Figure 10, the ultrasound field of a planar transducer is distinguished in two zones: (1) – Near field (NF) or Fresnel Zone, that corresponds to the acoustic field right in front of the transducer face, characterized by oscillations in the acoustic intensity (multiple local maxima and minima) as a result of wave interference, limiting the accurate analysis of US transmission; (2) – Far field (FF) or Fraunhofer Zone, represented as the acoustic field beyond the Fresnel Zone and characterized by a divergent US beam with more uniform acoustic intensities and a smooth decaying. The transition between these two fields is termed as the "natural" focus of the transducer, in which the last signal maxima occurs at a distance approximately equal to the Near field distance ($N$) [53]. According to Equation 8 [54], $N$ is proportional to the square of the transducer's diameter ($D$) and inversely proportional to the transmitted US wavelength ($\lambda$). Therefore, transducers with higher frequencies have a longer Near field distance and consequently, a longer focal length – distance from the surface of the transducer in which the signal reaches its maximum amplitude.

$$N = D^2 \cdot \frac{f}{4c} = \frac{D^2}{4\lambda} \quad (8)$$

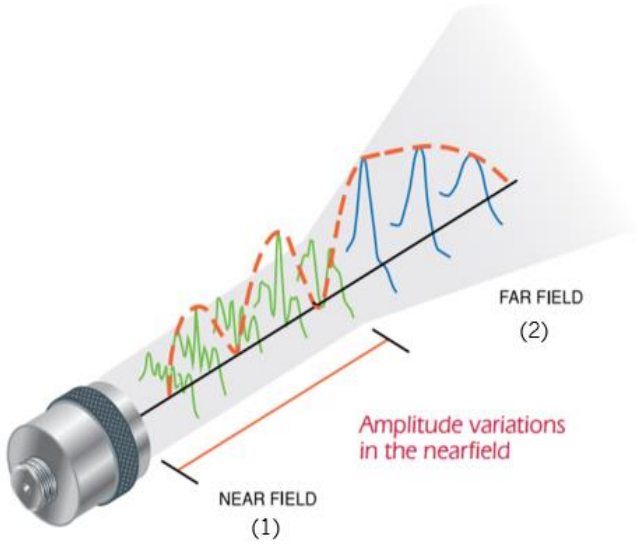


Figure 10 – Schematic representation of the ultrasonic field of a planar transducer, adapted from [54]. (1) – Near field, with multiple local maxima and minima and a highly irregular intensity (orange line). (2) – Far field, characterized by a smooth intensity decay (orange line). Green and blue lines correspond to US waveforms.

In focused transducers, the acoustic energy converges to a single focal spot within an area detonated as focal zone ($F_Z$), and then the propagation beam diverges, as depicted in Figure 11 [54]. The focus of the transducer can be displaced and distorted due to acoustic mismatches between the transducer and the targeted tissue that lead to phase aberration, i.e., phase errors in beamforming due to tissue inhomogeneities which defocus the US beam.

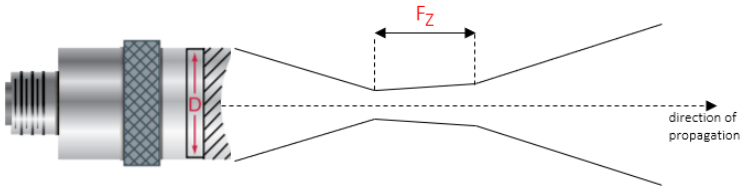


Figure 11 – Schematic representation of the ultrasonic field of a focused transducer, adapted from [54].

A matching layer with a similar acoustic impedance to the piezoelectric crystal can be used to improve the transducer's performance, with a layer thickness equal to a quarter of the wavelength ($\lambda/4$) at the transducer's fundamental frequency. Therefore, by inserting an intermediate material between the ultrasonic probe and the targeted medium, an impedance matching is obtained and consequently, the signal reflection at the source is minimized, which in turn results in the transmission of a higher amount of acoustic energy to the tissue of interest [55]. Furthermore, a coupling ultrasound gel can be place between the transducer face and tissue for a better acoustic contact, namely by diminishing the impedance mismatch from existing air gaps [56].

### 2.1.1. Ultrasound-induced Bioeffects

Therapeutic ultrasound is capable of producing different interactions with the sonicated tissue, namely thermal and non-thermal effects. Thermal-induced US bioeffects result from the absorption and subsequent attenuation of acoustic energy; later converted to heat and temperature rise at the beam focus, which is influenced by parameters such as the acoustic properties of the target tissue and the duration of the US exposure. This rise in temperature is denoted as thermal dose and assesses the thermal-induced cell damage or death. Equation 9 depicts the empiric relationship for calculating thermal dose, in which the time ($t$) correspondent to the threshold for a specific temperature ($T$) to produce a bioeffect is related to the time ($t_{43}$) required for obtaining the same result at 43 °C, considering that $R$ = 4 when $T \leq 43$ °C and $R$ = 2 when $T \geq 43$ °C [57, 58].

$$t = t_{43} \cdot R^{(T-43)} \quad (9)$$

The interaction between US and tissue can generate multiple mechanical-induced bioeffects, namely cavitation, radiation forces and acoustic streaming. Cavitation corresponds to the formation and oscillation of gas cavities (microbubbles) in response to the delivery of acoustic waves with compression and rarefaction periods, being categorized as inertial cavitation and stable cavitation. Stable cavitation corresponds to the linear oscillation of the microbubbles over their equilibrium radius; whilst inertial cavitation occurs when the acoustic pressure surpasses a specific threshold and the gas microbubbles grow and collapse violently, incurring in cell damage [57, 58].

Radiation force is characterized as an US-induced steady and time-averaged force, constituting one of the underlaying mechanism behind acoustic streaming. As specified by Equation 10, the radiation force ($F_{rad}$) is proportional to the intensity of the delivered US, while $\alpha$ and $c$ are the attenuation of the acoustic wave and sound speed, respectively [59]. Lastly, acoustic streaming can occur when US is transmitted in a fluid and the radiation force generates a fluidic flow, which may modulate the cell's membrane permeability.

$$F_{rad} = \frac{2\alpha I}{c} \quad (10)$$

### 2.1.2. Stimulation Parameters and Safety Regulatory Standards

The transmission of US can be optimized by adjusting the ultrasonic wave parameters to the target tissue. Examples of such parameters are the fundamental frequency ($f_0$), pulse duration ($PD$), pulse repetition frequency ($PRF$), duty cycle ($DC$), sonication duration ($SD$) and intensity, as illustrated in Figure 12. Not only do these factors affect the sonication itself but also the resulting outcome, namely the biological effects on the targeted brain areas. The fundamental frequency, as previously mentioned, corresponds to the number of cycles per unit of time and according to Equation 4, it is inversely proportional to the wavelength. Therefore, this parameter influences the width of the focal point (focus of stimulation), considering that lower frequencies have wider focal points .

The transmission of US can be conducted through the use of continuous (CW) or pulsed (PW) waves. In continuous transmission, US is constantly delivered, as opposed to pulsed transmission in which a finite number of cycles ($N$) of a specific frequency are delivered, with pauses between sonications denominated as inter stimulation intervals ($ISIs$). This type of transmission mode diminishes energy

deposition and consequentially, the probability of incurring in tissue overheating and damage (phenomenon associated with US thermal effects).

The pulse duration ($PD$) corresponds to the period between the beginning and end of oscillation and according to Equation 11, $PD$ is equal to the number of cycles multiplied by the period of one cycle. In turn, the period between the start of one pulse and the start of the following pulse is denominated as pulse repetition period; whereas the inverse of this parameter corresponds to the pulse repetition frequency ($PRF$) (Equation 12), which defines the delivery rate of US pulses. Furthermore, the $DC$ equals the percentage of the ultrasound wave pulse duration and consequently, the percentage of time that the sonication is activated during the total length of the neuromodulation procedure. According to Equation 13 the duty cycle (presented in percentage) is a function of the pulse duration and pulse repetition period [60, 61].

$$PD = N \cdot T = N \cdot \frac{1}{f} \tag{11}$$

$$PRF = \frac{1}{PRP} \tag{12}$$

$$DC = \frac{PD}{PRP} \cdot 100\% = PD \cdot PRF \cdot 100\% \tag{13}$$

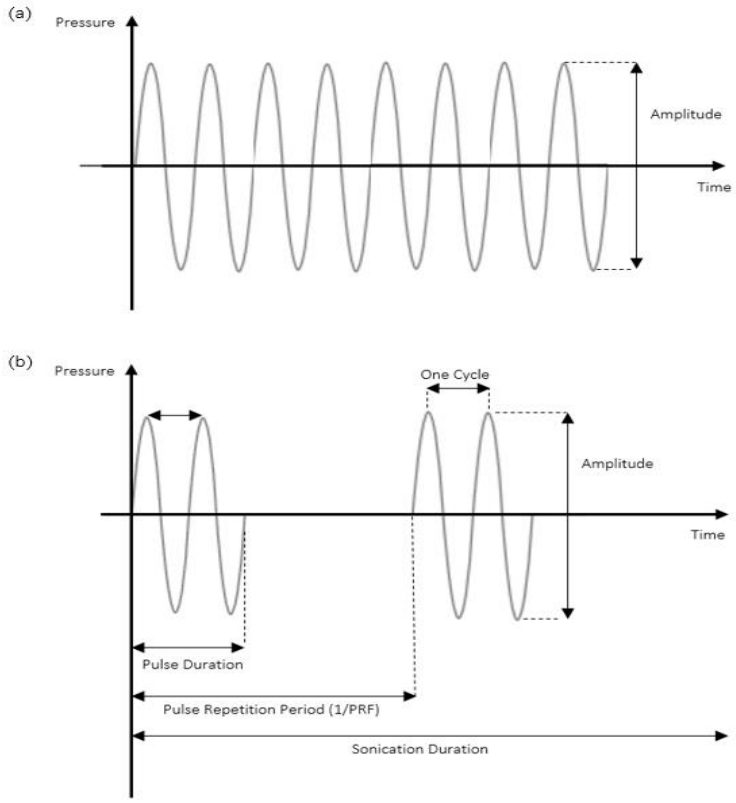


Figure 12 – Pulsed Ultrasound and correspondent acoustic parameters.

Another important parameter is the US intensity (expressed in $W/m^2$), which corresponds to the rate of energy flow per unit area normal to the direction of the acoustic propagation. In pulsed transmission, the US intensity can be characterized through the measurement of the instantaneous acoustic pressure ($p_i$) (in MPa), namely with the use of a hydrophone, which is a transducer designed to operate in liquid media (protocol later explored in subchapter 3.1.1). As depicted in Equation 14, the instantaneous intensity is proportional to the square of the acoustic pressure and inversely proportional to the acoustic impedance ($Z_0$) [18].

$$I_i = \frac{{p_i}^2}{Z_0} = \frac{{p_i}^2}{\rho c} \qquad (14)$$

The pulse intensity integral ($PII$) is calculated by integrating the instantaneous intensity (Equation 15 [18]). Through this parameter, it is possible to estimate two important acoustic exposure measures, namely the spatial-peak, temporal average intensity ($I_{SPTA}$) and the spatial-peak, pulse average intensity ($I_{SPPA}$). The $I_{SPTA}$ characterizes the temporal-average intensity of the transmitted pulses, i.e., the maximum intensity over the pulse repetition period; constituting a good measure of US-induced thermal bioeffects, such as tissue heating. This parameter is described in Equation 16 [18] as the product of the pulse intensity integral and the pulse repetition frequency. In contrast, the $I_{SPPA}$ measures the pulse-average intensity and enables the assessment of brief US-induced mechanical bioeffects. According to Equation 17 [18], this measure is proportional to the pulse intensity integral and presents an inverse relation with the pulse duration.

$$PII = \int I_i dt \qquad (15)$$

$$I_{SPTA} = PII \cdot PRF \qquad (16)$$

$$I_{SPPA} = \frac{PII}{PD} \qquad (17)$$

Figure 13 presents a schematic illustration of the spatial and temporal variation of pulsed US intensity. The top panel depicts two US pulses, in which the highest peak, the average intensity of single pulse and the average over one PRP are represented as temporal peak (TP), pulse average (PA) and temporal average (TA), respectively. The bottom panel characterizes the spatial profile of the US beam intensity, where the intensity peak and the average over the spatial profile are denoted as spatial peak (SP) and spatial average (SA), respectively [62].

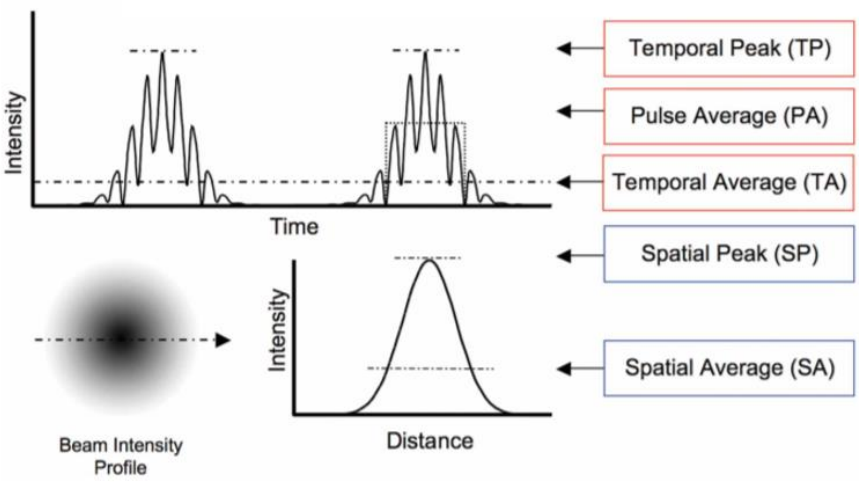


Figure 13 – Representation of the spatial and temporal variation of pulsed US intensity, adapted from [62].

Moreover, another important parameter for the assessment of acoustic exposure is the mechanical index ($MI$), which measures the US-induced mechanical bioeffects such as inertial cavitation that can induce cell or tissue destruction. The $MI$ is defined in Equation 18 as the quotient of the peak rarefactional (peak negative) pressure ($p_r$) and the square root of the transmitted acoustic frequency ($f$), considering that lower frequencies result in lower $MI$ [18].

$$MI = \frac{p_r}{\sqrt{f}} \qquad (18)$$

On the aspect of biosafety, the acoustic output levels must be in agreement with the safety threshold guidelines specified by the FDA for diagnostic imaging purposes (for adult cephalic ultrasound). The parameters stipulated by this entity were an $I_{SPTA} \leq 720$ W/cm$^2$, $I_{SPPA} \leq 190$ mW/cm$^2$ and a $MI \leq 1.9$ [63].

## 2.2. Ultrasound Neuromodulation

Over the last six decades, systematic research in the neuroscience field has demonstrated US ability to modulate neuronal activity in the central nervous system (CNS) and peripheral nervous system (PNS), either in *ex vivo* and *in vivo* nerves. As early as 1958, by means of electrophysiological recordings, Fry *et al.* [64] demonstrated that high-intensity US can reversibly suppress the visual cortex activity of cat's intact brain (lateral geniculate nucleus), without visible histological lesions. Additionally, research performed *in vitro* hippocampal preparations, namely in the CA1 and dentate gyrus pyramidal neurons,

reported that evoked field potentials can be elicited or depressed by FUS pulses [65, 66]. Later on, through the neuromodulation of frog peripheral nerves in a continuous mode, Tsui and colleagues [67] concluded that US waves (3.5 MHz) with higher temporal average intensities ($I_{TA}$ = 1-3 W/cm$^2$) seem to decrease compound action potential (CAP) amplitude and conduction velocity (CV) in the sonicated areas.

In an important study, Tyler *et al.* [43] showed that low frequency, low-intensity US (LILFU) pulsations (0.0227-0.18 ms of 0.44–0.67 MHz US, $I_{SPPA}$ = 2.9 W/cm$^2$) were capable of evoking electrical neural activity in the CNS , such as action potentials (APs) and synaptic transmission. By way of confocal imaging and electrophysiological recordings *in vitro* hippocampal slice cultures, this group concluded that the mechanosensitive voltage-gated ion ($Na^+$ and $Ca^{2+}$) channels' activity was triggered as a response to LIFU stimulation, inducing synaptic transmissions and SNARE-mediated synaptic vesicle exocytosis (release of neurotransmitters). These results triggered a series of experimental trials targeting the CNS of anesthetized rodents [49, 25, 68, 69, 56], rabbits [38], non-human primates [70], sheep [71] and pigs [72]. To discover the optimal acoustic stimulation parameters and pulsing protocols that enable an efficient *in vivo* neuromodulation, these UNMOD studies resorted, predominately, to sonication frequencies lower than 1 MHz, in particular with transcranial stimulation of neuronal activity which is characterized by several barriers in the transmission and focusing of acoustic energy through the skull bone to the target brain regions. Outcomes such as motor responses (limb movement) and elicitation of somatosensory excitability were verified in these reports, in some cases through electrophysiology techniques such as electroencephalography (EEG) and electromyography (EMG), which involve the recording of surface electrical activity in the brain and muscle, respectively.

Table 1, 2 and 3 present a summary of the acoustic parameters in pioneering experimental literature of *in vitro* as well as *in vivo* animal and human models, employed as a framework in the current assay. UNMOD-induced effects in multiple experimental studies (targeting either the CNS or peripheral nerves) are also exploited. Moreover, Appendix I presents a published review article "Low Intensity Focused Ultrasound Modulation of Neural Circuits Activity", developed in the current dissertation.

### 2.2.1. In Vivo Small Animal Neuromodulation

The same research group of Tyler *et al.* also documented motor responses as a product of modulating intact mice brains (motor cortex and hippocampus brain regions) with transcranial low-intensity US pulsations (26-333 ms of 0.25-0.5 MHz US, $I_{SPPA}$ = 0.075–0.229 W/cm$^2$) [25]. They concluded that distinct neuronal structures can be modulated through US with a lateral spatial resolution

of about 2 mm and with insignificant temperature growth. A general protocol for *in vivo* transcranial UNMOD, including both continuous and pulsed stimulus, was also presented by Tufail and colleagues. This protocol enables the study of the US bioeffects on the sonicated areas of intact epileptic mouse brains, specifically via motor responses and electromyography recordings (EMG) [18].

With a compatible fMRI monitorization and EMG recordings, Yoo *et al.* [38] verified via BOLD fMRI signals that pulsed FUS (0.5-50 ms of 0.69 MHz US, $I_{SPPA}$ = 12.6 W/cm$^2$ and 13.5 ± 3.8 mW/cm$^2$) can evoke or suppress neural tissue excitability (bimodal modulation) in the visual and somatomotor cortex of rabbits subjected to craniotomies, without provoking histological tissue or blood-brain barrier (BBB) damage. Moreover, by applying FUS to the thalamus of ketamine/xylazine anesthetized rats with similar acoustic parameters (0.5 ms of 0.65 MHz US, $I_{SSPA}$ = 6 W/cm2) and set up, Yoo *et al.* [68] also verified that US can decrease the emergence time of voluntary limb movement from general anesthesia.

A significant study conducted by Younan *et al.* [69] examined transient motor responses induced by the delivery of transcranial FUS (250-500 ms of 0.32 MHz US, $I_{SPPA}$ =17.5±7.5 W/cm$^2$) pulses in the motor cortex of anesthetized rats. In order to predict the acoustic field, acoustic pressure amplitude and intensity inside the rat's head cavity, this study resorted to a numerical simulation based upon a computerized tomography (CT) scan of the rat's head. By comparing these estimations with the hydrophone-measured intensities in free water (free-field), it was inferred that US waves at low intensities were reverberated (reflected) within the rat's cranium, inducing the formation of standing waves These standing waves correspond to constructive and/or destructive interference patterns in the acoustic field, which may increase the pressure amplitude outside the focus *in situ*, originating cavitation effects as well as heat deposition and brain damage (cerebral hemorrhages), especially at high intensities. One explanation could be that the rodent's small-size skull, smaller than the transducer, results in the propagation of US with wavelengths of the same dimension as the rodent's cranium. Thus, the occurrence of aberrations, distortions and other wave interactions inside the rat cranium are very likely to occur. These phenomena could result in the modulation of surrounding tissues in the acoustic path, diminishing FUS's spatial accuracy. Furthermore, as to assess the presence of a pressure threshold, only one stimulation parameter was altered, namely the acoustic pressure amplitude, by which it was verified that tFUS is conditioned by pressure as well as anesthesia.

Likewise, King and colleagues [56] explored the influence of anesthesia and several acoustic parameters (acoustic intensity, sonication duration, stimulation mode, US frequency, pulse repetition frequency) on the stimulation success rate by applying continuous tFUS (20-480 ms of 0.25-0.6 MHz

US, $I$ = 0.01- 79.02 W/cm$^2$) to the motor cortex of rats. Along with the confirmation of previous findings in which the efficacy of UNMOD diminishes with a higher anesthesia level and higher US carrier frequencies, the elicited motor responses proved to be an all-or-none response, being that higher acoustic intensities required higher stimulation frequencies to obtain the same outcomes. Furthermore, though both Continuous-wave (CW) and Pulsed-wave (PW) transmission modes were capable of eliciting brain activity (provided that the $I_{SPTA}$ are equated), short-duration CW was found to be the most effective in stimulating neuronal activity and consequential motor responses, contesting the prominent use of PW mode in prior studies.

Since the optimal stimulation frequency as not yet found consensus among the various UNMOD studies, Ye *et al.* [73] conducted a study on the sonication frequency influence upon US neuromodulation success. To achieve such a purpose, the mouse motor cortex was first targeted with low frequency continuous FUS (80 ms of 0.3 - 1MHz US, $I_{SPPA}$ = 0.02 – 9.4 W/cm$^2$) and, unlike King *et al.* previous findings, the success rate was found to be independent of the utilized US carrier frequencies together with whether the sonication duration was kept constant or shifted. Next, frequencies above 1 MHz (80 ms of 1.4 - 2.9 MHz US, $I_{SPPA}$ = 0.02-127 W/cm$^2$) were also capable of inducing EMG activity and motor responses; nevertheless, as the carrier frequency was augmented, the stimulation efficacy decreased, and higher US spatial peak intensities were needed in order to obtain the same success. Additionally, by maintaining a constant transducer's frequency and varying focal spot size, the group found that a smaller stimulation area does not increase its spatial specificity.

More recently, Baek *et al.* [74] targeted the lateral cerebellar nucleus (LCN) of stroke mice with pulsed LIFUS (300 ms of 0.35 MHz US, $I_{SPPA}$ = 2.54 W/cm$^2$), eliciting motor-evoked potentials (MEPs) plus muscle movement in both forelimbs. After 4 weeks of rehabilitative training, the group verified that the mice subjected to LIFUS neuromodulation exhibited an ameliorated sensorimotor behavior when compared to the stroke group without stimulation. This data could support the hypothesis that LIFUS can enhance cerebellar cortical plasticity and the activation of perilesional cortical areas, therefore able to sustain the recovery of sensorimotor function from an ischemic injury.

### 2.2.2. In Vivo Large Animal Neuromodulation

Concerning large animal models, Deffieux *et al.* [70] conducted short-pulsed LIFUS (100 ms of 0.32 MHz US, $I_{SPPA}$ = 13.5 ± 3.8 mW/cm$^2$) sonications in the prefrontal (frontal eye field (FEF)) and premotor cortex (PMC) of awake nonhuman primates. The subjects were simultaneously submitted to an

anti-saccade (AS) task - a visual task in which the cognitive control of eye movement (regulated by the prefrontal cortex) is tested. This group demonstrated that LIFUS can modulate AS latencies and, consequently decrease cortical excitability. Following, Lee *et al.* [75] targeted the primary sensorimotor (S1) and visual (V1) cortices of anesthetized sheep with transcranial MRgFUS (300 ms of 0.25 MHz US, $I_{SPPA}$ = 3.4-14.3 W/cm2), eliciting EMG and EEG potentials (motor evoked potentials (MEPs) and visual evoked potentials (VEPs), respectively). Stimulation of the S1 didn't produce any contralateral motor responses, whilst prolonged repetitive V1 excitation was accompanied by adverse effects (microhemorrhages).

Dallapiazza and colleagues [72] performed a series of neuromodulation experiments by delivering both high and low-intensity FUS to large animals, such as pigs. Firstly, by targeting the pig ventrolateral thalamus (VPL) with pulsed LIFUS (43.7 ms of 0.22-1.14 MHz US, $I_{SA}$ = 25-30 W/cm$^2$) they concluded that deep-brain functions can be reversibly modulated. The monitorization of the somatosensory evoked potentials (SSEPs) (electrophysiologic recordings) showed that neuronal activity was suppressed by longer duration pulses and sonication duration. Moreover, a non-invasive and selective LIFUS mapping in the thalamus was also carried out and, lastly, during LIFUS sonications, tissue heating was monitored by real-time MR-thermography. Experimental data supported that low-intensity FUS can regulate brain activity without endangering tissue integrity, being that at the acoustic focus the temperature increase did not surpass the sensitivity standards of the MRI thermography. Histologic evaluations revealed that tissue targeted with LIFUS pulses presented no signs of lesions, while thalamus exposed to HIFUS showed signs of tissue damage and necrosis, endorsing once again the safety and possible application of LIFUS in human trials.

### 2.2.3. In Vivo Human Neuromodulation

Following the discoveries of Deffieux *et al.*, Legon and colleagues demonstrated the ability of tFUS (0.5 s of 0.5 MHz US, $I_{SPPA}$ = 23.87 W/cm$^2$) to modulate human cortical functions, namely in the primary somatosensory cortex (S1). As showed by EEG recordings, the SSEPs generated by median nerve (MN) stimulation, were lessened by tFUS delivery. This inhibition was then associated with an augmented sensory discrimination in patients performing behavioural tasks (two-point and frequency discrimination tasks), while being subjected to tFUS delivery. The authors hypothesised that by supressing SSEPs, FUS can narrow spatial cortical excitability and consequently improve the patient's tactile discrimination [37].

Furthermore, in an innovative approach the same group [38] applied low intensity tFUS (0.5 ms of 0.5 MHz US, $I_{SPPA}$ = 6.16 W/cm$^2$) simultaneously with transcranial magnetic stimulation (TMS) to the human primary motor cortex (M1). Whilst the patients executed a stimulus response task, the reaction time was diminished as a response to ultrasound *stimuli* delivery. This outcome corroborated the results in the previous study, since by supressing neuronal activity FUS generated a behaviour and task performance improvement.

Similarly, Lee *et al.* [76] studied the human primary (S1) and secondary (S2) somatosensory cortices, which were targeted with dual tFUS (500 ms of 0.21 MHz US, $I_{SPPA}$ = 35 W/cm$^2$), i.e., both regions in the same hemisphere were simultaneous or separately stimulated through the use of multiple transducers, while being under fMRI guidance. UNMOD elicited tactile sensations (hand and arms, contralateral to the sonication) in the absence of external sensory *stimuli*. The same group reported tFUS (300 ms of 0.27 MHz US, $I_{SPPA}$ = 0.7-6.6 W/cm$^2$) ability to modulate the human primary visual cortex (V1). Moreover, BOLD fMRI signals concurrent to FUS stimulation revealed the activation of not only the sonicated areas, but also of neuronal regions associated with visual and higher-order cognitive processes, being that the activated regions were spatially align with the targeted areas. In addition, this report performed a series of acoustic simulations to predict the US beam propagation patterns and intensity distribution inside the patient's cranium, inferring that US delivery through the skull to the target areas was successful by using a 0.27 MHz single-element focused transducer [42].

In 2016, a case study reported the treatment of a 25-year old patient, suffering from post-traumatic disorder of consciousness (DOC) - coma, vegetative state (VS), minimally conscious state (MCS) - by delivering pulsed LIFUS (30 s of 0.65 MHz US, $I_{SPTA}$= 720 mW/cm$^2$) to the thalamus, under MR guidance (MRgFUS). The patient exhibited a progressive improvement in speech, motor and oromotor functions after sonication (between 13- and 17-days post-stimulation), without suffering from LIFUS-induced adverse effects. Nevertheless, further research is needed to causally correlate the patient's rehabilitation with LIFUS modulation, considering that this recovery could have been a spontaneous event [43].

### 2.2.4. Underlying Mechanism of Action

Regardless of the abundant findings of the aforementioned studies, the precise mechanism behind UNMOD, at a cellular and molecular scale, is still elusive. Ultrasound ability to either stimulate or suppress neuronal activity in a wide selection of sonication parameters, modulation protocols and experimental conditions also contribute to the complexity in grasping the biophysical mechanisms underlying US

neuromodulation. Therefore, additional research and progress are needed in this field to achieve safer and further efficient modulation of neuronal circuits by the use of acoustic waves.

At high intensities, US can induce thermal effects on tissue, namely heating caused by the absorption of acoustic energy. Through the exploration of safety thresholds for FUS inhibition of bullfrog nerve activity, an *in vitro* study [77] showed that the thermal effects of pulsed FUS (1-30 ms of 0.661-1.986 MHz US, $I_{SPTA}$ = 100–875 W/cm$^2$) can temporarily or permanently suppress nerve conduction. At high-frequencies, these effects were correlated with a temperature increase (inferior to the thermal-ablation threshold). However, at low-frequencies FUS thermal effects failed to account for the inhibition of neural signaling, which was then associated to non-thermal effects (cavitation). However, recent experimental protocols using low frequency, low intensity FUS have disregarded thermodynamics as a main contributor to the underpinning stimulation mechanism, reporting that the activation of brain regions was associated with a minor rise of temperature (less than 0.01°C) [25]. Reinforcing this repudiation, Kubanek *et al.* [78] demonstrated that modulatory effects were driven by non-thermal stimulation while targeting the CNS of *C. elegans* nematodes with pulsed LIFUS (200 ms of 10 MHz US). Their data indicated that in nematodes without mechanosensitive ion channels, LIFUS-induced neuronal activity was eliminated (in opposition to the results obtained with the nematodes missing thermosensitive ion channels). Moreover, this study also reported that increased modulatory effects could be achieved by adjusting the sonication parameters to obtain higher acoustic radiation forces (non-thermal mechanism).

US waves can produce numerous effects of a mechanical nature while interacting with tissue, such as cavitation, acoustic streaming and acoustic radiation forces (see subchapter 2.1.1), or a combination of these responses. Several cellular-level models were postulated in order to attain a better understanding of the mechanisms behind UNMOD bioacoustic interactions, namely the flexoelectricity model, the soliton model, the bilayer sonophore (BLS) model and the neuronal intramembrane cavitation excitation (NICE) model.

The flexoelectricity model [79] describes the action potential (AP) as a flexoelectrical wave propagating along the axon membrane, where US induces the modification of the membrane's curvature through mechanical bending. It hypothesizes that US exerts non-thermal actions on cellular targets such as mechanosensitive ion channels, leading to conformational changes that can act on properties like membrane conductance and, in turn to the depolarization and AP generation. Tyler *et al.* [43] verified that voltage-gated ion channels are mechanically sensitive to US, considering that $Na^+$ and $Ca^{2+}$ transients can be evoked when delivering LIFUS to *ex vivo* mice brain tissue, eliciting neuronal electrical activity as

well as the exocytosis of neurotransmitters. Moreover, by adding tetrodotoxin (TTX), a neurotoxin capable of inhibiting voltage-gated $Na^+$ channel currents, the LIFUS-induced neuronal activity was suppressed, indicating that US increases the ion channels conductance and consequently induces its opening. The blocking of voltage-gated $Na^+$ transients by TTX (implanted in the cortex of transgenic mice) and subsequent attenuation of US-induced cortical activity was also demonstrated by Tufail *et al.* [25] through the monitorization of local field potentials (LFPs) and multiunit activity (MUA) in the primary motor cortex (M1) of mice. Once again, they concluded that US elicits cortical excitability mediated by APs.

In the soliton model [80], the AP is considered as a density pulse (soliton) that propagates along the axon membrane (described as a cylindrical lipid membrane) without energy attenuation or change in shape, similarly to a piezo-electric wave. The formation of this electromechanical soliton is temperature-dependent and based upon the thermodynamics and phase behavior of the lipids in the cell membranes, which are not taken into account in the H-H model (presented in subchapter 1.1.1). Therefore, US-induced thermal and mechanical effects can produce thermodynamic variables that affect the cell's membrane and consequently, generate or modify the propagation of AP.

The BLS model was proposed by Krasovitski and colleagues [81] as a unifying mechanism for US-induced bioeffects, where acoustic pressure waves induce intracellular deformations - expansions and contractions – that at elevated levels of stress and strain can induce membrane rupture. Therefore, US energy can be absorbed by the bilayer membrane and transformed into intramembrane cavitation, which can generate modifications in membrane permeability and activate mechanotransduction actions. Likewise, Plaksin *et al.* [82] stipulated that electromechanical effects are behind low-intensity US neuromodulation, namely by means of a neuronal intramembrane cavitation excitation (NICE) model, which couples a modified BLS model with the Hodgkin-Huxley (H&H) model, adapted for a pyramidal neuron. This model assumes that intramembrane cavitation produces hyperpolarizing capacitance displacement currents and subsequent charge accumulation until reaching the AP threshold. Hence, the membrane's permeability can be increased by fast fluctuations in its capacitance, promoting membrane depolarization. Furthermore, the NICE model analyses the influence of acoustic parameters (US frequency and pulse duration) on the intensity thresholds for single AP generation, wherein intensity activation thresholds are slightly enhanced with stimulation frequency and diminished with pulse duration [82, 83]. Such inferences are in accordance with the results of King *et al.* [56] that, as depicted in Figure 14, concluded that the stimulation success is increased with acoustic intensity, seeing that higher frequencies required greater intensities to attain the same success rate.

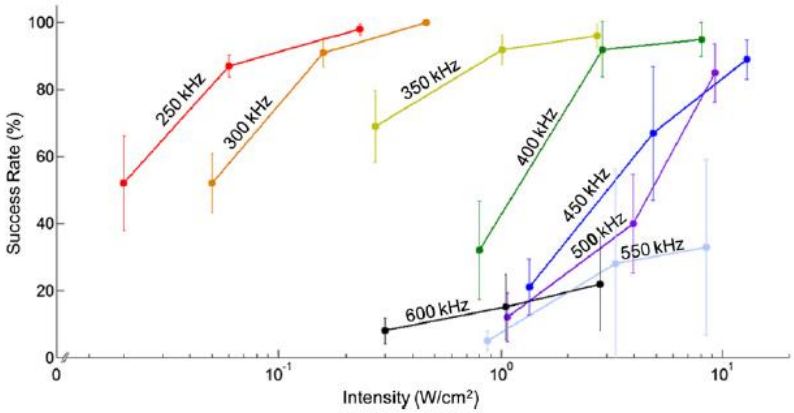


Figure 14 – Influence of the US intensity in the modulation success rate at several fundamental frequencies (ranging from 250 kHz to 600 kHz and 1 MHz US). Each curve depicts the average of all CW stimulations conducted at the respective fundamental frequency [56].

Contrary to previous stated theories, a recent unifying framework [84, 85] , questions US capability of directly modulating brain activity, claiming instead that UNMOD effects result from the indirect activation of the auditory cortex, in particular through the cochlear pathway. By delivering low intensity pulsed ultrasound (500 ms of 0.22 MHz US, $I_{SPPA}$ = 20-330 mW/cm²) to the primary auditory cortex (A1) and primary somatosensory cortex (SC1) of guinea pigs, Guo *et al.* [84] verified that subjects either deprived of bilateral cochlear fluids or submitted to a transection of the auditory nerves were unresponsive to LIFUS stimulation. Along similar lines, through wide-field calcium imaging (fluorescence imaging method), Sato *et al.* [85] demonstrated that motor responses induced by FUS (80 ms of 0.5 MHz US, $I_{SPTA}$ = 0.034 - 4.2 W/cm²) applied to the right visual cortex, diminishes in chemically deafened mice. To support this inference, EMG signals showed that sound was also capable of eliciting cortical activity in resemblance to UNMOD. Alike the previous study, it suggested that US modulates neuronal activity of transgenic mice through an indirect mechanism, in particular through the modulation of auditory regions. Hence, the delivery of FUS could produce mechanical effects despite the fact that ultrasound frequencies are inaudible to the studied mammal.

Nevertheless, this theory has been refuted by another study [86] that applied tFUS (80 ms of 0.5 MHz US, $I_{SPTA}$ = 1-3.78 W/cm²) to both normal hearing mice and genetically deafened mice. This group verified that the tFUS-elicited motor responses were not influenced by the elimination of peripheral auditory pathway, namely through the analysis of electrophysiologic signals and motor responses.

Table 1 - Summary of UNMOD parameters and outcomes from selected *in vitro* studies of both CNS and PNS.

| Author/Year | Target Region | Frequency (MHz) | PRF (kHz) | Other acoustic parameters | Energy | Outcomes |
|---|---|---|---|---|---|---|
| Rinaldi *et al.*, 1991 [65] | Rat hippocampal slice culture (CA1) | 0.75 | 150 | Transmission mode: PW<br>Pulse duration: 0.006 ms | $I_{SPTA}$ = 80 W/cm² | FUS supressed neural activity with a temperature rise lower than 1 °C. |
| Bachtold *et al.*, 1998 [66] | Rat hippocampal slice culture (CA1 and dendrite gyrus) | 0.5 | 200 | Transmission mode: PW | $I_{SPTA}$ = 40-110 W/cm² | FUS supressed fiber volley and cell population potentials. Elicited dendrite potentials. |
| Tsui *et al.*, 2005 [67] | Frogs sciatic nerve | 3.5 | – | Transmission mode: CW<br>Sonication duration: 5 min | $I_{TA}$ = 1-3 W/cm² | US increased and decreased CAPs amplitude, increasing nerve conduction with a temperature rise between 3-10 °C. |
| Tyler *et al.*, 2008 [43] | Mice hippocampal slice culture (CA1) | 0.44–0.66 | 0-0.1 | Transmission mode: PW<br>Pulse duration: 0.0227–0.18 ms<br>Cycles per pulse: 10<br>Number of pulses: 3-250 | $I_{SPTA}$ = 0.023 W/cm²<br>$I_{SPPA}$ = 2.9 W/cm² | LILFU activated voltage-gated $Na^+$ and $Ca^{2+}$ channels, synaptic transmissions and SNARE-mediated synaptic vesicle exocytosis. |
| Colucci *et al.*, 2009 [77] | Frogs sciatic nerve | 0.661–1.986 | 0.01-0.02 | Transmission mode: CW(1) and PW(2)<br>Sonication duration: 30 s(1) and 1–10 ms(2) | $I_{SPTA}$ = 100 – 875 W/cm² | FUS blocked nerve conduction in a reversible manner, primarily due to temperature elevation. |
| Kubanek *et al.*, 2018 [78] | *C. elegans* nematodes | 10 | 0.3-1 | Transmission mode: PW<br>Sonication duration: 200 ms<br>Duty cycle = 50% | Acoustic pressure = 1MPa | FUS elicited behavioural responses in mutants lacking thermal sensitivity, with absent FUS-induced effects in mutants with removed mechanosensitive channels. |

*$I_{SPTA}$ (Spatial-Peak, Temporal-Average Intensity), $I_{SPPA}$ (Spatial-Peak, Pulse-Average Intensity) and $I_{TA}$(Temporal-Average Intensity).
*CAPs (Compound Action Potentials)

Table 2 - Summary of UNMOD parameters and outcomes from selected *in vivo* small and large animals' studies of the CNS.

| Author/Year | Target Region | Frequency (MHz) | PRF (kHz) | Other acoustic parameters | Energy | Outcomes |
|---|---|---|---|---|---|---|
| Tufail *et al.*, 2010 [25] | Mice motor cortex [(1)] and Mice hippocampus [(2)] | 0.25-0.5 | 1.2-3 | Transmission mode: PW<br>Sonication duration: 26-333 ms<br>Pulse duration: 0.16-0.57 ms<br>Cycles per pulse: 80-225 | $I_{SPTA}$ = 0.021-0.163 W/cm$^2$<br>$I_{SPPA}$ = 0.075-0.229 W/cm$^2$ | Bimodal transcranial US:<br>[(1)] triggered LFPs and motor responses;<br>[(2)] elicited TTX-sensitive neuronal activity, supressing LFPs in the CA1.<br>Temperature rise lesser than 0.01 °C. |
| Yoo *et al.*, 2011 [38] | Rabbit motor cortex [(1)] and Rabbit visual cortex [(2)] | 0.69 | 0.1 | Transmission mode: PW<br>Sonication duration: 50 ms [(1)] and 0.5 ms [(2)] | $I_{SPTA}$ = 6.3 W/cm$^2$ [(1)] and 160-320 mW/cm$^2$ [(2)]<br>$I_{SPPA}$ = 12.6 W/cm$^2$ [(1)] and 13.5 ± 3.8 mW/cm$^2$ [(2)] | Bimodal FUS:<br>[(1)] elicited motor cortex activity, triggering motor responses;<br>[(2)] decreased 30 VEP component magnitude. |
| Yoo *et al.*, 2011 [68] | Rat thalamus | 0.65 | 0.1 | Transmission mode: PW<br>Sonication duration: 0.5 ms | $I_{SPTA}$ = 3.3 W/ cm$^2$<br>$I_{SPPA}$ = 6 W/cm$^2$ | tFUS decreased anesthesia time. |
| King *et al.*, 2013 [56] | Mice motor cortex | 0.25-0.6 | 1.5 | Transmission mode: CW and PW<br>Sonication duration: 20-480 ms<br>Duty cycle: 30% | I = 0.01- 79.02 W/cm$^2$ | Transcranial US elicited motor responses (transient muscle contractions). The stimulation success increased as the US carrier frequency is lowered and the anesthesia level lightened. |
| Younan *et al.*, 2013 [69] | Rat motor cortex | 0.32 | 2 | Transmission mode: PW<br>Sonication duration:250-500 ms<br>Pulse duration:0.23 ms<br>Cycles per pulse:75<br>Duty cycle: 50% | $I_{SPPA}$ = 17.5 ± 7.5 W/cm$^2$ | Transcranial US elicited motor responses. |
| Deffieux *et al.*, 2013 [70] | Monkey left frontal eye field | 0.32 | – | Transmission mode: PW<br>Pulse duration: 100 ms | $I_{SPTA}$ = 4 ± 1.1 W/cm$^2$<br>$I_{SPPA}$ = 13.5 ± 3.8 mW/cm$^2$ | LIFUS modulated AS latencies during trained visual task. |

| | | | | | | |
|---|---|---|---|---|---|---|
| Ye *et al.*, 2016 [73] | Mice motor cortex | 0.3-2.9 | – | Transmission mode: CW<br>Pulse duration:80 ms | $I_{SPPA}$ = 0.02 - 127 W/cm$^2$ | FUS was capable of eliciting EMG activity and motor behaviour using either low or high frequencies |
| Lee *et al.*, 2016 [71] | Sheep primary sensorimotor (SM1)[(1)] and visual (V1)[(2)] cortices | 0.25 | 0.5 | Transmission mode: PW<br>Sonication duration: 300 ms<br>Pulse duration: 1 ms<br>Duty cycle: 50 %<br>Inter-stimulus interval: 5 s [(1)] and 1 s [(2)] | $I_{SPPA}$ = 3.4-11.8 W/cm$^2$ [(1)] and 1.7-14.3 W/cm$^2$ [(2)] | FUS:<br>[(1)] elicited MEPs (only on the contralateral right posterior limb), without any stimulation-related motor responses;<br>[(2)] elicited VEPs. |
| Sato et al., 2018 [85] | Mice posterior visual cortex | 0.5 | 1.5 | Transmission mode: PW<br>Sonication duration: 80 ms<br>Pulse duration: 0.2 ms<br>Cycles per pulse: 100 | $I_{SPTA}$ = 0.034-4.2 W/cm$^2$ | FUS and audible sound evoked similar cortical and motor responses. Chemical mice deafening reduced both responses. |
| Dallapiazza *et al.*, 2018 [72] | Pig thalamus (VPL) | 0.22–1.14 | 0.01 | Transmission mode: PW<br>Pulse duration:43.7 ms | $I_{SA}$ = 25-30 W/cm$^2$ | LIFUS supressed SSEP's amplitude |
| Baek *et al.*, 2018 [74] | Mice lateral cerebellar nucleus (LCN) | 0.35 | 1 | Transmission mode: PW<br>Sonication duration: 300 ms<br>Pulse duration: 0.5 ms<br>Duty cycle: 50 %<br>Inter-stimulus interval: 2 s | $I_{SPPA}$ = 2.54 W/cm$^2$ | LIFUS improved the sensorimotor performance and decreased brain edema as well as tissue swelling in mice recovering from ischemic injury. |

*$I_{SPTA}$ (Spatial-Peak, Temporal-Average Intensity), $I_{SPPA}$ (Spatial-Peak, Pulse-Average Intensity) and $I_{SA}$(Spatial-Average Intensity).

* LFP (Local Field Potential), VEP (Visual Evoked Potentials), AS (Anti-saccade), EMG (Electromyography), MEPs (Motor Evoked Potentials), SSEPs (Somatosensory Evoked Potentials).

Table 3 - Summary of UNMOD parameters and outcomes from selected *in vivo* humans' studies of the CNS.

| Author/Year | Target Region | Frequency (MHz) | PRF (kHz) | Other acoustic parameters | Energy | Outcomes |
|---|---|---|---|---|---|---|
| Legon *et al.*, 2014 [87] | Primary somatosensory cortex (S1) | 0.5 | 1 | Transmission mode: PW<br>Sonication duration: 0.5 s<br>Pulse duration: 0.36 ms<br>Cycles per pulse: 180 | $I_{SPPA}$ = 23.87 W/cm$^2$ | tFUS modulated (excited and supressed) the amplitude of short-latency SSEPs components and improved performance on sensory discrimination tasks. |
| Lee *et al.*, 2016 [76] | Primary and secondary somatosensory cortices (S1/S2) | 0.21 | 0.5 | Transmission mode: PW<br>Sonication duration: 500 ms<br>Duty cycle: 50 % | $I_{SPTA}$ = 17. 5 W/cm$^2$<br>$I_{SPPA}$ = 35 W/cm$^2$ | tFUS elicited transient contralateral tactile sensations (palmar/dorsal side of the hand and finger(s)). |
| Lee *et al.*, 2016 [88] | Primary visual cortex (V1) | 0.27 | 0.5 | Transmission mode: PW<br>Sonication duration: 300 ms<br>Pulse duration: 1 ms | $I_{SPPA}$ = 0.7-6.6 W/cm$^2$ | tFUS elicited phosphene perception, EEG peaks and the activation of stimulated regions and functions implicated in visual and higher-order cognitive processes |
| Monti *et al.*, 2016 [89] | Thalamus | 0.65 | 500 | Transmission mode: PW<br>Sonication duration: 30 s<br>Pulse duration: 500 ms<br>Duty cycle: 50 % | $I_{SPTA}$ = 720 mW/cm$^2$ | Pulsed LIFUS elicited a tolerable and safe recovery of motor and oromotor functions in post-traumatic DOC (case study) |
| Legon *et al.*, 2018 [90] | Primary motor cortex (M1) | 0.5 | 1 | Transmission mode: PW<br>Sonication duration: 0.5 ms<br>Cycles per pulse: 180<br>Inter-stimulus interval: 1-15 ms | $I_{SPTA}$ = 17.12 W/cm$^2$<br>$I_{SPPA}$ = 6.16 W/cm$^2$ | tFUS supressed MEPs and intracortical facilitation (with no effect in intracortical inhibition). Further than inhibiting motor cortical excitability, the reaction time on a motor task is also reduced |

*$I_{SPTA}$ (Spatial-Peak, Temporal-Average Intensity) and $I_{SPPA}$ (Spatial-Peak, Pulse-Average Intensity)

* SSEPs (Somatosensory Evoked Potentials), EEG (Electroencephalography), DOC (Disorder of Consciousness) and MEPs (Motor Evoked Potentials)

# Chapter 3

# Materials and Methods

## 3.1. Ultrasound Neuromodulation: Setup and Protocol

The implemented experimental sonication set2up, illustrated in Figure 15, was based upon previous *in vitro* [65, 66, 43] and *in vivo* [38, 68, 56] UNMOD studies. The implemented ultrasound system (Image Guided Therapy, France) was composed by a single-element focused ultrasound transducer with a fundamental frequency of 0.65 MHz (Figure 16), a control software along with a main cabinet ("Cube"), which accommodates a signal generator, power amplifier and an online water degassing system (Figure 17 a). This setup was installed next to a pre-existent electrophysiology setup (Figure 17 b), with the purpose of measuring the LIFUS-induced modulatory effects on neuronal activity in *ex vivo* brain slices. The electrophysiology setup and *ex vivo* brain slice preparation are later exposed in subchapter 3.2.

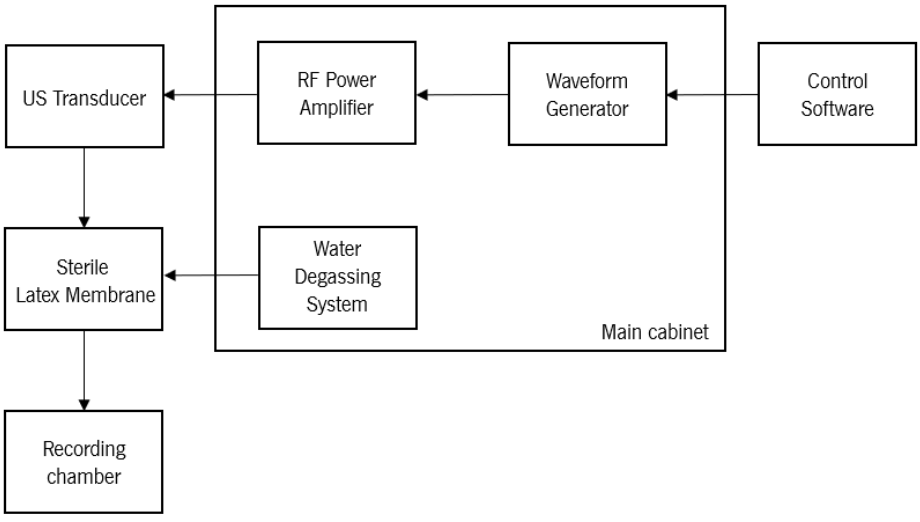


Figure 15 - Ultrasound setup block diagram.

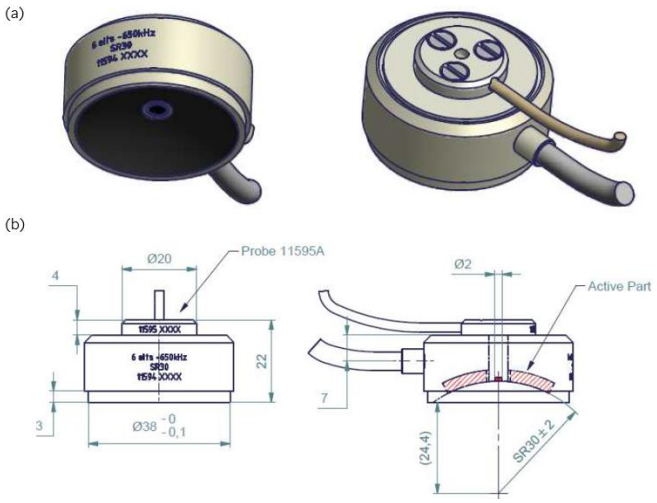


Figure 16 – Focused ultrasound transducer. (a) – Focused ultrasound transducer with a fundamental frequency of 0.65 MHz (Image Guided Therapy, France). (b) – Schematic of the transducer's mechanical specifications (Image Guided Therapy, France), namely the diameter (30 mm) and radius of curvature (24 mm).

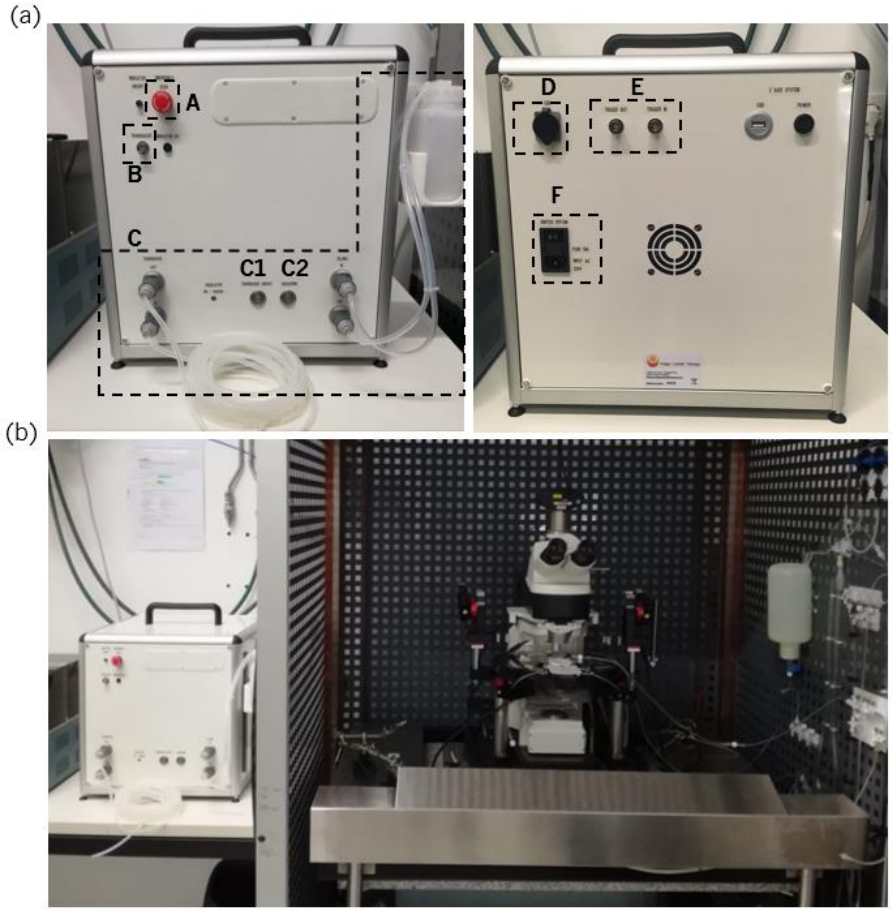


Figure 17 – Ultrasound setup. (a) - Main cabinet with signal generator and power amplifier. Right panel: (A) – Emergency button, (B) – Transducer output port, (C) - Water degassing system, (C1) – Transducer circuit button, (C2) – Degassing system button. Left panel: (D) – USB port for connecting the main cabinet to the laptop with the control software, (E) – Trigger Out and Trigger In ports, (F) – Power switch. (b) – Adaptation of the ultrasound system to the pre-existing electrophysiology recording setup.

The transducer was characterized by a focused US beam with a focal length between 2.0 and 4.0 mm. Therefore, the transducer must be positioned between 2.0 and 4.0 mm above the surface of the *ex vivo* brain slice in the recording chamber with a 3-axis micromanipulator (PatchStar Controller, Scientifica), allowing the user to modify its horizontal position if needed. Moreover, a sterile latex outer transducer cover (membrane) must be placed upon the US transducer and filled with degassed water, allowing the acoustic energy to be propagated through a medium without reflective particles and thus, guaranteeing the acoustic path to the target tissue and an efficient energy transmission. In order to avoid pressure problems and tubing break inside the degassing system, the degassing process must be first triggered by activating the transducer circuit and, when the transducer's cover is characterized by a good regime of water, the degassing circuit can be activated. Once the experiment is over, the degassing system must be emptied and if not, algae can form inside.

Regarding the transducer's energy supply, the 50 Watts signal generator can be used to deliver square pulses to a radiofrequency (RF) power amplifier, responsible for controlling the electric pulse since the transducer operates through high voltage pulses. Additionally, the signal generator must be connected to the laptop with a control system that enables the operator to adjust the acoustic parameters of the transmitted US (acoustic frequency, pulse duration, sonication duration, duty cycle, among others). This connection can be achieved by means of a Universal Serial Bus (USB). Moreover, to improve the signal-to–noise ratio (SNR) as well as to match the transducer's electrical impedance with the power amplifier's output impedance, the equipment can be connected with 50 Ω BNC connectors.

The distribution of the acoustic field during the US and target tissue interaction is influenced by the sonication parameters (carrier frequency, transmission mode, pulse repetition frequency, duty cycle, sonication duration and intensity). These parameters were selected in a wide range of values, based on the reviewed UNMOD literature, to test their efficiency in evoking or suppressing neuronal activity, in particular by applying low intensity FUS using pulsed *stimuli* along with a sonication duration in the range of 20-500 ms [56, 69], pulse duration within 0.0227-0.5 ms [43, 68] and a PRF of 0.1-2 kHz [43, 69].

### 3.1.1. Ultrasound Transducer Calibration

Before conducting US neuromodulation protocols it is necessary to first characterize the acoustic beam and output power levels of the transducer at the fundamental frequency using a pulsed transmission, namely through the measurement of the voltage waveforms generated by the US pressure waves with a calibrated needle hydrophone (HNR500; Onda, Sunnyvale, CA) in free water. The following

measurement protocol was based *in vivo* studies [56, 68]. Figure 18 illustrates the ultrasound setup for US transducer characterization and calibration.

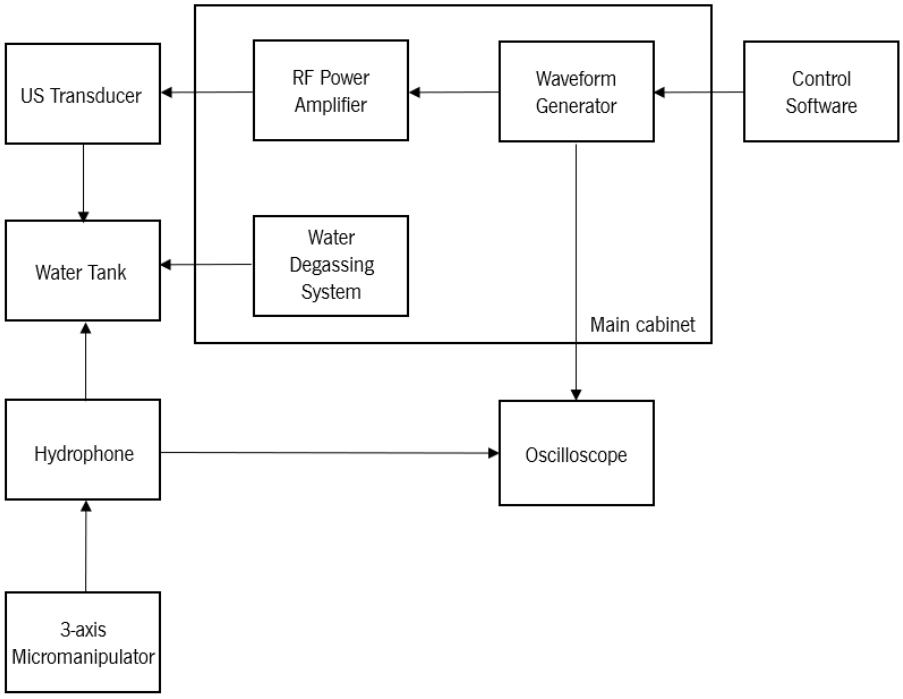


Figure 18 - Ultrasound setup block diagram for US transducer characterization and calibration.

The calibration process begins by immersing the US transducer, immobilized in a holder, in a water tank filled with degassed water (free field), with an oxygen percentage lower than 30%. Next, the needle hydrophone (Figure 19) is held by a 3-axis micromanipulator (PatchStar Controller, Scientifica) and placed in the water tank, aligned parallel to and vertically over the center of the US transducer. The hydrophone's output signal can be visualized in an oscilloscope (TDS3012B, Tektronix), while the output of the US main cabinet (Trigger Out output) must also be connected to the oscilloscope in view of synchronizing the US transmitter with the receiver (hydrophone).

A spatial sampling of the acoustic pressure field is conducted by moving the hydrophone position in the x-, y- and z-axis with the micromanipulator and in relation to the transducer, in order to find the acoustic maximum peak negative pressure, i.e., the transducer's focal point. Therefore, pressure field profiles can be created by measuring negative pressure amplitudes of the transducer's output at distinct spatial positions, which are later normalized according to the maximum measured spatial peak negative pressure. The measured voltage waveforms can be converted into pressure based on the hydrophone's table of voltage responses at different frequencies (provided by the hydrophone's manufacturer).

Acoustic exposure measurement such as the spatial-peak temporal average ($I_{SPTA}$), the spatial-peak pulse average ($I_{SPPA}$) and the mechanical index ($MI$) can be estimated according to published equations established by the American Institute for Ultrasound in Medicine and National Electronics Manufacturers Administration (see equations and safety regulatory standards in subchapter 2.1.2) and technical standards defined by the FDA [91].

After calibration, the transducer must be immersed in MiliQ water and left to dry, considering that it should never be cleaned with ethanol since it would instantaneously result in the break of the US device. Moreover, both the transducer's and hydrophone's faces are very sensitive and easily damaged, thus extra caution must be taken while maneuvering both devices to avoid touching or knocking the devices' surface.

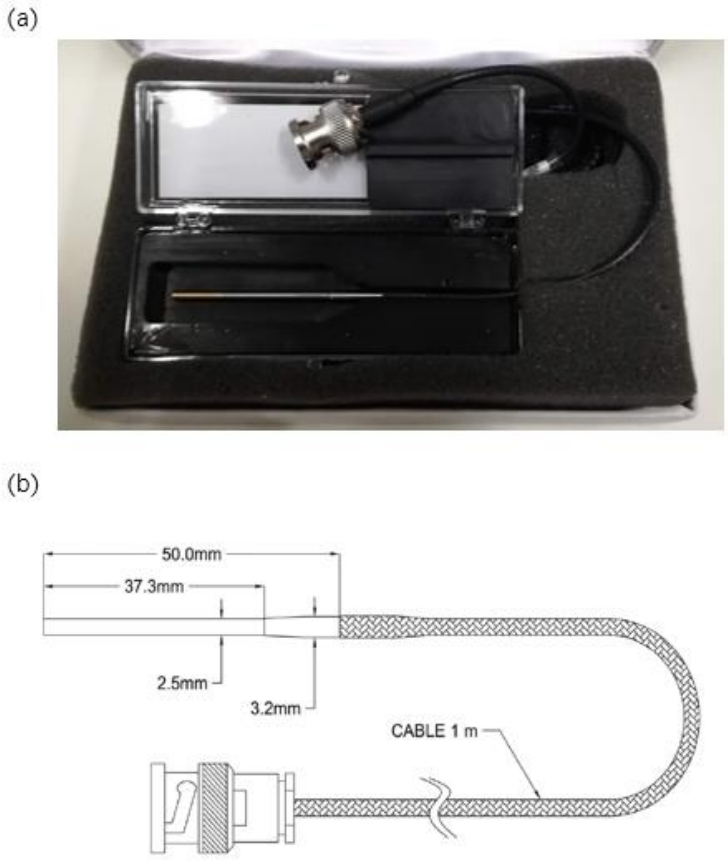


Figure 19 – Needle Hydrophone. (a) - HNR500 needle hydrophone (Onda, Sunnyvale, CA). (b) – Schematic of the hydrophone's mechanical specifications (Onda, Sunnyvale, CA).

## 3.2. Electrophysiology Recordings

### 3.2.1. Experimental Animals and Ethical Approval

A total of 15 mice of both genders, from the PV-cre+:Ai27D and SOM-cre:Ai27D transgenic lines, were used in this study. PV-cre:Ai27D animals were obtained by crossing homozygous PV-Cre mice (Jackson Laboratory, JAX 8069) [92] with homozygous Ai27D mice (Jackson Laboratory, JAX 012567) [93], while SOM-cre:Ai27D animals were obtained by crossing homozygous SOM-IRES-Cre mice (Jackson Laboratory, JAX 013044) with homozygous Ai27D mice (Jackson Laboratory, JAX 012567) [94]. Animals were housed under the following laboratory conditions: room temperature 22◦C, relative humidity of 55%, 12 h light cycle beginning at 8 a. m., food and water ad libitum.

Experiments were conducted in accordance with European Union Directive 2016/63/EU and the Portuguese regulations and laws on the protection of animals used for scientific purposes of the Ministry for Agriculture, Rural Development and Fishing. This study was approved by the Ethics Subcommittee for the Life Sciences and Health (SECVS) of University of Minho (SEVS 01/18) and the Portuguese Veterinary General Direction, Direção Geral de Alimentação e Veterinária (DGAV_8519).

### 3.2.2. Hippocampal and Habenula Coronal Brain Slices

#### 3.2.2.1. Solutions

Three solutions were prepared for hippocampal slice preparation, namely a standard artificial cerebral-spinal fluid (aCSF) solution (mM): 119 NaCl, 2.5 KCl, 1.2 $NaH_2PO_4$, 24 g $NaHCO_3$, 12.5 glucose, 2 $CaCl_2.2H_2O$ and 2 $MgSO_4.7H_2O$; a cutting N-methyl-D-glucamine (NMDG)-based aCSF solution (mM): 92 NMDG, 2.5 KCl, 1.20 $NaH_2PO_4$, 30 $NaHCO_3$, 20 HEPES, 25 glucose, 5 thiourea, 2 Na-ascorbate, 3 Na-pyruvate, 0.5 $CaCl_2.2H_2O$ and 10 $MgSO_4.7H_2O$; and an avertin (0.5 mg/g) intraperitoneal solution for animal anesthesia [95]. All chemicals were purchased from Sigma (Sigma-Aldrich).

The aCSF and NMDG-based aCSF solutions were titrated with concentrated hydrochloric acid to 7.2-7.4 pH and kept in Erlenmeyer flasks at room temperature. The osmolarity for each solution was measured and verified to be within 300-310 mOsm. Both solutions were carbogenated (95% $O_2$ and 5% $CO_2$) through bubbling stones both during brain slice preparation and subsequent electrophysiology

recordings, as to maintain a stable pH, lessen the slicing edema and assure the oxygenation of the slices during their preparation, recovery and incubation.

#### 3.2.2.2. Brain Slice Preparation

A glass beaker with carbogenated NMDG-based aCSF solution (previously prepared) was first placed in an incubation chamber at 37 °C, in which any air bubbles present in the solution were removed. A surgical area for animal perfusion was also prepared by laying out the dissection tools. All the animals were deeply anesthetized by avertin intraperitoneal injection. The surgical plane of anesthesia was reached when stimuli (tail or toe pinches) was inflicted with absent reflexes.

To prepare hippocampal brain slices the animals were transcardially perfused with NMDG-based aCSF solution [95, 96] . Afterwards, the animal was decapitated with scissors at the cervical medulla level and the skull removed. The brain was rapidly detached and glued with cyanoacrylate glue onto a cutting stage and placed in the slicing chamber of a Vibratome 1000 Plus (Leica Microsystems, USA), filled with carbogenated NMDG based-aCSF solution. Coronal brain (300 μm) were prepared with a transverse slicing angle [96].

The slices were recovered in NMDG-based aCSF solution (in the incubation chamber) for 11 minutes and then transferred to a holding chamber with room-temperature carbogenated regular aCSF, in order to be used in the next 1-8 h.

### 3.2.3. Cerebellar Longitudinal Brain Slices

#### 3.2.3.1. Solutions

Two solutions were prepared for cerebellar slice preparation, namely a standard artificial cerebral-spinal fluid (aCSF) solution (mM): 125 NaCl, 2.5 KCl, 1.2 $NaH_2PO_4$, 24 g $NaHCO_3$, 12.5 glucose, 2 $CaCl_2.2H_2O$ and 1 $MgSO_4.7H_2O$ [97] and an avertin intraperitoneal solution for animal anesthesia. All chemicals were purchased from Sigma (Sigma-Aldrich). Both solutions were prepared as explained in the previous subchapter.

#### 3.2.3.2. Brain Slice Preparation

The animals were decapitated with scissors at the cervical medulla and the skull removed. The cerebellum was detached from the forebrain by a coronal cut and quickly glued with cyanoacrylate glue

onto a cutting stage and placed in the slicing chamber of a Vibratome 1000 Plus (Leica Microsystems, USA), filled with carbogenated aCSF solution at 34°C. Longitudinal brain slices (300 μm) were prepared, while the bath temperature was monitored with a conventional mercury/glass thermometer and preserved at the desired temperature range by filling the external chamber of the slicer with warm or cold water. The slices were transferred to a holding chamber with carbogenated regular aCSF at 34°C and ready to be used during the following 1-8 h [97].

### 3.2.4. Extracellular Recordings' Setup

After recovery, coronal slices were transferred to a recording chamber and perfused with carbogenated aCSF at room temperature (20±2°C) (2 ml/minute rate); on the other hand, cerebellar slices were oxygenated with carbogenated aCSF at 34±2°C, (2 ml/minute rate) while the bath's temperature was maintained by an in-line solution heater and cooler, monitored through an automated temperature controller (TC-324B, Warner Instruments). The slices were visualized using a microscope (BX-51WI, Olympus), controlled by a 3-axis micromanipulator (PatchStar Controller, Scientifica).

The cellular layer of the hippocampus and the lateral portion of the habenula regions were targeted when using coronal slices, whereas the dentate nuclei (DN) was examined when using longitudinal slices. Tetrode visualization and placement was performed using a microscope (BX-51WI , Olympus) and a 3-axis micromanipulator (PatchStar Controller, Scientifica). All recordings were referenced to ground, by a silver chloride pellet electrode (E-202 Ag-AgCl electrode disk, Science Products) immersed in the recording chamber bath and connected to the EIB ground.

Extracellular activity was recorded by using an open-source acquisition system (Open Ephys) [98], composed by an acquisition board along with a 32-channel headstage (RHD2132, Intan) connected together by serial peripheral interface (SPI) cables (Intan). The extracellular electrodes' signals were sampled, amplified and digitally multiplexed at the headstage level, which was connected to the prototype's EIB with male Omnetics connectors (A79026-001, Omnetics). The recording chamber and the remaining experimental devices (apart from the temperature controller, acquisition board and computer) were mounted above an air table and inside a Faraday Cage, seeing that the recorded signals are very susceptible to mechanical vibrations and electromagnetic interference (EMI) noise. All devices were connected to a common ground. Figure 20 and 21 represent the extracellular recordings' setup.

The Open Ephys graphical user interface (GUI) [98] – Windows plugin-based application - was employed for signal acquisition and visualization of each recording site, as neuronal electrophysiology

data was sampled at 30 kHz and bandpass filtered between 0.3 and 6 kHz (Figure 22). Recordings of up to 10 minutes were made for each slice region for subsequent processing and analysis in MATLAB software (MathWorks). The tetrodes' data was saved in both Open Ephys native format and raw binary format for subsequent offline analysis.

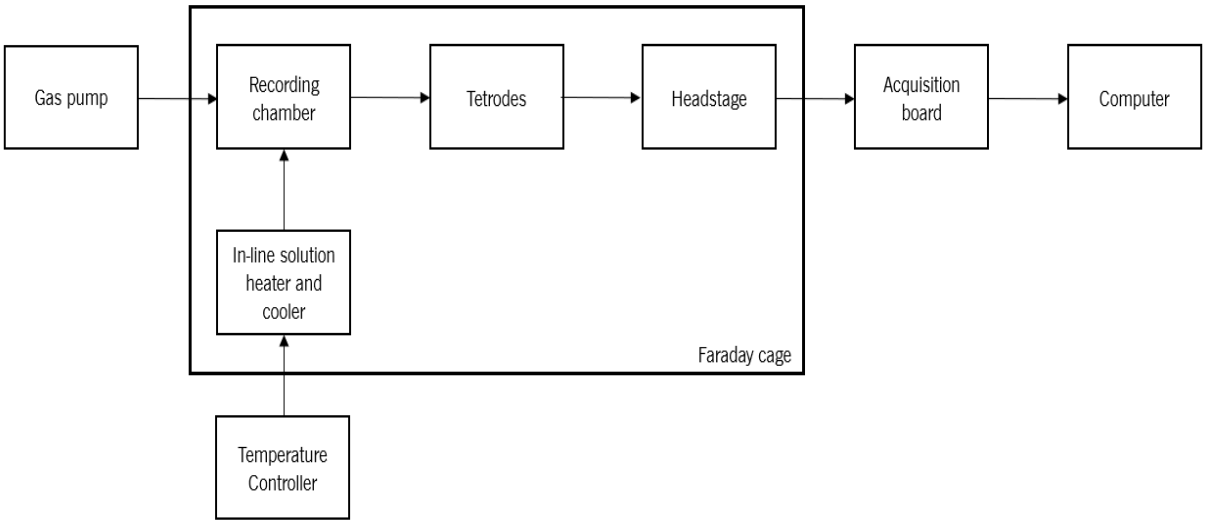


Figure 20 – Extracellular recordings' setup block diagram.


Figure 21 - Extracellular recordings' setup. (A) – in-line solution heater and cooler. (B) – recording chamber. (C) – 32-channels headstage. (D) – microscope. (E) – 3-axis micromanipulator, (F) – SPI cable, (G) – 3-axis micromanipulator control cube. (H) - automated temperature controller. (I) – Open Ephys acquisition board.

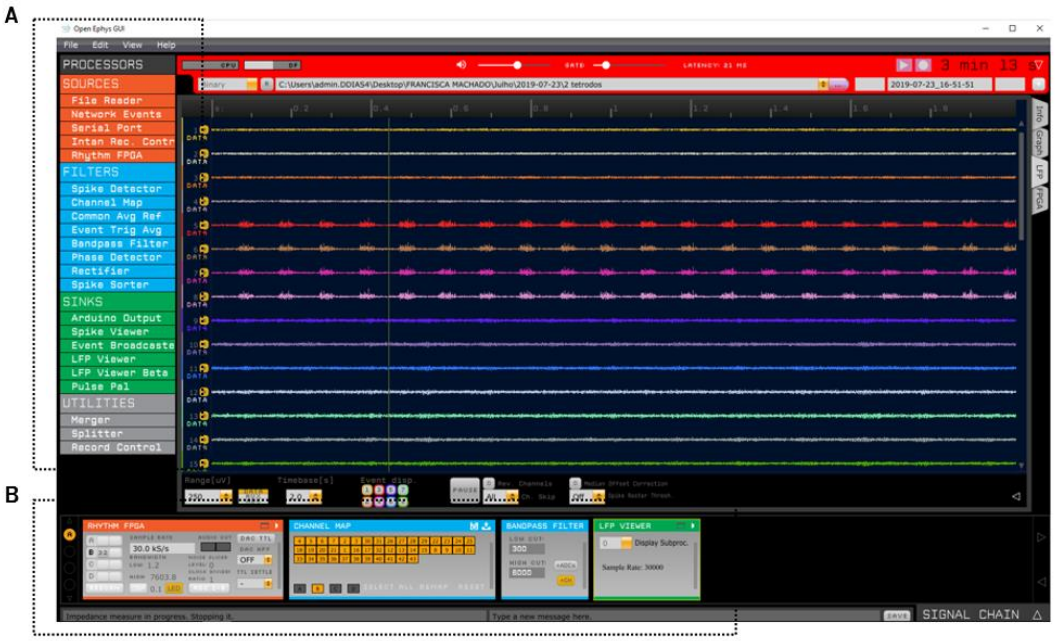


Figure 22 – Open Ephys GUI. (A) – data processing modules ("Sources", "Filters", "Sinks", "Utilities"). (B) – processing pipeline.

## 3.3. Prototypes for Tetrode Recordings in Brain Slices

### 3.3.1. Impedance Measurement

Towards the selection of an appropriate wire for tetrode fabrication, impedance measurements were carried out in different wires with a nanoZ multi-electrode impedance tester (White Matter LLC, USA), which computes the impedance magnitude and phase through sine wave excitation with a small current (0.1 μA).

Electrode wires were loaded to a 32-channel Omnetics electrode interface board (EIB) (Open Ephys) [99], which in turn was connected to the nanoZ tester through an ADPT-NZ-N2T-32 adaptor (NeuraLynx, USA). The impedance was measured in relation to a low impedance stainless steel reference with all electrodes fully submerged in a saline solution (0.9% NaCl) and apart from each other. A copper wire served as EIB ground and was also submerged in the saline solution along with the reference and test electrodes, as seen in Figure 23. Eight impedance measurements were conducted for each electrode wire through the Windows based nanoZ application (White Matter LLC, USA), at a constant frequency of 1040 Hz.

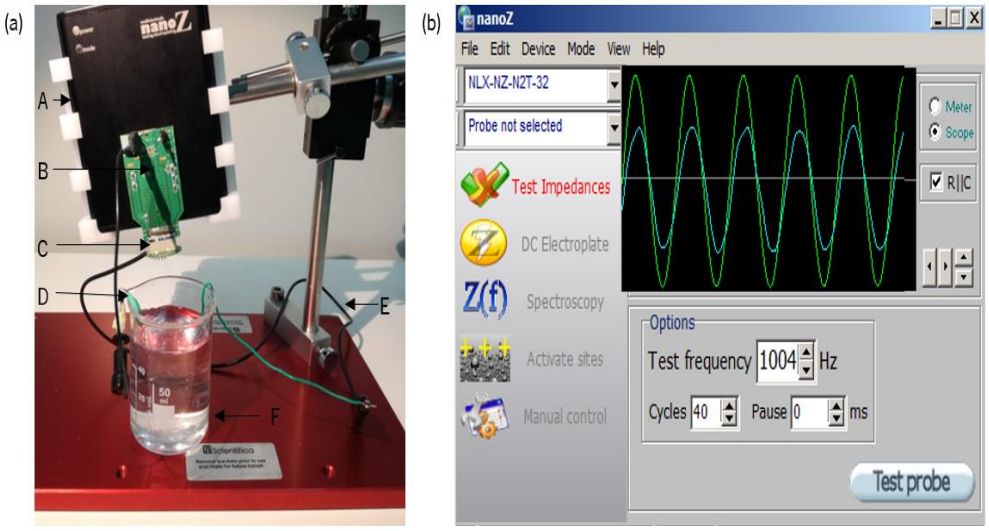


Figure 23 - Impedance measurement setup. (a): (A) – nanoZ™, (B) – ADPT-NZ-N2T-32 adaptor, (C) – 32-channel Omnetics electrode interface board, (D) – reference electrode, (E) – electrode interface board ground wire, (F) – saline. (b): Windows based nanoZ application in "Test Impedances" mode.

## 3.3.2. Tetrode Fabrication and Electroplating

### 3.3.2.1. Tetrode Fabrication

In accordance to previous published methods *[100, 101]*, the tetrodes were fabricated by twisting four 12.5 µm diameter nichrome (Redi Ohm 800, Hard PAC) wires (Sandvik, USA) and heat-fusing their insulation, with the aid of the setup presented in Figure 24.

Briefly, tetrode fabrication began by twisting a folded wire tensioned in a horizontal metal bar (in a direct hang down position) and attached to a motorized Tetrode Spinner 2.0 (NeuraLynx, USA). Subsequently to the tetrode twisting procedure, the wires insulation was fused at 420 °C with the aid of a heat gun (RYOBI) in order to lock the wires together as well as to achieve increased mechanical rigidity while avoiding short-circuits. The tetrode was then cut at the tip and stored in a box to prevent dust and other debris from accumulating.

The quality of the fabricated tetrodes was evaluated according to their physical and mechanical properties, knowing that a proper tetrode should look like a single straight and rigid wire with tight loops and that does not have ruptures or lose ends. Furthermore, the tetrodes were discarded if any of the following situations occurred: wire break or split; curling of the wires during the spinning process; rupture of the wire's insulation during the fusing process (visible since the wire changes in color).

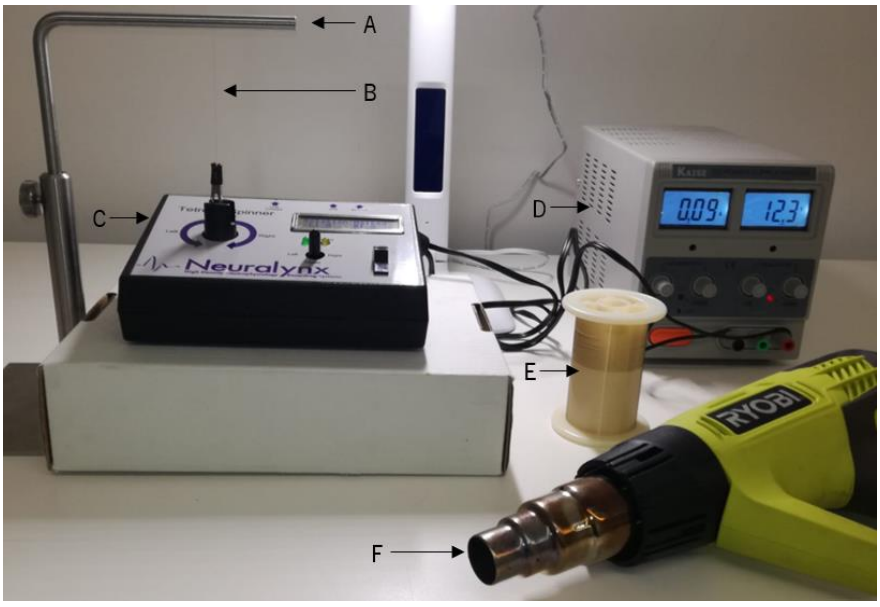


Figure 24 – Tetrode fabrication setup. (A) – horizontal metal bar. (B) – tetrode. (C) – tetrode spinner. (D) – power supply. (E) – 12.5 µm nichrome wire. (F) – heat gun.

#### 3.3.2.2. Gold Plating of Tetrodes

With the purpose of obtaining electrodes with impedances in the range of 70 and 100 kΩ, the nichrome tetrode wires were electroplated. The plating solution was obtained by combining 0.375 mL of gold plating solution (10ml Gold Plating Solution, Neuralynx, USA) with 0,01125 g of PEG addictive (Poly(ethylene glycol) BioUltra, 8,000, Sigma-Aldrich) dissolved in 1,125 mL of MiliQ water. PEG worked as an electroplating inhibitor by promoting the deposition of new gold particles to the detriment of the nonstop development of existing particles, thus preventing shorting and resulting in large surface area electrodes. This process improves the SNR and facilitates the recording of extracellular activity through the enhancement of the tetrode's biocompatibility and the matching of the electrode's impedance, resulting in more reliable and consistent neuronal signal recordings [100, 101]. The electroplating set up is illustrated in Figure 25.

Previously to electroplating, the tetrodes were cut at the tip with micro-serrated stainless scissors (14058-09, Fine Scientific Tools). The cut was performed in a swift and gentle single movement, simplified by partially immobilizing the scissors with a vice, since this procedure can change the electrodes' impedance by reducing the diameter of the wires through crushing and if ill-made can provoke wire shorting. The quality of the cut was checked under a microscope (SZ51, Olympus), namely for the presence of damaged wires or insulations, as well as the occurrence of wires shorting. The tetrodes were then submitted to an impedance measurement.

At the start of the electroplating procedure, +0.1 μA DC current was applied to each wire for 1 second in order to clean its exposed surface [102]. The electroplating was then conducted in the nanoZ Windows based application by supplying a negative DC current (-0.05 μA) in consecutive steps of varying duration, according to the NeuraLynx plating protocol (Table 4) [103].

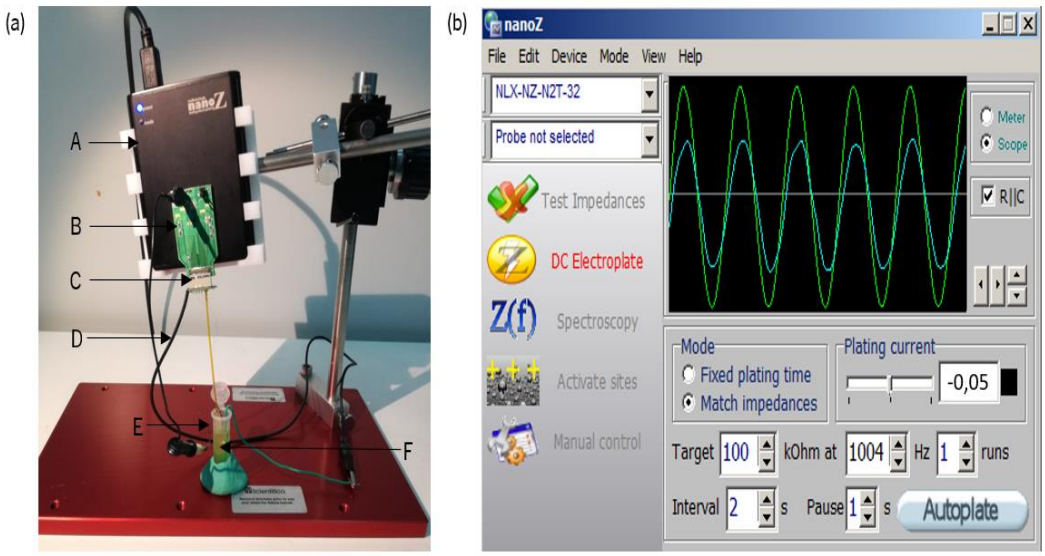


Figure 25 –DC Electroplating setup. (a): (A) – nanoZ, (B) – ADPT-NZ-N2T-32 adaptor, (C) – 32-channel Omnetics electrode interface board (EIB), (D) – electrode interface board ground wire, (E) – reference electrode, (F) – gold plating solution with PEG inhibitor. (b): Windows based nanoZ application in "DC Electroplate" mode.

Table 4 – NeuraLynx plating protocol (adapted from [103]).

| Step | Time (s) | DC Current (μA) | Impedance Target (MΩ) | Number of attempts |
|---|---|---|---|---|
| Cleaning | 1 | +0.1 | n/a | 1 |
| 1 | 15 | -0.05 | 2 | 3 |
| 2 | 10 | -0.05 | 1.5 | 3 |
| 3 | 5 | -0.05 | 0.5 | 3 |
| 4 | 3 | -0.05 | 0.25 | 3 |
| 5 | 2 | -0.05 | 0.1 | 3 |
| 6 | 2 | -0.05 | 0.7 | 3 |

Impedances were reduced to below 100 kΩ. Wire shorting was signaled through the existence of impedances below 70 kΩ in all wires of the same tetrode. In the presence of short-circuits, two solutions were employed to remove the excess gold layers: (1) - application of a current with reverse polarity (+0.1 μA) followed by the repetition of the impedance measurement and gold electroplating processes; (2) – repetition of the tetrode's tips cut and gold electroplating process [101, 103]. Posteriorly to electroplating, the tetrodes were lifted from the plating solution and lowered into MiliQ water to clean the gold crystallites excess for 1 to 2 seconds; after, they were air dried.

#### 3.3.2.3. First Prototype: Design and Conception

An insulated copper wire was glued to one of the ground pins on the EIB (Open Ephys) with conductive silver glue (SCP Silver Conductive Paint, Electrolube) and later with of epoxy glue (5 min Epoxy, Devcon), to stiffen and protect the connection. This wire was afterwards used to ground the recording setup with the purpose of eliminating potential noise interference.

The support structure for loading the tetrodes to the EIB was built with 3 cm and 8 cm long medical grade polyimide tubes (ID = 0.114 mm and ID = 1.04 mm, respectively) (Science Products, GmbH, Germany). The 3 cm polyimide tubes served as tetrode guides and were used for tetrode loading- with the number of tubes varying according to the number of tetrodes to be loaded – while one 8 cm tube served to structurally hold the tetrode guides and connect to the EIB creating a single structurally cohesive device. This process is illustrated in Figure 26.

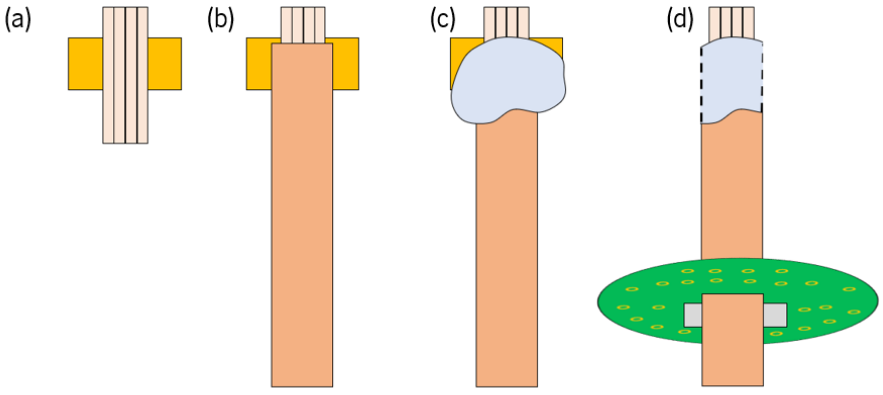


Figure 26 – Support structure for tetrode load assembly. (a) – Alignment of four 3 cm long polyimide guide in folded tape. (b) – Fixation of an 8 cm long polyimide tube with cyanoacrylate glue on top of the guide tube assembly. (c) – Deposition of epoxy glue. (d) – Tape removal and epoxy glue excess cut; fixation of the 8 cm long polyimide tube in the EIB with cyanoacrylate glue on top of the guide tube assembly.

Finally, the tetrodes were loaded through the guide tubes with the aid of a microscope (SZ51, Olympus), allowing each tetrode tip to project 0.5 -1.0 cm from the guide tubes (opposite to the EIB). Each tetrode wire was connected to the EIB by pressing a small gold-plated pin (Open Ephys) with the aid of a pair of tweezers through the gold plated EIB electrode holes simultaneously securing the wire in place and stripping its insulation thus creating electrical contact (Figure 27). To ensure tetrode stability, each tetrode was glued to the small 3 cm long polyimide tubes with a drop of cyanoacrylate glue (Super Glue, Loctite).

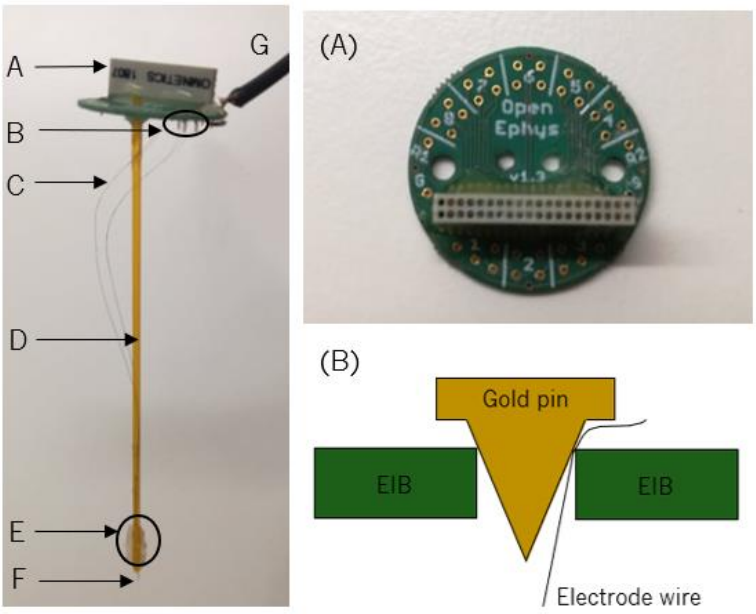


Figure 27 – First extracellular recording prototype for brain slices based on tetrodes. (A) – Electrode-Interface-Board (EIB). (B) – gold pins. (C) – 12.5 µm diameter nichrome tetrodes. (D) – 8 cm long polyimide tube (ID=1.04 mm). (E) – 3 cm long polyimide guide tubes (ID=0.114 mm). (F) – tetrodes' recording tips. (G) – GND wire.

## 3.3.3. Final Prototype: Design and Conception

### 3.3.3.1. Tetrodes' Support Structure Design

The structure to physically hold and guide the tetrodes' support (tetrode support structure) (Figure 28 a) was designed in AutoCAD software with a probe like shape, with a single groove track for tetrode insertion and fixation. Furthermore, features such as rectangular openings and screw holes (ID = 2.70 mm) were added as to facilitate prototype handling reducing potential damage to the tetrode wires. The tetrodes support structure was 3-D printed in Nylon 12 (PA12) multijet fusion plastic. Two 3D models

were produced, namely with a track for loading four tetrodes (30 mm length x 0.3 mm width x 0.3 mm depth) and another one for eight tetrodes (30 mm length x 0.6 mm width x 0.6 mm depth) although the track can be designed to hold any number of tetrodes. The whole support structure was characterized by a 70 mm length, 10 mm back width, 1.5 mm tip width and 1.5 mm depth.

#### 3.3.3.2. Electrode Interface Board Design

The electrode interface board's structure was first design in AutoCAD software and similarly to the support, matching rectangular openings and screw holes (ID = 2.70 mm) features were added to the 3D model (Figure 28 b). The whole EIB structure was characterized by a 66 mm length, 30 mm back width, 10 mm tip width and 1.5 mm depth. Additionally, this structure was created with a large bottom width in order to facilitate the tetrode apparatus handling and thus, reducing the probability to bend or break the tetrodes' wires. The final structure layout, i.e., the merge between the designed tetrodes' support and electrode interface board parts) was characterized by a total length of 100 mm, as illustrated in Figure 7 (c).

A printed circuit board (PCB) was designed in Eagle software, which was responsible for the mechanical support and electrical connection between components such as a 32-channel Omnetics connector (Omnetics Connector Corporation, A79024-001) and gold-plated electrode holes (same as the on the Open Ephys EIB).

The designed AutoCAD part described above was converted into a .DXF file and imported into the Eagle software, serving as an outline for board design (Figure 30). The Omnetics connector component's pads were positioned in the center of the structure's bottom (at wider end). The electro holes were divided in two areas mounted symmetrically in the vertical plane, with printed marks on the board that divided the electro holes into groups of four, which allowed to keep track of the loaded tetrodes' positions considering that each tetrode is composed by four electrodes. Two ground holes and two reference holes were first placed in opposite sides to the vertical plane, right above the Omnetics connector. The EIB PCB was manufactured by JLCPCB (China) with electroless nickel immersion gold (ENIG) surface plating.

The Omnetics connector (A79024-001, Omnetics Connector Corporation) was soldered to the tetrode's device connector pads by hot air soldering with solder paste (Leaded, No Clean Solder Paste, MG Chemicals).

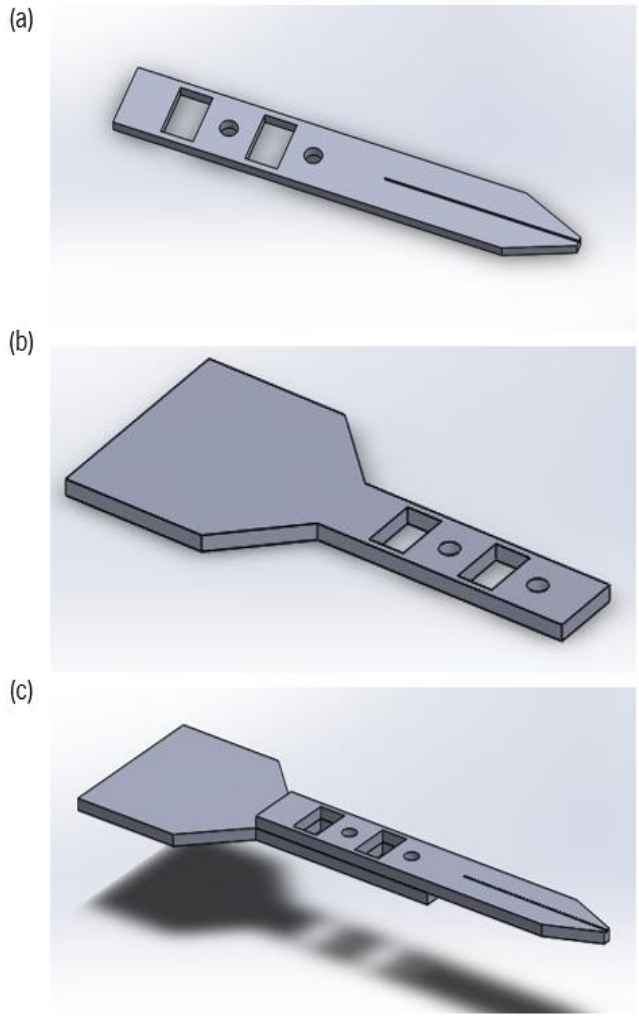


Figure 28 – 3D model of the recording prototype design on AutoCAD software. (a) - Tetrode support structure. (b) - Electrode interface board structure. (c) - Tetrode support and electrode interface board parts combined.

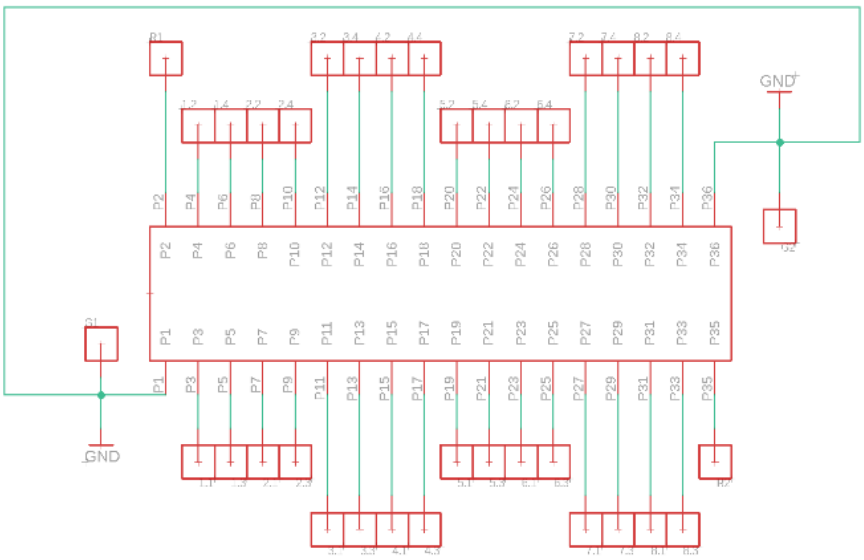


Figure 29 – Electrode interface board design on Eagle software: schematic design.

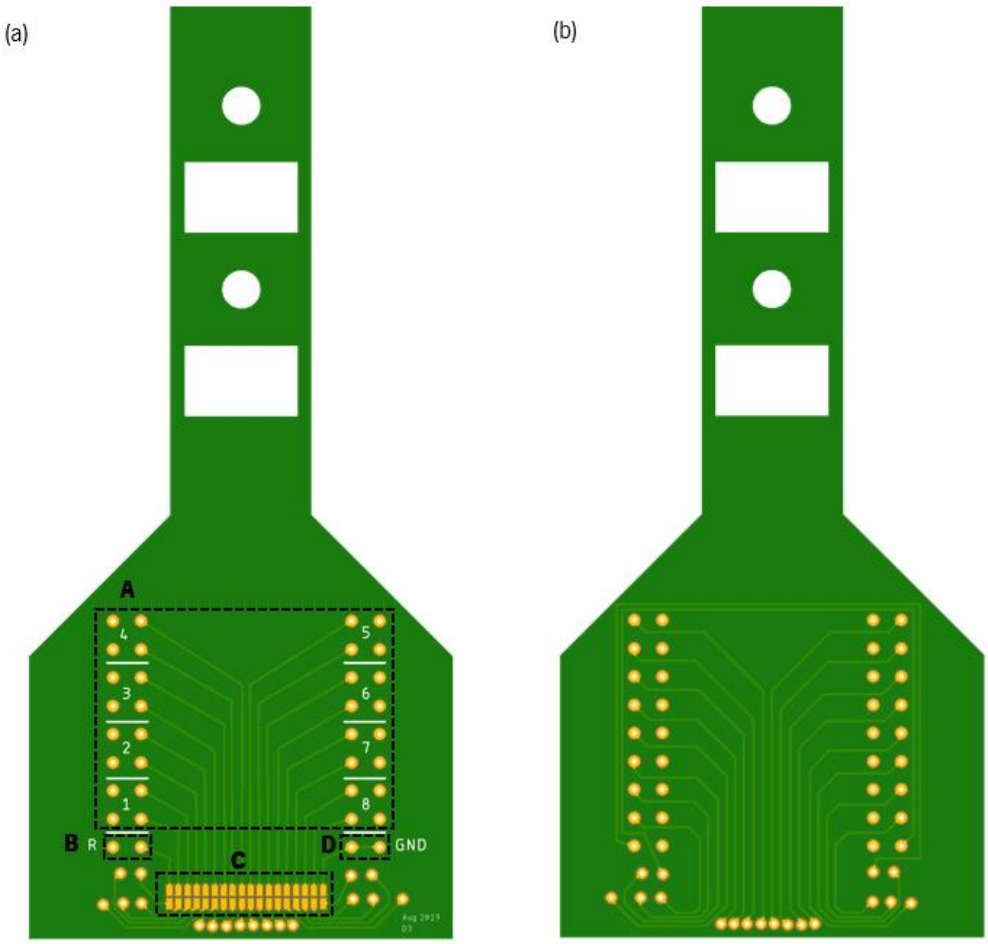


Figure 30 – Electrode interface board design on Eagle software. (a) – Front view: (A) – tetrode holes, (B) – reference holes, (C) – connector pads, (D) – ground holes). (b) – Back view.

## 3.4. Extracellular Neuronal Activity Processing and Analysis

### 3.4.1. Spike Detection

Spike detection was achieved by applying an amplitude threshold ($Th$) according to the algorithm published by Quiroga *et al.* (2004) [104]. As seen in Equations 19 and 20, the $Th$ was set as a multiple (in Equation 19 defined as four) of an estimation of the noise standard deviation ($\sigma_n$), in which $x$ corresponded to the bandpass filtered signal. The use of threshold based on the median absolute deviation of the filtered improves the discrimination of high amplitude signals (spikes) in the neighborhood

of low amplitude background activity when compared, for example, with other spike detection methods based on the root mean square (RMS) of the signal. The threshold value was adjusted in the analysis of each individual recording by changing the multiplier factor of $\sigma_n$ (Equation 19), considering that if the $Th$ was too high lower-amplitude spikes would possibly not be discriminated and, otherwise, if too low it would lead to the detection of background activity.

Furthermore, a peak-to-peak distance threshold was also used to prevent multiple detections in the same spike waveform, where a time window was defined for which no spike can be detected after a threshold crossing event (considering that the refractory period is of at least 1 ms for the majority of cells [105]). Figure 31 summarizes the steps performed to obtain spike detection. Off-line data pre-processing was not executed previously to spike detection since the signal was already bandpass filtered (0.3-6 kHz) during extracellular recordings.

$$Th = 4\sigma_n \qquad (19)$$

$$\sigma_n = median\left\{\frac{|x|}{0.6745}\right\} \qquad (20)$$

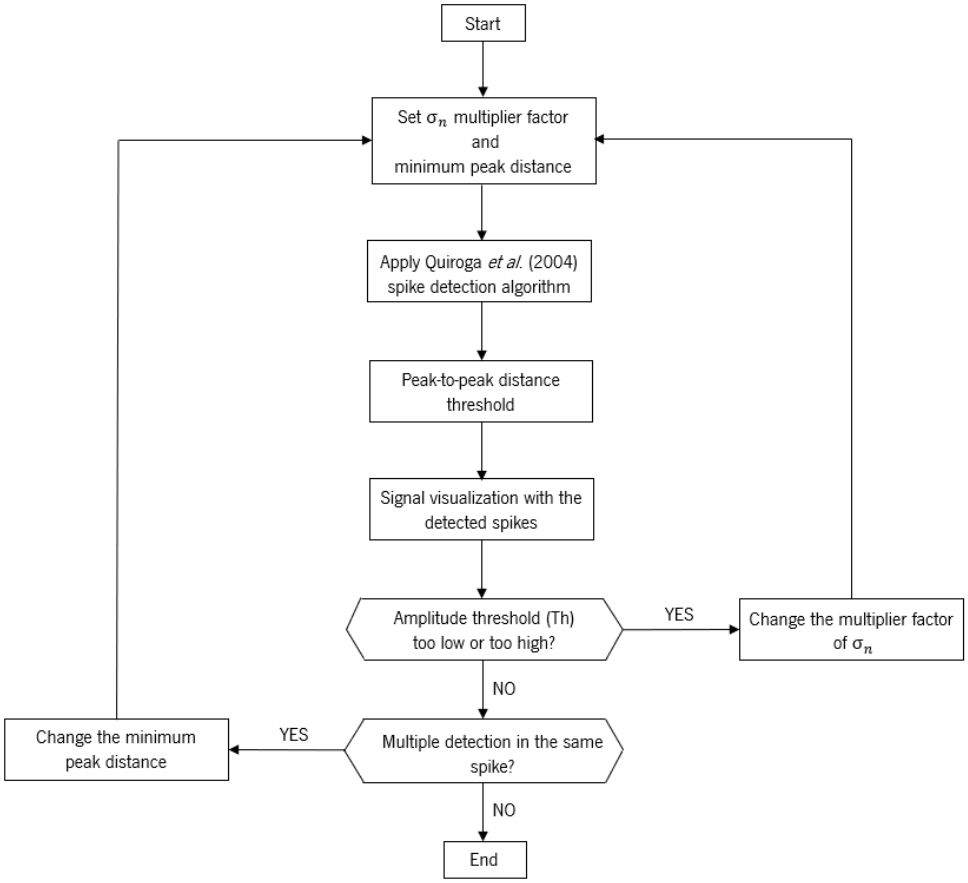


Figure 31 – Spike detection algorithm flowchart.

### 3.4.2. Spike Sorting

In order to isolate the activity of putative single neurons, a new semi-supervised spike sorting algorithm was developed in this dissertation. This algorithm was used to extract features from detected spikes and group them into clusters assigned to the activity of distinct neurons. Furthermore, to validate the new algorithm developed in the current work an open-source toolbox called "WaveClus" was used to compare the spike sorting performance.

#### 3.4.2.1. Semi-Supervised Spike Sorting

The newly developed semi-supervised spike sorting algorithm automatically tests various clustering possibilities and selects the one that yields the best clustering results within the data space. At the end of the automatic procedure the user can manually select in a supervised way which clusters to keep for further analysis.

Spike detection was achieved with the previously described algorithm, employing amplitude and peak-to-peak distance thresholds to separate the action potentials from background activity or noise. Subsequently, feature extraction was performed by selecting the maximum amplitude of each detected spike (peak amplitude) on all four tetrode channels.

Next, extracted feature values of all possible electrode pairs (called 2D projections) were classified into clusters using K-means clustering, which was chosen due to its easy implementation and efficient computation. This unsupervised machine-learning clustering method partitions $m$ objects of a dataset $X$ into $k$ groups, assigning each object to the cluster with the closest mean, while using the squared Euclidean distance metric as a proximity measure. The initial "mean" is randomly generated within the data space and is iteratively updated after object assignment until convergence is reached, i.e., until no further changes in mean are possible due to object re-assignment, or until a predefined number of iterations is reached.

Since the number of clusters that possibly exist in the experimental data is not initially known the optimal $k$ numbers of clusters are automatically selected by the algorithm through an assessment measure of the clustering procedure by the silhouette method. This method calculates how distant each point in one cluster is to the mean of the closest neighboring cluster. By calculating the mean silhouette value of each cluster, i.e. the average of the silhouette values of all points within a cluster, one gets an approximate estimate of how separate each cluster is from its neighboring clusters. Averaging the mean

silhouette values of all clusters can be used as an estimate of how well the total number of clusters is separate from each other. The developed algorithm thus uses the mean silhouette value of all clusters to automatically select not only what is the number of clusters $k$ that maximizes data separation, but also what is the 2D projection – i.e. the pair of tetrode electrodes - within each $k$ that achieves the best cluster separation. Briefly, the algorithm calculates the mean silhouette value for all clusters for $k$ values from 2 to 5 for all possible pair of electrodes' combinations and simultaneously selects how many clusters (i.e., which k) and which electrode combination yields the highest mean silhouette value. The user is then presented with the spike waveforms as well as the distribution of spike peak amplitudes of each these clusters. This allows the user to manually select in a supervised way which clusters to accept and which to reject. The remaining data analysis/processing of the data is performed based on the selected clusters by the user.

The develop algorithm is based upon four main steps: (1) - spike detection, (2) - feature extraction and (3) - spike sorting using K-means clustering (4) manual cluster selection. Figure 32 summarizes the steps performed to obtain this semi-supervised algorithm.

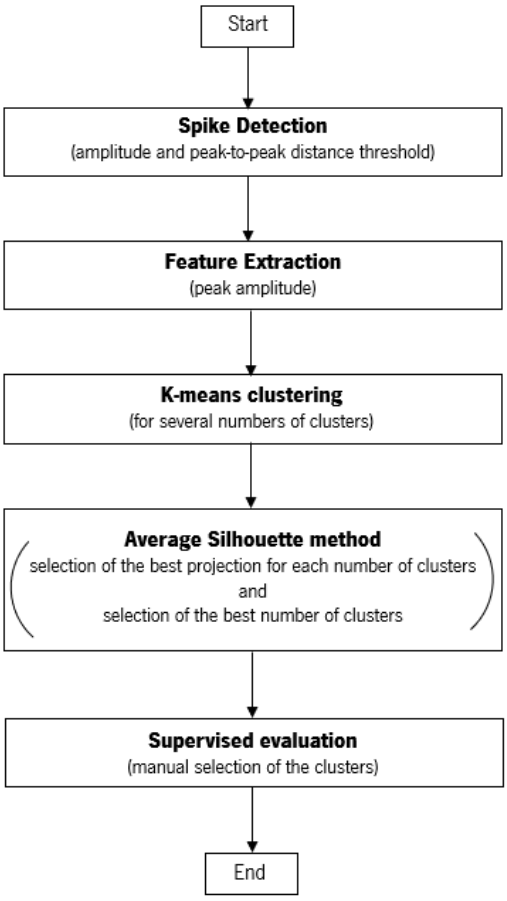


Figure 32 - Semi-supervised spike sorting algorithm flowchart.

#### 3.4.2.2. Wave Clus

Spike detection and spike sorting were also performed with the open-source software "Wave Clus" [104]. The software applies an automated algorithm for detecting and separating spikes correspondent to distinct neurons, namely by using PCA (or wavelets) for feature extraction and super-paramagnetic clustering (SPC). The selected coefficients for optimal spike separation serve as input parameters for the SPC clustering, which is based upon the K-nearest neighbor interaction and in the automatic selection of the corresponding superparamagnetic phase's temperature, knowing that in order to find the optimal clustering temperature the algorithm calculates results for all temperatures in a superparamagnetic regime. This software allows the user to visualize the clustering results in a MATLAB GUI (Figure 33).

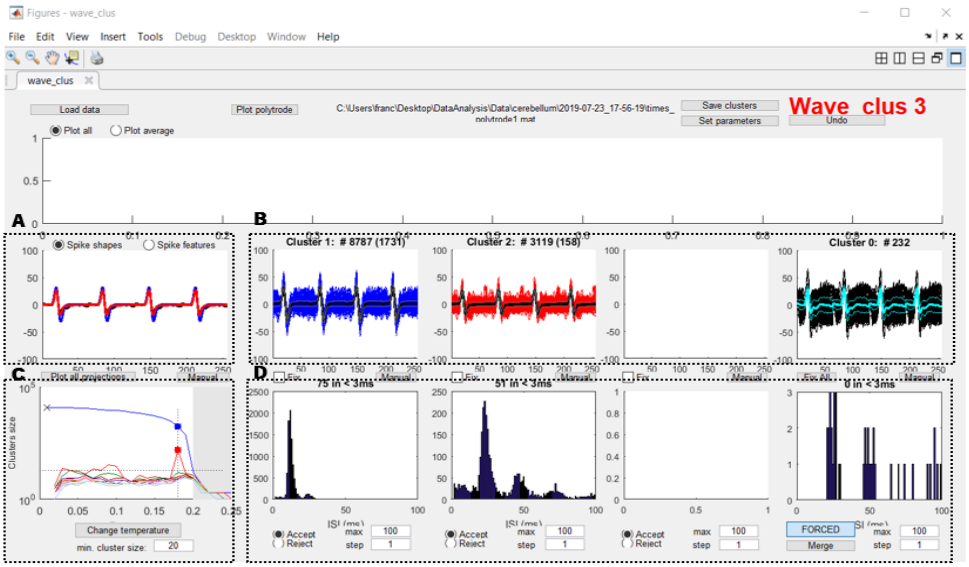


Figure 33 – Wave Clus GUI. (A) – Spike shapes' plot of all the clusters. (B) – Spikes' shapes for each cluster in all of the four tetrode's channels. (C) – temperature map of the superparamagnetic clustering. (D) – interspike interval (ISI) histogram for each cluster.

## 3.5. Optogenetic Stimulation: Setup and Protocol

Brain slices were illuminated with blue light pulses (470 nm wavelength) at 10 Hz with 50 ms pulse width. Pulse trains were delivered for 10 s in intervals of 60 s as to induce acute effects of optogenetic modulation.

The optical pulse trains were delivered by using a fiber-coupled LED source (470 nm, 10 mW) (Thorlabs, M470F3) connected to a LED driver (Thorlabs, T-Cube), in which the optical fiber (ID = 400 µm, Thorlabs) was held by a 3-axis micromanipulator (Scientifica) and directly placed in the recording

chamber near to the recording electrodes and above the slice, with the microscope's visual aid. The pulse trains were generated in a waveform generator (DG1022, Rigol), which was connected to the LED driver and to the acquisition board through an I/O board (Open Ephys), with the purpose of recording the stimulation pulse trains simultaneously with the extracellular activity in the Open Ephys GUI. Figure 34 presents the block diagram of the previously described set up.

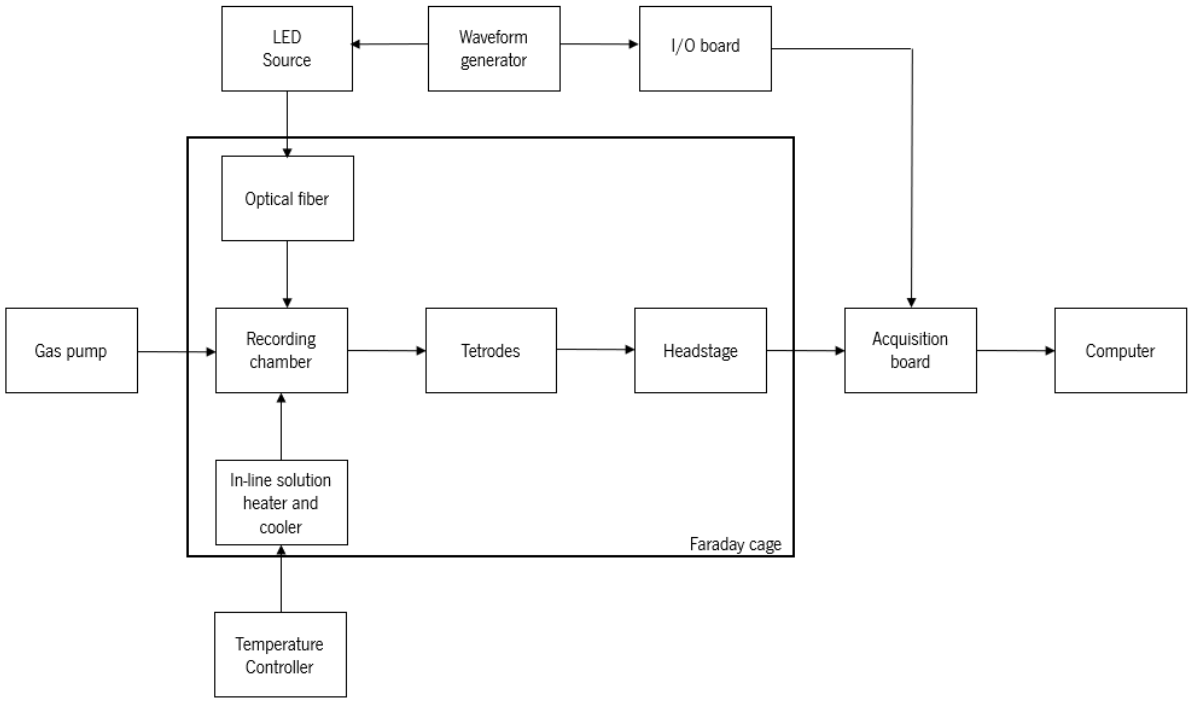


Figure 34 – Extracellular recordings with optogenetic stimulation's setup block diagram.

# Chapter 4

# Results

The overarching goal of this project is to the study low intensity focused ultrasounds as a tool for modulating neuronal brain activity. For achieving this long-term goal, first it was necessary to develop and implement a way to automatize the brain activity recording in brain slices, in a low-cost and re-usable, but nevertheless accurate and reproducible, manner. As such, the current master's dissertation accomplished the measuring of neuronal activity in mouse brain slices using a novel extracellular recording prototype based on tetrode electrodes, along with the analysis of single-unit activity through a newly developed semi-supervised spike sorting algorithm. Both the new prototype and spike sorting algorithm were validated using optogenetic stimulation, before proceeding to LIFUS neuromodulation protocols.

## 4.1. Electrophysiology Recordings

Extracellular recordings of spontaneous action potentials were performed in hippocampal, habenula and cerebellar brain slices with the described set up (subchapter 3.2.4) and shown in Figure 35. Continued neuronal activity was observed in the GUI, as depicted in Figure 36, and signal quality and spike detection was performed subjectively online by the user.

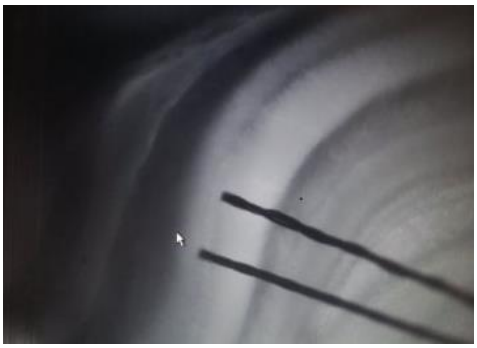

Figure 35 – Positioning of two tetrodes during the measurement of spontaneous activity in brain hippocampal slices (image obtained with the recording set up's microscope).

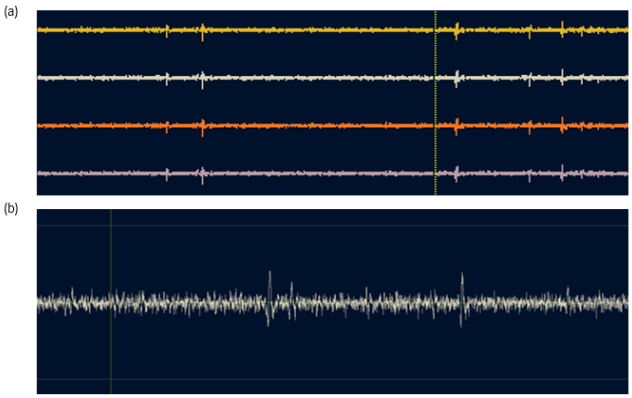


Figure 36 – Extracellular recordings of spontaneous action potentials, visualized online in the Open Ephys GUI. (a) – Hippocampal extracellular activity measured in one tetrode. (b) – Cerebellar extracellular activity in one recording channel.

## 4.2. Tetrodes

### 4.2.1. Electrode Wire

The appropriate electrode wire for performing extracellular recordings *ex vivo* was first selected before proceeding to tetrode manufacturing through the analysis of physical and electrical properties, such as the electrode wire diameter and impedance. Determining the suitable wire electrode resided on a compromise between the recording area and its impedance, bearing in mind that to isolate single units from extracellular recordings in the desired brain areas it should have an appropriate diameter, while presenting some degree of mechanical rigidity and an impedance range within 0.05 MΩ to 2 MΩ.

To achieve this goal, four distinct electrode wires were tested: (1) - 50 µm diameter nichrome wire (Science Products), (2) – 25 µm diameter platinum-iridium (90% Pt/10% Ir) wire (California Fine Wire), (3) – 12.5 µm diameter tungsten wire (California Fine Wire), (4) - 12.5 µm diameter nichrome (Redi Ohm 800, Hard PAC) wire (Sandvik, USA). The results of the four distinct wires' impedance measurements are presented below in Table 5. As it shows, the 50 µm diameter nichrome wire presented a mean impedance ($\bar{Z}$) of 1.55 MΩ, while the 25 µm diameter platinum-iridium (90% Pt/10% Ir) wire (which is characterized by a larger diameter) presented a higher $\bar{Z}$ of 2.22 MΩ. In resemblance to the 50 µm diameter nichrome wire, the 12.5 µm diameter tungsten wire and 12.5 µm diameter nichrome wire also presented mean impedance values below 2 MΩ.

The 50 µm diameter nichrome wire was excluded as a possible candidate due to its high diameter, considering that a tetrode (bundle of four coated nichrome electrodes) would have a width of 264 µm which would cause tissue damage at a large scale on brain slices (*ex vivo* mouse brain slices typically have 300 µm thickness). Likewise, the platinum-iridium wire was also rejected as a result of its large size and impedance values. Despite having a lower impedance than the 12.5 µm diameter nichrome wire, the 12.5 µm diameter tungsten wire was discarded as it presented a lower stiffness, being harder to manipulate with an increased risk of tip deformation and thus, complicating tetrode manufacturing. Based on these results the 12.5 µm diameter nichrome wire was selected as it presents a low diameter and an impedance value between the range of 1-2 MΩ.

Table 5 – Diameters and respective mean impedance ($\bar{Z}$) of distinct electrodes.

| **Electrode** | **Diameter (µm)** | $\bar{Z}$ **(MΩ)** |
|---|---|---|
| Nichrome | 50 | 1.55 |
| Platinum-Iridium (90% Pt/10% Ir) | 25 | 2.22 |
| Tungsten | 12.5 | 1.39 |
| Nichrome | 12.5 | 1.83 |

### 4.2.2. Gold Electroplating

In order to measure very small extracellular brain voltages, both background noise and neuronal background activity should be as low as possible. Background noise can be due to instrumentation noise but also electrochemical noise of the electrode/electrolyte interface. For metal-based electrodes, the electrochemical noise is related with its impedance. Hence, appropriate impedance values must be chosen to improve signal-to-noise ratio. Additionally, the impedance range should be such that it allows the recording of neurons in proximity to the electrodes while supressing or reducing voltage variations from distant neurons (i.e. background activity which can mask the activity of the proximal neurons).

Gold electroplating of several nichrome tetrodes' wires as to attain impedances between 70 and 100 kΩ was successfully accomplished. Before every recording session the electrodes were electroplated in that same day to guarantee plating quality and to prevent the accumulation of other particles in the

electrodes' tips. Table 6 presents exemplificative impedance values of freshly cut 12.5 um nichrome tetrodes before and after an electroplating session.

Table 6 – Impedance values before and after the electroplating of tetrodes (12.5 μm electrodes).

| EIB zone | Electrode wires | Initial impedance (MΩ) | Final impedance (MΩ) |
|---|---|---|---|
| 1 | 1 | 0,966 | 0,075 |
| 1 | 2 | 0,980 | 0,071 |
| 1 | 3 | 0,989 | 0,069 |
| 1 | 4 | 0,989 | 0,069 |
| 2 | 5 | 1,596 | 0,078 |
| 2 | 6 | 1,812 | 0,076 |
| 2 | 7 | 1,851 | 0,072 |
| 2 | 8 | 1,639 | 0,070 |

### 4.2.3. Prototype Design and Assembly

After the analysis of physical and electrical properties (electrode wire diameter and impedance) for selecting the appropriate electrode wire for extracellular brain recordings, I have proceeded to tetrode manufacturing using gold plated 12.5 um nichrome wire (see methods). These tetrodes were used on all prototypes designed and tested for extracellular recordings on brain slices and described below.

The first prototype (subchapter 3.3.2.3) that was used for preliminary recordings in brain slices (Figure 37) relied on materials and an EIB that already existed in the lab but presented some disadvantages, such as cumbersome and prolonged assembly, mechanical instability of the tetrode support structure, and limitations on re-use. The mechanical instability was mainly caused by the tetrodes' support structure which was composed of flexible polyimide support tubes, whereas the EIB's circular design and small size resulted in the occasional tetrodes' damage during processes such as the connection and detachment between EIB and NanoZ adaptor or recording headstage. Another issue was the need for gluing the 8 cm long polyimide tube into the EIB, causing damage during fixation and recovery

for re-use. This process resulted in the accumulation of cyanoacrylate glue in the EIB as well as the damage of its conductive tracks.

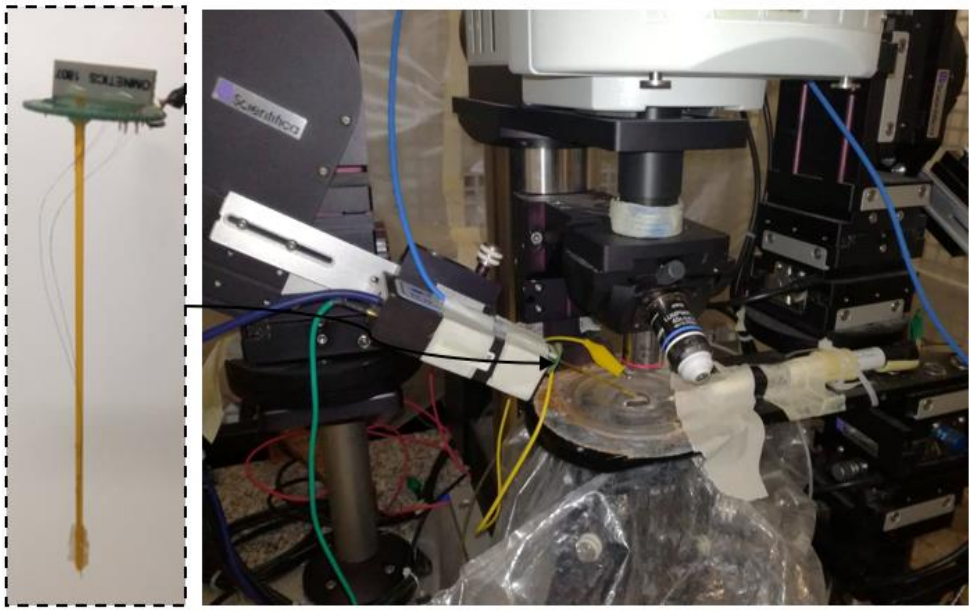

Figure 37 – Electrophysiology recordings setup using the first extracellular recording prototype for brain slices based on tetrodes.

To solve the issues from the first prototype, a couple of additional incremental prototypes were designed, assembled and tested but were ineffective in improving easiness of assembly and re-use (prototypes and data not showed). Thus, the whole concept was entirely re-engineered and a new tetrodes' support structure along with a new electrode interface board were separately designed in AutoCAD and Eagle software, respectively (see subchapter 3.3.3.2).

The final produced results are presented below in Figure 38. By designing two separate structures that are easily connected and detached by the simple use of two screws assembly time was drastically reduced. Moreover, since the support structure is easily 3D printed it can be quickly replaced whenever necessary and without any damage to the EIB (Figure 39).

Figure 41, shows the tetrode device loaded with tetrodes' wires and placed in the recording chamber filled with aCSF, where it presented a good performance in terms of mechanical stability and stiffness.

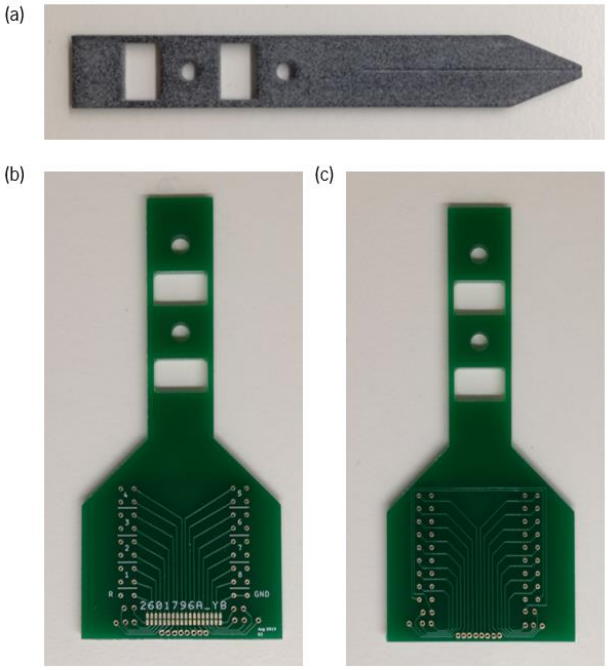


Figure 38 – Printed prototype parts. (a) - Tetrodes' support structure front view. (b) – Electrode interface board front view. (c) – Electrode interface board back view.

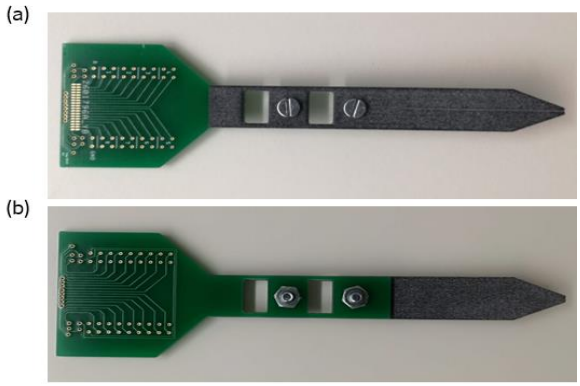


Figure 39 – Tetrode prototype (merge between tetrodes' structure and electrode interface board by means of screws). (a) – Front view, (b) – Back view.

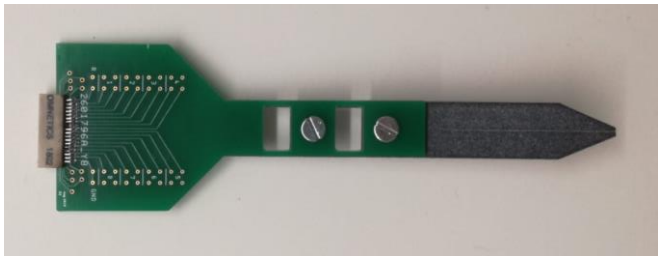

Figure 40 – Final tetrode prototype with the Omnetics connector.

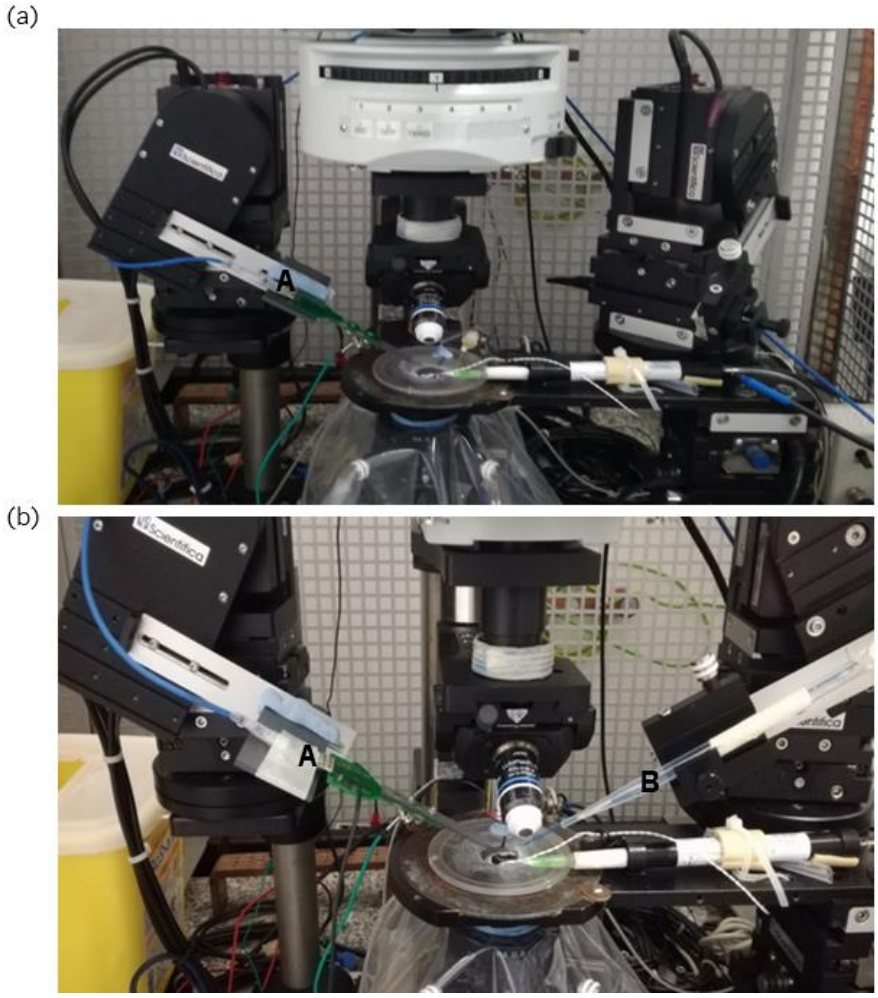


Figure 41 – Electrophysiology recordings setup while using the final extracellular recording prototype (a) and with optogenetic stimulation (b). A – tetrode device. B – Optical fiber.

## 4.3. Optogenetic Stimulation

Given that the goal of this project is to the study low intensity focused ultrasounds as a tool for modulating neuronal brain activity, it was important to validate whether this new prototype was able to detect subtle changes in neuronal brain activity after a known modulation.

Direct optical illumination of neurons expressing a light responsive channel called Channelrhodopsin-2 (ChR2) can elicit changes in neuronal spiking activity in brain slices (opto stimulation), which can then be detected by extracellular electrodes placed nearby (Figure 42). By applying light pulses at defined frequencies through an optical fiber, it was possible to observe entrainment of brain spiking activity. As such, neurons that were initially spiking at a given baseline frequency (Figure 43 a), quickly increased their frequency upon opto stimulation (based on qualitative assessment just by observing signals in the Open Ephys GUI) (Figure 43 b).

Immediately after opto stimulation, the signal's frequency decreased in all of the tetrode's channels, resulting in a lower number of spikes in comparison to the recorded activity before and during opto stimulation (Figure 43 c). This is due to a neuronal phenomenon known as "depolarization blockade", where neurons become unexcitable after sustained long periods of depolarization due to persistent inactivation of sodium channels. Eventually, the spiking partially recovered and stabilized near to its frequency of baseline activity. In some cases, individual neuronal responses were eradicated when applying excessive opto stimulation, leading to absence of spiking activity after opto stimulation, likely due to brain cells' death.

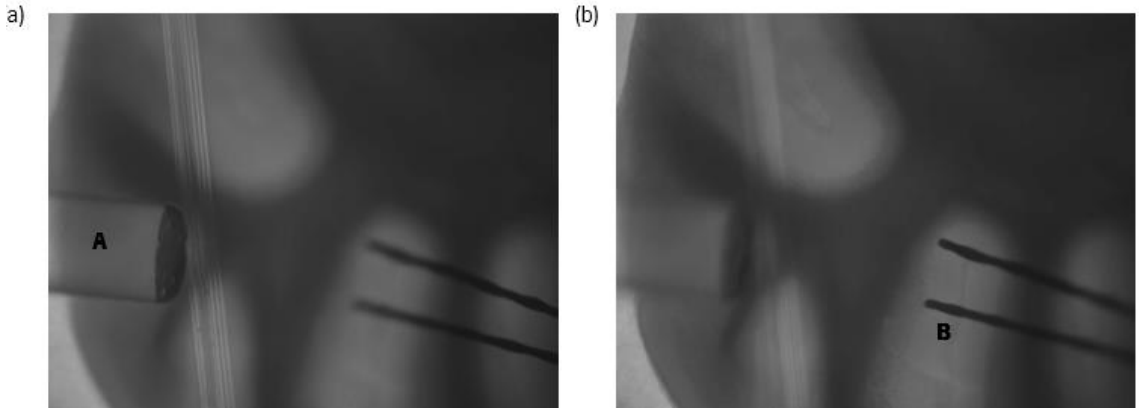


Figure 42 – Positioning of two tetrodes and the optical fiber during the measurement of extracellular activity with optogenetic stimulation in cerebellar slices (obtained with the recording set up's microscope). (a) – Picture focused in the optical fiber (A). (b) - Picture focused on the tetrodes (B).

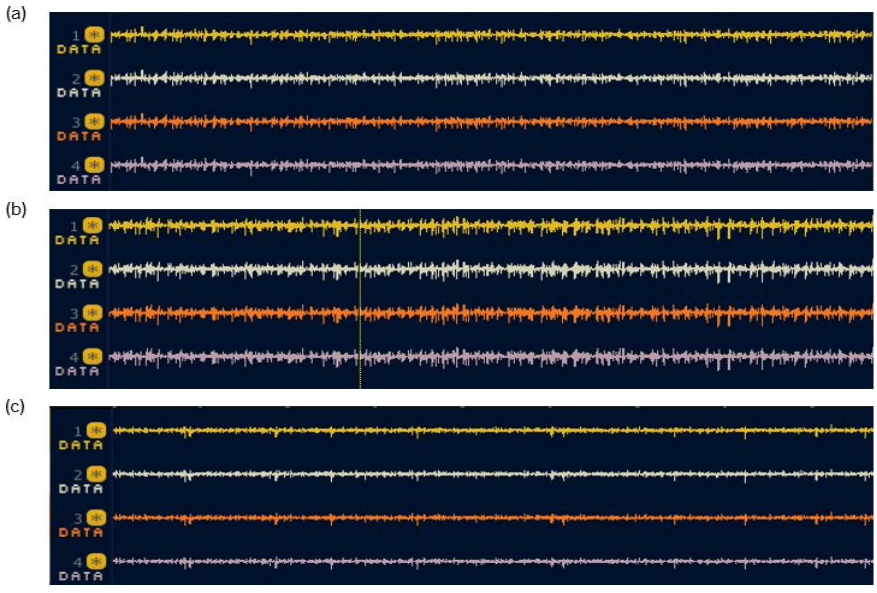


Figure 43 – Extracellular recordings of cerebellar slices with optogenetic stimulation, visualized online in the Open Ephys GUI. (a) – Extracellular activity before opto stimulation. (b) - Extracellular activity during opto stimulation. (c) - Extracellular activity immediately after opto stimulation.

## 4.4. Extracellular Neuronal Activity Processing and Analysis

### 4.4.1. Spike Detection

After qualitative visualization of brain spiking activity signals, quantitative measurements were performed in MATLAB. Spike detection was achieved by applying the algorithm published by Quiroga *et al.* (2004) [53]. As seen in Figure 44, the spike detection algorithm was capable of identifying the positive peaks of extracellular spikes in *ex vivo* brain slices. In certain recordings, it was necessary to increase the amplitude threshold to eliminate background activity or noise detection.

Furthermore, to prevent the detection of false spikes, the peak-to-peak distance was increase to 1.67ms, which is above the initial established 1 ms of neuronal refractory period.

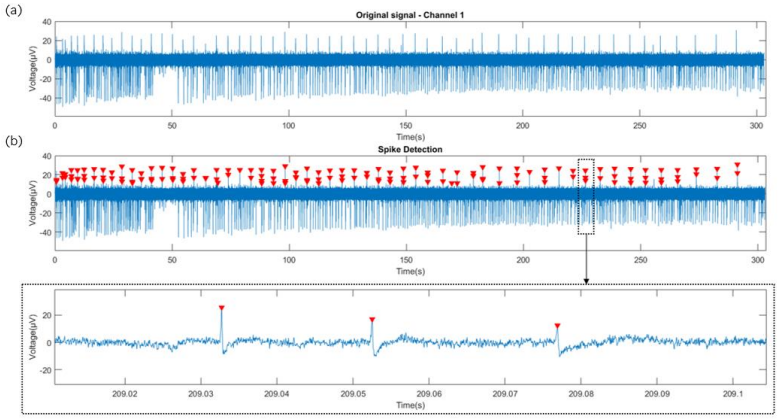


Figure 44 – Spike detection. (a) – Raw data of a single channel of the recording tetrode. (b) - Spike detection of spontaneous activity in hippocampal brain slices of a single channel of the recording tetrode (multiplier = 6 and peak-to-peak distance = 50 samples (approximately 1.67 ms)). Each red arrow indicates a detected spike.

### 4.4.2. Evoked Opto Activity

#### 4.4.2.1. Multi-Unit Activity

The first step for analyzing and processing evoked opto-activity was to look at MUA. The multi-unit activity of extracellular recordings with optogenetic stimulation in cerebellar slices is illustrated in Figure 45 and 46, with the time raster plot of its spiking activity for each stimulation trial (y-axis) along with the

Peristimulus Time Histograms (PSTHs) that display the mean firing rate (y-axis) of the neuronal population in all of the stimulation trials.

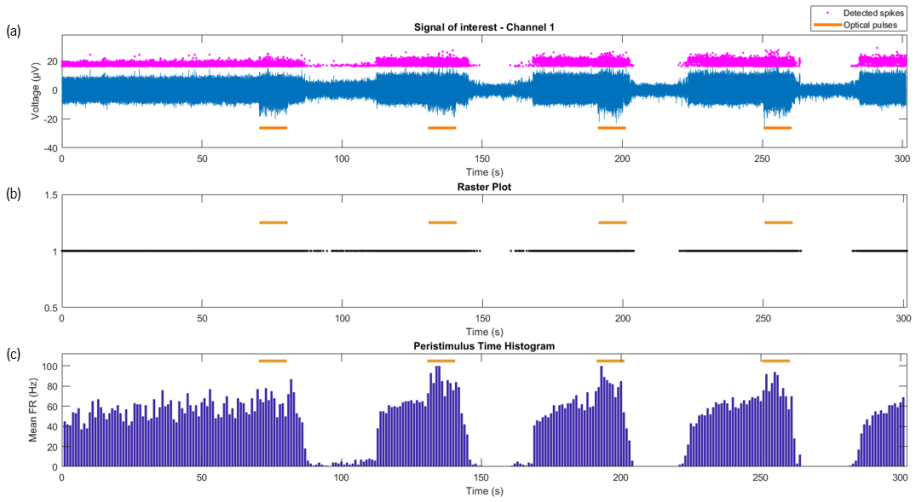


Figure 45 - Multi-unit activity with optogenetic stimulation (four trials of 10 s each) in cerebellar slices within a 300 s time window of a single tetrode channel. (a) – Raw signal with the detected spikes and optical pulses. (b) – Raster plot of the extracellular activity. (c) – Peristimulus Time Histogram (PSTH) of the extracellular activity. Spikes are indicated by pink arrows and opto-stimulation periods are indicated by an orange line.

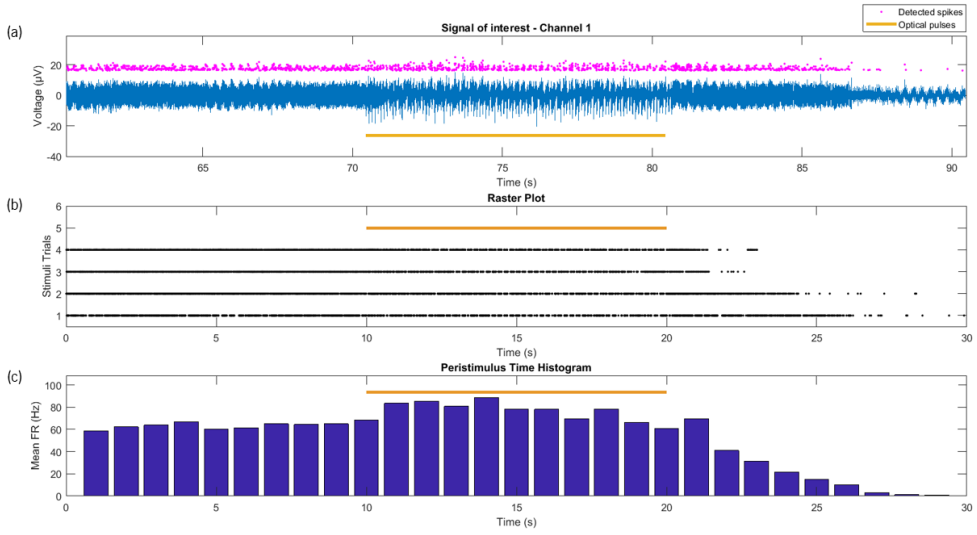


Figure 46 - Multi-unit activity with optogenetic stimulation in cerebellar slices within a 30 s time window of a single tetrode channel. (a) – Raw signal with the detected spikes and optical pulses. (b) – Raster plot of the extracellular activity in each optogenetic stimulation trial (with a duration of 10 s each). (c) – Peristimulus Time Histogram (PSTH) of the extracellular activity. Spikes are indicated by pink arrows and opto-stimulation periods are indicated by an orange line.

As shown in both figures, the mean firing rate increases upon each opto stimulation trial from a baseline spontaneous firing rate of approximately 40-60 Hz to an activity near 80 Hz. Nevertheless, the

signal's frequency decreased drastically (near 0 Hz) in the post-stimulus time period of approximately 30 s until it eventually recovers back to its baseline activity (approximately 40 to 60 Hz). In Figure 45 it can be seen that the brain slice's neurons become progressively unexcitable after each stimulation trial, resulting in longer periods of depolarization. By visual inspection it is possible to observe that our prototype was able to successfully detect subtle changes in spiking activity of cerebellar brain slices before and after optogenetic stimulation.

#### 4.4.2.2. Single-Unit Activity

When recording activity with a single wire, it is only possible to accurately detect multi-unit activity (MUA), which is a mixture of spikes from many neurons. However, when using tetrodes, it is possible to isolate spikes (called spike sorting) from individual neurons ("single units"). This sorted spiking activity is called single-unit activity (SUA) and provides an advantage in terms of knowing approximately how many neuron sources are present as well as analyzing the individual responses of single neurons. In order to find how many single units were present in the recorded datasets, a semi-supervised spike sorting algorithm was developed (see details in methods section). Then, to validate the new algorithm developed in this dissertation, an open-source toolbox called "WaveClus" was used to compare the results (results presented in the Appendices III and IV).

Furthermore, the new prototype's ability to detect subtle changes induced by a known modulator was validated through opto stimulation. As a result, by measuring the activity of individual neurons it is possible to examine how each individual neuron type responds to opto stimulation.

#### Semi-Supervised Spike Sorting

The identification of action potentials in cerebellar brain slices was first employed using the spike detection algorithm. The identified spikes' peak amplitudes were extracted and used as input parameters in the developed semi-supervised spike sorting algorithm.

After feature analysis, it is important to estimate how many clusters (single units) are present in the data. The k-means clustering is a popular method for cluster analysis in data mining. The method aims to partition observations into $k$ clusters in which each observation belongs to the cluster with the nearest mean, serving as a prototype of the cluster.

To achieve such purpose, k-means clustering was simultaneously performed for 2< $k$<5 to automatically find the optimal $k$ number of clusters. The clustering results were visualized in 2D projections by plotting the spike peak amplitudes of pairs of electrodes against each other, from one recording tetrode (which contains four recording electrodes and thus, four data channels). The interpretation of these results as well as the evaluation of the clustering performance was conducted through the average silhouette method. This method provides an estimate of how well the identified clusters are separated from each other, considering that an appropriate partition is the one with the maximum average silhouette over the tested number of clusters (Figure 47).

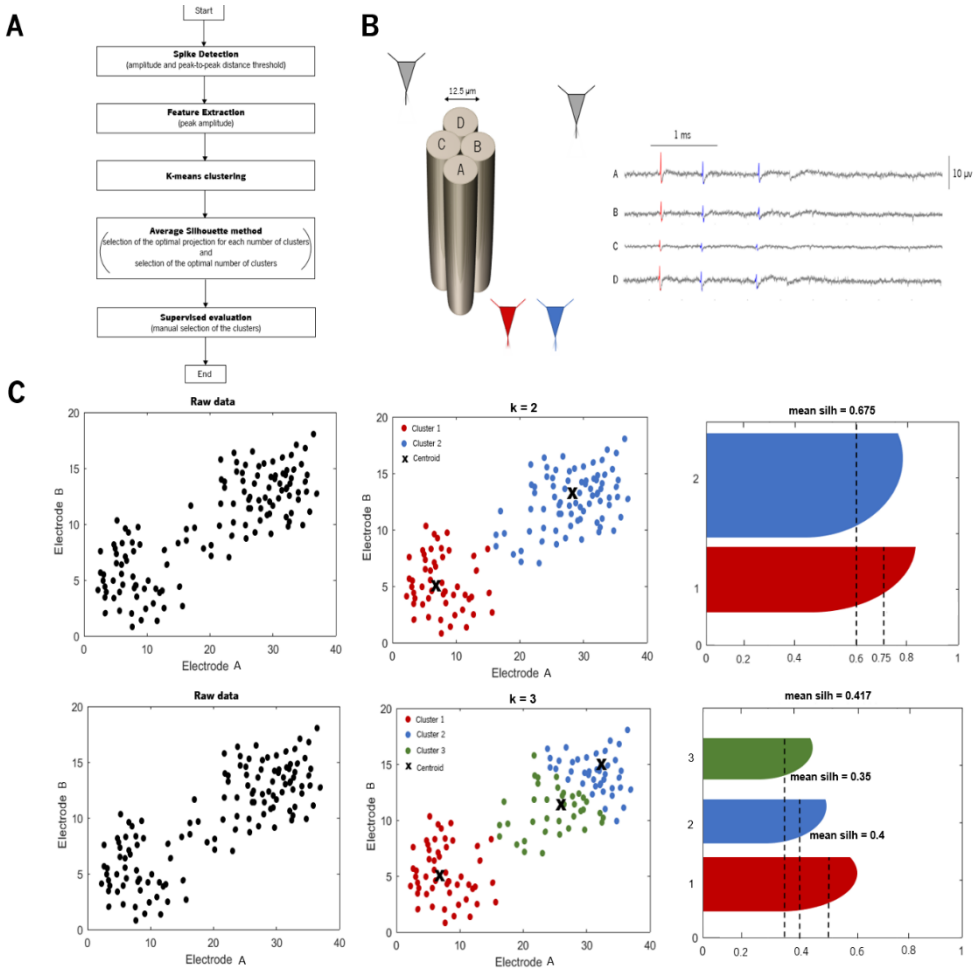


Figure 47 – Explanatory diagram of the developed semi-supervised spike sorting algorithm. (A) – semi-supervised spike sorting algorithm flowchart. (B) – four electrodes that constitute a tetrode and the activity of two nearby neurons as recorded by each electrode. (C) – example of K-means clustering for k = 2 (top panel) and k = 3 (bottom panel) of randomly generated data representing spikes' peak amplitudes as visualized by plotting a pair (2D projection) of electrodes A and B. Left panels represent 2D projections of raw data. Middle panels represent data after k-means clustering (each cluster represented by a different color). Right panels show the silhouette plots for each k-mean clustering results with the mean silhouette values of all clusters displayed on top of each plot. The clustering on the top panel (k=2) presents the highest mean silhouette value and would therefore be selected as the optimal number of clusters by the algorithm.

Figure 48 illustrates the partition results for the selected optimal number of clusters, $k$ = 3 (average silhouette value of approximately 0.53). The clustering results for the remaining tested number of clusters were placed in Appendix III. After selecting the optimal number of clusters, spikes' time in one of the tetrode's channels (Figure 49) as well as each individual clusters' spike waveforms and amplitudes (Figure 50) were examined. As showed in both figures, the spiking activity in cerebellum brain region was harder to partition in comparison to spike sorting of spontaneous activity in hippocampal brain slices (results present in Appendix III), since most waveforms are too similar to be correctly distinguished.

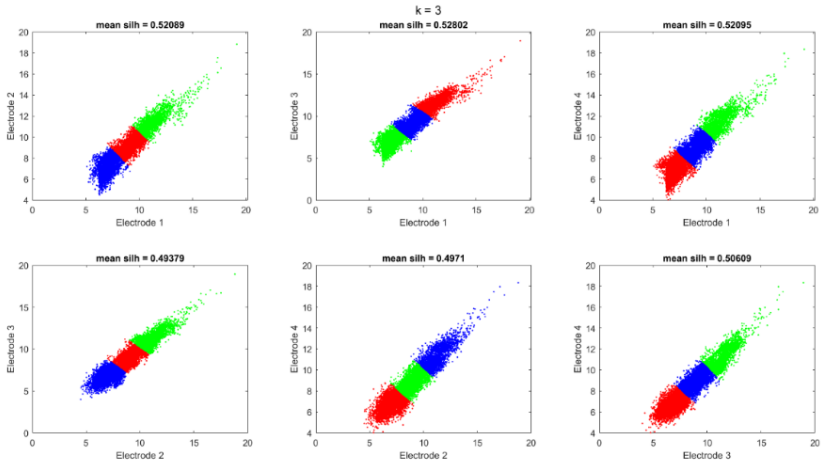


Figure 48 - K-means ($k$=3) clustering results along with the correspondent average silhouette values, visualized by plotting spike peak amplitudes recorded from pairs of electrodes of one tetrode against each other (2D projections).

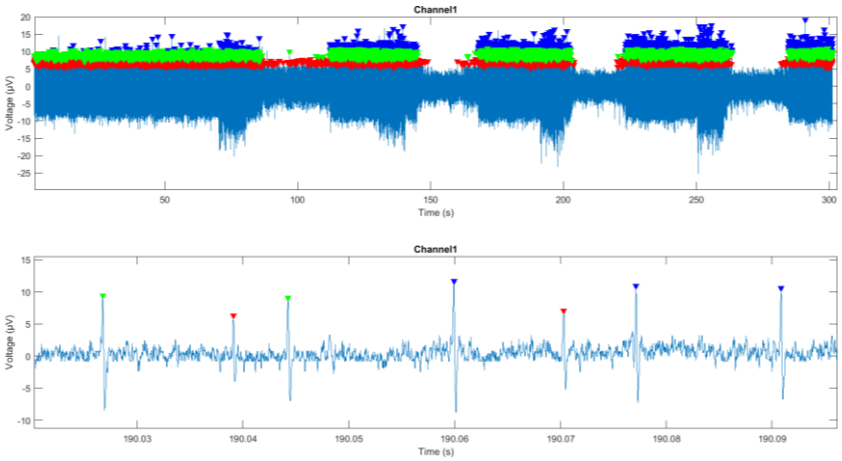


Figure 49 - Spikes' time for each separated cluster, obtained through semi-supervised spike sorting of extracellular activity before and after optogenetic stimulation (4 stimulation trials with a duration of 10 s each) in cerebellar brain slices. Each cluster is represented in a different color.

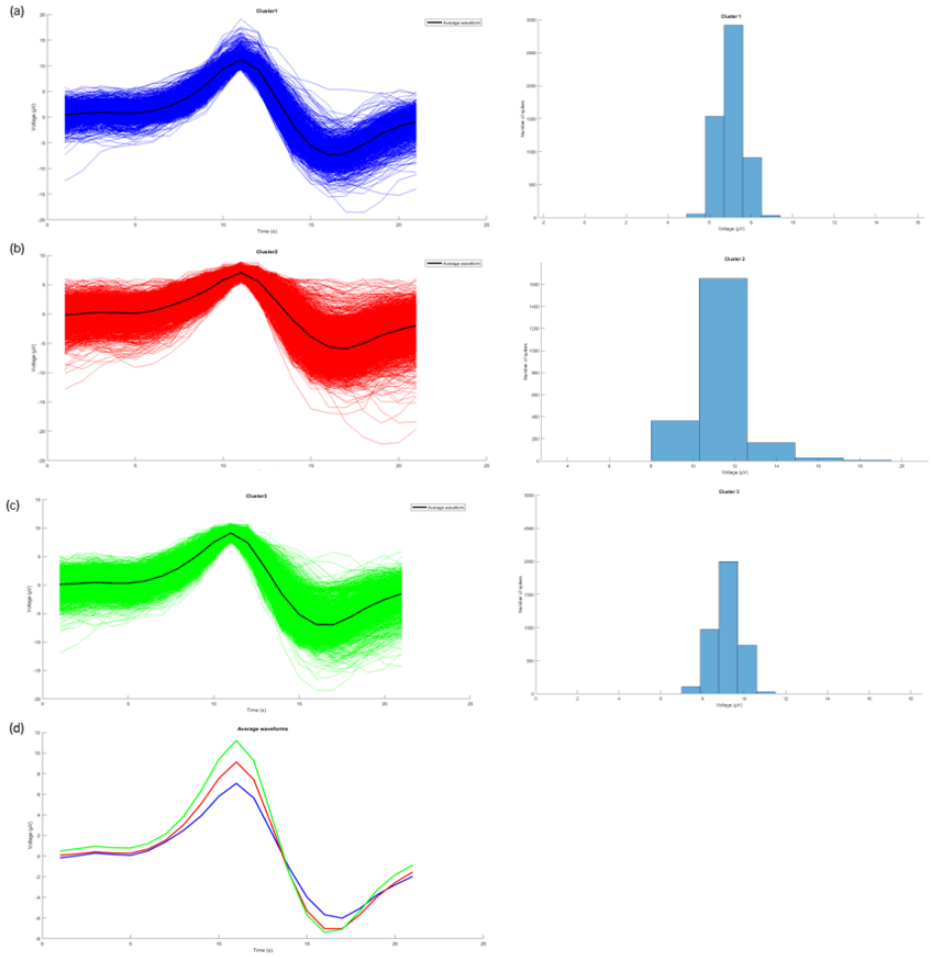


Figure 50 - Waveforms of all detected spikes of each separated cluster through semi-supervised spike sorting of evoked extracellular activity in cerebellar brain slices and correspondent amplitude histograms (the x- and y-axis were differentially adjusted for visualization purposes). (a) – Cluster 1. (b) – Cluster 2. (c) – Cluster 3. (d) – Average wave shape of all the separated clusters.

The single-unit activity of the classified clusters is shown in Figure 51 to Figure 53, with the corresponding raster plot of its spiking activity in each opto stimulation trial and Peristimulus Time Histogram. By comparing the results of all three figures, the single unit assigned to cluster 2 was the neuron with the highest response to opto stimulation, changing from a baseline activity with a mean firing rate of approximately 20 Hz to an activity approximately above 30 Hz. The remaining units (cluster 1 and cluster 3) were characterized by mean firing rates of approximately 10-20 Hz and 20-30 Hz, respectively. However, these clusters seemed to have very little to no response during delivery of opto light pulses, displaying fewer noticeable increases in the mean firing rate in comparison to the cluster 2 single unit.

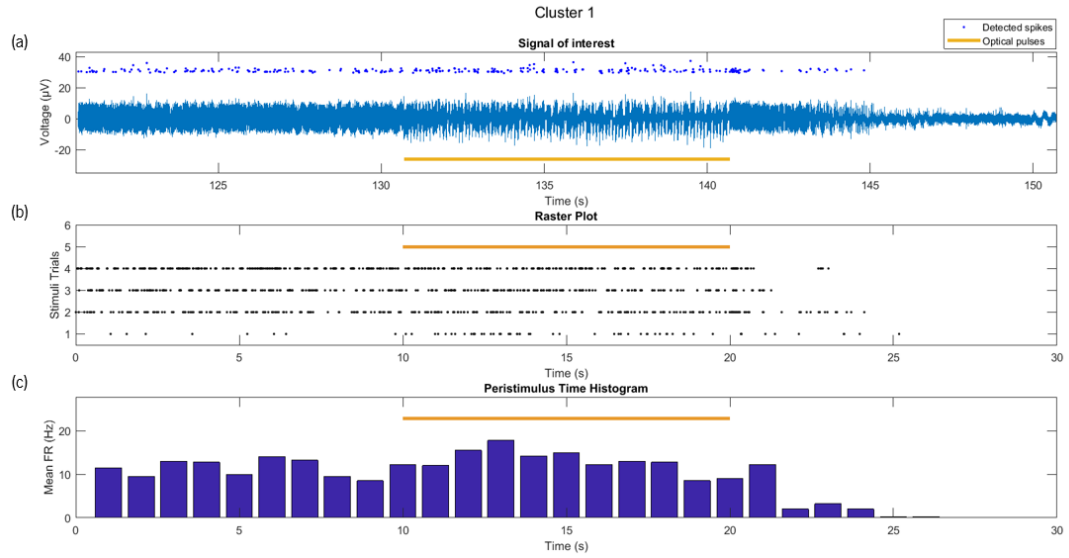


Figure 51 - Single-unit activity of the neuron corresponding to cluster 1, obtained through semi-supervised spike sorting of extracellular activity with optogenetic stimulation (4 stimulation trials with a duration of 10 s each) in cerebellar brain slices. (a) – Raw signal with the detected spikes. (b) – Raster plot of the neuron's activity during each trial. (c) – Peristimulus Time Histogram (PSTH) of the neuron's activity. Orange line represents opto stimulation period.

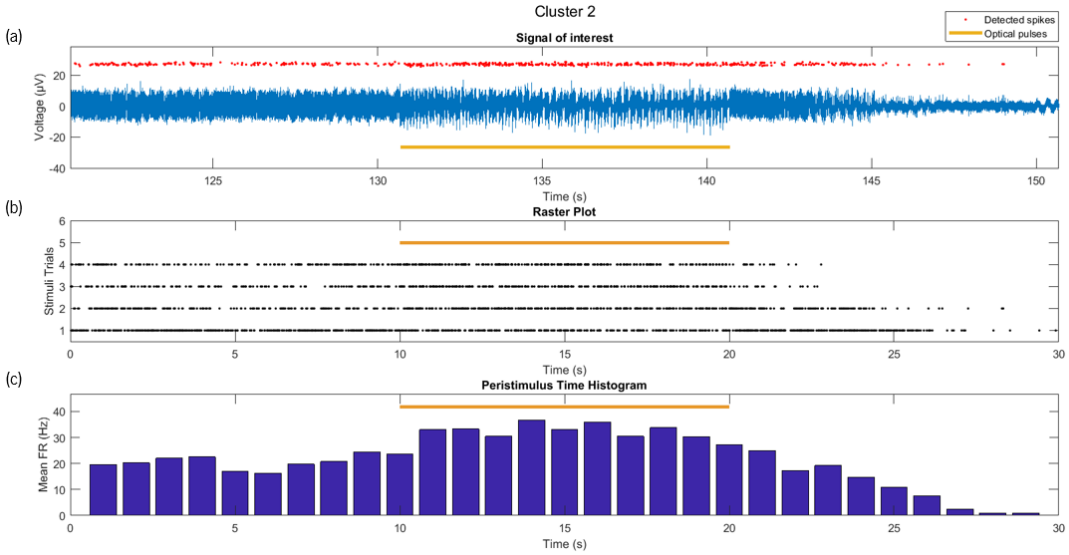


Figure 52 - Single-unit activity of the neuron corresponding to cluster 2, obtained through semi-supervised spike sorting of extracellular activity with optogenetic stimulation (4 stimulation trials with a duration of 10 s each) in brain cerebellar brain slices. (a) – Raw signal with the detected spikes. (b) – Raster plot of the neuron's activity during each trial. (c) – Peristimulus Time Histogram (PSTH) of the neuron's activity. Orange line represents opto stimulation period.

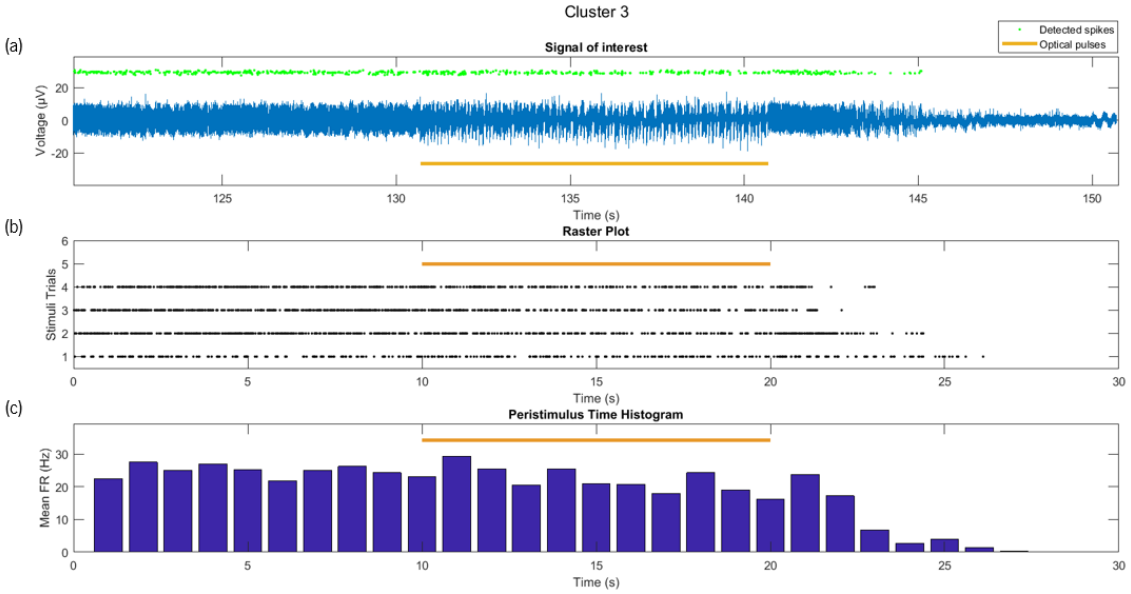


Figure 53 - Single-unit activity of the neuron corresponding to cluster 3, obtained through semi-supervised spike sorting of extracellular activity with optogenetic stimulation (4 stimulation trials with a duration of 10 s each) in cerebellar brain slices. (a) – Raw signal with the detected spikes. (b) – Raster plot of the neuron's activity during each trial. (c) – Peristimulus Time Histogram (PSTH) of the neuron's activity. Orange line represents opto stimulation period.

# Chapter 5

# Discussion

This dissertation explored the feasibility of inducing neuromodulation by targeting neuronal structures with low intensity focused ultrasound (LIFUS). To achieve such a purpose, a review of UNMOD studies over the past few decades was first performed, displaying the ability of US to modulate neuronal activity in both the central and peripheral nervous system. A myriad of methodologies and subsequent outcomes - summarized in Table 1, 2 and 3 (subchapter 2.2) - corroborate that US can elicit neuronal responses in several experimental models such as cell cultures, *ex vivo* brain slices, small or large animals and more recently, humans. In fact, a significant number of human studies have reported that tFUS can be employed as an efficient and well-tolerated neuromodulation technique under the standard safety guidelines, capable of targeting the primary motor and visual cortices along with deeper structures such as the thalamus.

Transcranial FUS has emerged as a pioneering technique characterized by a non-invasive, reversible, safe and cost-effective neuromodulation, capable of penetrating the skull barrier and modifying the neuronal activity of deep brain structures with a high spatial resolution. Hence, tFUS holds great potential for replacing conventional neuromodulation techniques such as DBS, TMS and tDCS in the treatment of neurological or psychiatric disorders; working as well as a basic research tool for investigating brain function. Nevertheless, this potential is hindered by the lack of mechanistic understanding regarding the FUS-induced neuronal responses, despite several explanatory models having been proposed (subchapter 2.2.4). UNMOD is also constrained by a large number of protocols with distinct stimulation parameters, leading to standardization and repeatability deficiency.

A preliminary selection of the adequate acoustic parameters (carrier frequency, transmission mode, pulse repetition frequency, duty cycle, sonication duration and intensity) can optimize FUS delivery and the modulation of specific brain regions, enabling an efficient energy transmission where the maximal acoustic power occurs at the focal point of the ultrasound beam and, therefore limiting defocusing and increasing spatial and temporal resolution. Likewise, thermal ablation and damage of neuronal tissue can

be avoided by the theoretical account of thermal dose and heat deposition in the sonicated regions, decreasing the risk of inducing irreversible biohazards in the brain tissue.

Regarding the selection of the carrier frequency, lower frequencies have wider acoustic focus which can lead to the sonication of surrounding areas to the target tissue. In turn, higher frequencies have a lower depth of penetration along with a higher temperature rise and tissue heating, considering that the acoustic waves are attenuated with the propagation distance due to the absorption of acoustic energy and scattering processes. King *et al.* reported that lower carrier frequencies were also capable of achieving higher stimulation efficacy for a certain acoustic intensity [56]. Moreover, Tufail and colleagues [18] recommended the use of a center frequency between 0.2 and 0.7 MHz, while considering that the optimal acoustic frequencies for eliciting brain activity in intact mice brains lied between 0.25 and 0.65 MHz. Hence, in the present study, a low frequency (< 1 MHz) focused ultrasound transducer with a fundamental frequency of 0.65 MHz was chosen to deliver acoustic waves to modulate the activity of neuronal circuits in *ex vivo* brain slices.

As stated by King *et al.* [56], although both continuous-wave (CW) and pulsed-wave (PW) transmission modes were capable of eliciting brain activity (in paralleled conditions of $I_{SPTA}$), CW stimulation was correlated to higher neurostimulation success rates and robust elicited motor responses. A contradictory dependence was reported by Kim *et al.* [49], where a pulsed sonication scheme required lower intensities in order to elicit neuronal activity in relation to continuous stimulation, resulting in a higher neurostimulation efficiency. Moreover, bearing in mind that a duty cycle tending to unity is conducive to a continuous sonication scheme, the smaller the duty cycle value (lower $I_{SPTA}$ in respect to $I_{SPPA}$), the less heat can be deposited in the target tissue. Thus, the current study opted por the transmission of pulsed FUS with a low duty cycle to avoid hazards such as tissue overheating and neural function decrease or cell's death, namely with values equal or below 50% as previously employed by other US neuromodulation studies [56, 69].

Moreover, Yoo *et al.* [38] stipulated that the acoustic intensity was linked to the transition of the neuromodulation mode (inhibition or activation of neuronal structures), where neuronal excitation was correlated to increased acoustic intensity whilst sonications characterized by lower intensities and shorter durations have suppressing effects. On the other hand, Tsui *et al.* [67] supported an opposite relation, where higher stimulation durations and acoustic intensities were associated to neuronal activity inhibition. This incoherence between stimulation protocols and subsequent results reinforces the complexity in choosing the right FUS parameters to achieve the desired outcomes (neuronal inhibition or activation).

Ergo, an experimental protocol was developed in the current study, describing how to apply low intensity FUS using pulsed *stimuli* along with a sonication duration in the range of 20-500 ms [56, 69], pulse duration within 0.0227-0.5 ms [43, 68] and a PRF of 0.1-2 kHz [43, 69]. This protocol should enable a general study of the FUS-induced neuronal responses through electrophysiology recordings.

Furthermore, a novel neuromodulation technique has been introduced to the Life and Health Science Institute (ICVS) through the selection and installation of an ultrasound system, characterized by a focused ultrasound transducer with a fundamental frequency of 0.65 MHz. The US system was mounted and assembled next to a pre-existent electrophysiology recording setup, with the objective of targeting *ex vivo* brain slices with LIFUS, along with the simultaneous recording of the brain slices' extracellular activity and its response upon the delivery of acoustic energy. Concerning the *ex vivo* brain slice model, artifacts may arise due to the existence of acoustically reflective surfaces such as air interfaces and the plastic slice recording chamber; while the extracellular recording process may result in electrode mechanical artifacts. In order to diminish electrode-induced artifacts, the US neuromodulation and recording sites can be defined in distinct positions and thus, by stimulating neuronal projections with US it is possible to measure the electrical activity of distant neurons that synapse with the projecting neurons. Furthermore, the US system can also be employed for future *in vivo* neuromodulation studies, using rat or mice models, bearing in mind that animal installation (animal bed and frame) and a 3D positioning system to control the positioning of the transducer (for which the US system's main cabinet already presents the corresponding ports for connecting both systems) can be purchased with the US system manufacturer (Image Guided Therapy, France).

The current dissertation also presents recordings of neuronal activity in mouse brain slices using a novel extracellular recording prototype based on tetrode electrodes, along with the analysis of single-unit activity through a newly developed semi-supervised spike sorting algorithm.

Hardware developments included the design and production of a reusable and reproducible device, which not only reduced costs and assembly time but also increased re-use success. Although tetrodes usually provide reasonable mechanical stability of recordings when chronically implanted in the brain, this is not the case when used in *ex vivo* brain slices like in this project. One of the advantages of this new prototype was its mechanical rigidity and stiffness, conferring stability during brain slice recordings (preventing tetrode's fluctuations inside the recording chamber liquid perfusion) and while steering the tetrodes for positioning into the targeted brain tissue. The use of tetrodes proved to be a lower-cost method compared to other approaches such as silicon probes and microelectrode arrays (MEAs), as well as a

reliable technique for measuring the activity of multiple neurons in brain slices, with a high spatial resolution for inferring putative single units' sources in contrast to single-wire extracellular electrodes. Moreover, tetrodes do not have a fixed geometry in terms of electrode spacing, providing greater spatial flexibility when compared to MEAs. One important step to mention when manufacturing the tetrodes is the initial tetrode's cut because it influenced not only the electroplating process performance but also the quality of the electrophysiology recordings, since it would easily result in insulation damage and in short circuits.

In terms of electrode impedance, gold-electroplating was a simple process that yielded good results in terms of lowering electrode impedances and improving signal-to-noise ratio. However, depending on the brain region to be tested, this is not always an advantage. Lower impedance values were not ideal when recording for example from cerebellum brain region, which is characterized by high density of very large neurons such as Purkinje cells (one of the largest neurons in the brain). Therefore, the low impedance tetrodes recorded a great number of simultaneous signals that complicated subsequent signal processing and data analysis. One solution would have been to use higher impedance electrodes to decrease the number of far-away background neurons and thus enhancing spike detection and sorting.

Additionally to the recording prototype, a new data analysis tool was developed in the current master's dissertation, composed of spike detection and semi-supervised spike sorting algorithms. With this approach, the spike detection was performed with an amplitude threshold, automatically set as a multiple of the standard deviation of the background noise. Assuming that spikes amount to a minor fraction of all samples, this method diminished the interference of spikes by using the median in threshold estimation [104]. Therefore, the implemented algorithm produced an effective separation of the spiking activity of nearby neurons (to the recording site) from the background noise and activity of distant neurons. Nevertheless, although four times the standard deviation of the background noise was established by Quiroga *et al.* (2004) [104], it was necessary to manually modify the detection threshold according to the SNR of the studied data, knowing that a higher threshold may increase the number of missed spikes while lowering the threshold could rise the number of false positives.

The semi-supervised spike sorting was performed with K-means clustering, which grouped the peak amplitudes of each detected spikes according to the minimum Euclidian distance between each sample to the cluster centroids. Nonetheless, by using the minimum Euclidian distance as a classification criteria, the distribution of the samples within a cluster is ignored and consequently, this clustering algorithm fails to recognize clusters with shapes that deviate from a spherical distribution [105]. This problem was

observed in the analysis of the evoked activity in cerebellar brain slices, in which all samples were concentrated in the same clustering space, resulting in clusters with an ellipsoidal shape. The same was not verified in the analysis of spontaneous activity in hippocampal brain slices (see results in Appendix IV). Moreover, this method also assumes that all samples belong to a cluster by which the removal of outliers must be manually performed. This drawback was verified in the clustering results of both spontaneous and evoked activity of hippocampal and cerebellar brain slices, respectively.

Nevertheless, K-means clustering was used due to its easy implementation and efficient computation. This method was semi-supervised considering that the algorithm tested the best parameters to define the clusters and then clustering results were checked by a human user and corrected if needed. This approach can achieve lower errors and misclassifications in comparison to manual sorting and clustering; yet it may still result in the introduction of subjectivity and bias over the spike sorting pipeline. Other clustering techniques can be employed as to solve these issues, such as template matching that uses models spike shapes to classify new waveforms, while using a distance metric [106].

Furthermore, the clustering results were also submitted to validation methods such as the average silhouette method and compared to other techniques such as the ones employed by the "Wave Clus" open-source toolbox. The average silhouette method assessed the quality of the clustering, enabling the verification of the optimal number of clusters by the human-operator. In turn, "Wave Clus" results validated the semi-supervised spike sorting during the study of both spontaneous activity in hippocampal brain slices, in particular by obtaining clusters with similar waveforms as well as identical firing rates from the activity of isolated single units (see Appendix IV).

This analysis did not deal with sources of spike sorting errors, such as overlapping spikes or bursting neurons. The overlap of spike waveforms results from the synchronous firing (or with a small delay) of two or more nearby neurons, which then gives rise to spikes of multiple amplitudes and shapes. Misclustering can be avoided if one of the units displays a much higher peak amplitude or if the delay between the spiking activity is long enough to recognize the existence of two peaks in the cluster's waveform. The existence of overlapping spikes was found in the "Wave Clus" toolbox clustering results of evoked activity in cerebellum brain slices (see Appendix III), by which the clusters with more than one peak were discarded as single units. This issue was not verified in the clustering results of the semi-supervised spike sorting algorithms.

Regarding the use of optogenetics stimulation, our new prototype proved to be an efficient method for recording evoked activity by opto stimulation during extracellular recordings (qualitatively assed by

observing signals in the Open Ephys GUI) and later, during the analysis of both multi-unit and single-unit activity (subchapter 4.4). The study of MUA showed the activation of a small neuronal population by delivering light stimulus, followed by a refractory period of very low to inexistent spiking activity until its recovery to baseline; whereas SUA analysis allowed the recognition of individual neurons which responded differently to the presentation of light pulses. Consequently, after using opto stimulation as a positive control, tetrodes can later be coupled with ultrasound stimulation as to record and study the neuromodulatory effects of low-intensity US.

The prototype and pipeline analysis developed and validated in this dissertation have laid the foundations to now test low intensity focused ultrasounds as a tool for modulating neuronal brain activity. In addition, the developed prototype can be used for other purposes involving brain activity recordings, providing a simple and cheap alternative to other more expensive approaches.

# Chapter 6

# Conclusions and Future Work

The overall goal of this master's dissertation was to select and perform preliminary tests upon an ultrasound system as a modulatory tool of neuronal brain activity. This goal was achieved by implementing a new ultrasound setup, adapted to the pre-existing electrophysiology recording setup, which can later be used for other future studies. Furthermore, an ultrasound neuromodulation protocol was elaborated based on the reviewed UNMOD literature, considering that future work will be done to determine the optimal sonication parameters to provide successful and effective neuromodulation through low intensity FUS. In order to test the new ultrasound setup many other steps had to be implemented beforehand, such as a way to accurately record and analyze neuronal activity from different brain regions, namely through the development of a novel extracellular recording prototype for brain slices based on tetrodes as well as a semi-supervised spike sorting algorithm.

Despite the recent publications demonstrating the feasibility of using ultrasound neuromodulation, the scientific community has not yet reached an agreement regarding the optimal US stimulation parameters and its underlying mechanisms remain to be explained. Such discoveries could enable safer and further controllable *in vivo* protocols for research studies and, possibly contribute to the future treatment of neurological diseases and dysfunctions. Ergo, the following points should be addressed next:

- FUS's capability to directly excite or inhibit synaptic transmissions, along with its influence in membrane conductance through electrical evidence;
- Interactions between ultrasound and nerve tissue, namely the mechanism responsible for eliciting or suppressing electrical neuronal activity.
- Ideal ultrasound transducer parameters such as the administered thermal exposure and dosage, which allow safe neuromodulation without the risk of ablating or damaging brain tissue.
- The optimal ultrasound intensity or pressure threshold that empowers a favorable targeting and stimulation of neural regions, by varying the acoustic parameters (frequency, pulse repetition

frequency, among others). To test and analyze the influence of US parameters in the neuromodulation process;

This work gives a step forward by providing means to experimentally test and answer many of these questions. Furthermore our prototype can be used for other studies providing a cheap and high throughput alternative to silicon probes and MEAs when recording neuronal activity in *ex vivo* brain slices.

In summary, the work developed along this master's dissertation resulted in:

- Selection and installation of an ultrasound system based upon literature review.
- Development of an experimental protocol for ultrasound neuromodulation of *ex vivo* brain slices.
- Development and implementation of a new low-cost and re-usable prototype to record extracellular activity in *ex-vivo* slices;
- Development of a new spike sorting algorithm that allows the analysis of single-unit activity (SUA) of neuronal ensembles in brain slices;
- Validation of the used recording method to successfully measure the modulatory effects on neuronal activity upon presentation of an external stimulus, by means of extracellular electrophysiology recordings and optogenetic stimulation;

# References


[1] L. B. D. Squire, F. E. Bloom, S. du Lac, A. Ghosh and N. C. Spitzer, Fundamental Neuroscience, London: Academic Press, 2008.

[2] C. Hammond, Cellular and Molecular Neurophysiology, Academic Press, 2015.

[3] D. Purves, G. J. Augustine, D. Fitzpatrick, L. C. Katz, A. S. LaMantia, J. O. McNamara and S. M. Williams, Neuroscience, Sunderland (MA): Sinauer Associates, 2004.

[4] E. R. Kandel, J. H. Schwartz, T. M. Jessell, S. A. Siegelbaum, A. J. Hudspeth and S. Mack, Principles of Neural Science, New York: The McGraw-Hill Companies, 2013.

[5] G. B. Ermentrout and D. H. Terman, Mathematical Foundations of Neuroscience, New York: Springer-Verlag , 2010.

[6] M. Carter and J. Shieh, Guide to Research Techniques in Neuroscience, London: Academic Press, 2015.

[7] M. Mattia, S. Ferraina and P. Del Giudice, "Dissociated multi-unit activity and local field potentials: a theory inspired analysis of a motor decision task.," *Neuroimage,* vol. 52, no. 3, pp. 812-23, 2010.

[8] G. Hong and C. M. Lieber, "Novel electrode technologies for neural recordings," *Nature Reviews Neuroscience,* vol. 20, p. 330–345, 2019.

[9] C. K. Alexander and M. N. O. Sadiku, Fundamentals of Electric Circuits, McGraw-Hill, 2006.

[10] G. E. Loeb, R. A. Peck and J. Martyniuk, "Toward the ultimate metal electrode," *Journal of Neuroscience Methods,* vol. 63, pp. 175-183, 1995.

[11] K. D. Harris, R. Q. Quiroga, J. Freeman and S. L. Smith, "Improving data quality in neuronal population recordings," *Nature Reviews, Neuroscience,* vol. 19, no. 9, p. 1165–1174, 2016.

[12] X. L. Chen, Y. Y. Xiong, G. L. Xu and X. F. Liu, "Deep brain stimulation," *Interventional Neurology,* vol. 1, no. 3-4, p. 200–212, 2013.

[13] US Food and Drug Administration, "FDA News Release: FDA Approves Humanitarian Device Exemption for Deep Brain Stimulator for Severe Obsessive-Compulsive Disorder," 2009.

[14] US Food and Drug Administration, "PMA: Medtronic DBS System for Epilepsy," 2018.

[15] K. E. Lyons, W. C. Koller, S. B. Wilkinson and R. Pahwa, "Long term safety and efficacy of unilateral deep brain stimulation of the thalamus for parkinsonian tremor," *Journal of Neurology, Neurosurgery, and Psychiatry,* vol. 71, no. 5, pp. 682-684, 2001.

[16] A. R. Rezai, M. Phillips, K. B. Baker, A. D. Sharan, J. Nyenhuis, J. Tkach, J. Henderson and F. G. Shellock, "Neurostimulation system used for deep brain stimulation (DBS): MR safety issues and implications of failing to follow safety recommendations," vol. 39, no. 5, pp. 300-303, 2004.

[17] F. G. Shellock, "Metallic neurosurgical implants: evaluation of magnetic field interactions, heating, and artifacts at 1.5-Tesla," *Journal of Magnetic Resonance Imaging,* vol. 14, no. 3, pp. 295-299, 2001.

[18] Y. Tufail, A. Yoshihiro, S. Pati, M. M. Li and W. J. Tyler, "Ultrasonic neuromodulation by brain stimulation with transcranial ultrasound.," *Nature Protocols,* vol. 6, no. 9, pp. 1453-70, 2011.

[19] J. P. O'Reardon, P. Cristancho and A. D. Peshek, "Vagus Nerve Stimulation (VNS) and Treatment of Depression: To the Brainstem and Beyond," *Psychiatry ,* vol. 3, no. 5, p. 54–63, 2006.

[20] J. A. Clancy, M. D. A. K. K. Witte, J. P. Greenwood, S. A. Deuchars and D. J. , "Non-invasive vagus nerve stimulation in healthy humans reduces sympathetic nerve activity," *Brain Stimulation,* vol. 7, no. 6, pp. 871-877, 2014.

[21] J. C. Horvath, J. Mathews, M. A. Demitrack and A. Pascual-Leone, "The NeuroStar TMS device: conducting the FDA approved protocol for treatment of depression," *Journal of Visualized Experiments,* no. 45, 2010 .

[22] M. A. Nitsche and W. Paulus, "Noninvasive brain stimulation protocols in the treatment of epilepsy: Current state and perspectives," *Neurotherapeutics,* vol. 6, no. 2, p. 244–250, 2009.

[23] L. Cocchi, A. Zalesky, Z. Nott, G. Whybird, P. B. Fitzgerald and M. Breakspear, "Transcranial magnetic stimulation in obsessive-compulsive disorder: A focus on network mechanisms and state dependence," *NeuroImage: Clinical - Journal,* vol. 19, p. 661–674, 2018.

[24] M. Kobayashi and A. Pascual-Leone, "Transcranial magnetic stimulation in neurology," *The Lancet Neurology,* vol. 2, no. 3, pp. 145-156, 2003.

[25] Y. Tufail, M. A. N. Baldwin, M. L. Tauchmann, J. Georges, A. Yoshihiro, S. I. Tillery and W. J. Tyler, "Transcranial pulsed ultrasound stimulates intact brain circuits," *Neuron,* vol. 66, no. 5, pp. 681-694, 2010.

[26] M. A. Nitsche, L. G. Cohen, E. M. Wassermann, A. Priori, N. Lang, A. Antal, W. Paulus, F. Hummel, P. S. Boggio, F. Fregni and A. Pascual-Leone, "Transcranial direct current stimulation: State," *Brain Stimulation,* vol. 1, no. 3, pp. 206-23, 2008.

[27] M. S. George and G. Aston-Jones, "Noninvasive techniques for probing neurocircuitry and treating illness: vagus nerve stimulation (VNS), transcranial magnetic stimulation (TMS) and transcranial direct current stimulation (tDCS)," *Neuropsychopharmacology,* vol. 35, no. 1, pp. 301-316, 2010.

[28] L. I. Navarro de Lara, C. Windischberger, A. Kuehne, M. Woletz, J. Sieg, B. S. N. Weiskopf, B. Strasser, M. E. and E. Laistler, "A novel coil array for combined TMS/fMRI experiments at 3 T," *Magnetic Resonance in Medicine,* vol. 74, no. 5, pp. 1492-501, 2015.

[29] K. M. Tye and K. Deisseroth, "Optogenetic investigation of neural circuits underlying brain disease in animal models," *Nature Reviews Neuroscience,* vol. 13, no. 4, pp. 251-266, 2012.

[30] A. M. Shah, S. Ishizaka, M. Y. Cheng, E. H. Wang, A. R. Bautista, S. Levy, D. Smerin, G. Sun and G. K. Steinberg, "Optogenetic neuronal stimulation of the lateral cerebellar nucleus promotes persistent functional recovery after stroke," *Scientific Reports,* vol. 7, no. 46612, 2010.

[31] L. Fenno, O. Yizhar and K. Deisseroth, "The development and application of optogenetics," *Annual Review of Neuroscience,* vol. 34, pp. 389-412, 2011.

[32] E. S. Boyden, F. Zhang, E. Bamberg, G. Nagel and K. Deisseroth, "Millisecond-timescale, genetically targeted optical control of neural activity," *Nature Neuroscience,* vol. 8, no. 9, pp. 1263-8, 2005.

[33] F. Zhang, L. P. Wang, M. Brauner, J. F. Liewald, K. Kay, N. Watzke, P. G. Wood, E. Bamberg, G. Nagel, A. Gottschalk and K. Deisseroth, "Multimodal fast optical interrogation of neural circuitry," *Nature,* vol. 446, no. 7136, pp. 633-9, 2007.

[34] F. Zhang, A. M. Aravanis, A. Adamantidis, L. de Lecea and K. Deisseroth, "Circuit-breakers: optical technologies for probing neural signals and systems.," *Nature Reviews Neuroscience,* vol. 8, no. 8, pp. 577-81, 2007.

[35] E. A. Pama, L. S. Colzato and B. Hommel, "Optogenetics as a neuromodulation tool in cognitive neuroscience," *Frontiers in psychology,* vol. 4, no. 610, 2013.

[36] K. Deisseroth, "Optogenetics," *Nature Methods,* vol. 8, p. 26–29, 2011.

[37] P. Ghanouni, K. B. Pauly, W. J. Elias, J. Henderson, J. Sheehan, S. Monteith and M. Wintermark, "Transcranial MRI-Guided Focused Ultrasound: A Review of the Technologic and Neurologic Applications," *American Journal of Roentgenology,* vol. 205, no. 1, pp. 150-159, 2015.

[38] S. S. Yoo, A. Bystritsky, J. H. Lee, Y. Zhang, K. Fischer, B. K. Min, N. J. McDannold, A. Pascual-Leone and F. A. Jolesz, "Focused ultrasound modulates region-specific brain activity," *Neuroimage,* vol. 156, no. 3, pp. 1267-1275, 2011.

[39] N. Lipsman, M. L. Schwartz, Y. Huang, L. Lee, T. Sankar, M. Chapman, K. Hynynen and A. M. Lozano, "MR-guided focused ultrasound thalamotomy for essential tremor: a proof-of-concept study," *The Lancet Neurology,* vol. 12, no. 5, pp. 462-8, 2013.

[40] A. E. Bond, B. B. Shah, D. S. Huss, R. F. Dallapiazza, A. Warren, M. B. Harrison, S. A. Sperling, X. Wang, R. Gwinn, J. Witt, S. Ro and W. J. Elias, "Safety and Efficacy of Focused Ultrasound Thalamotomy for Patients With Medication-Refractory, Tremor-Dominant Parkinson Disease, A Randomized Clinical Trial," *JAMA Neurology,* vol. 74, no. 12, pp. 1412-1418, 2017.

[41] W. E. Parker, E. K. Weidman, J. L. Chazen, S. N. Niogi, R. Uribe-Cardenas, M. G. Kaplitt and C. E. Hoffman, "Magnetic resonance-guided focused ultrasound for ablation of mesial temporal epilepsy circuits: modeling and theoretical feasibility of a novel noninvasive approach," *Journal of Neurosurgery,* pp. 1-8, 2019.

[42] S. J. Kim, D. Roh, H. H. Jung, W. S. Chang, C. H. Kim and J. W. Chang, "A study of novel bilateral thermal capsulotomy with focused ultrasound for treatment-refractory obsessive-compulsive disorder: 2-year follow-up," *Journal of Psychiatry & Neuroscience,* vol. 43, no. 5, pp. 327-337, 2018.

[43] W. J. Tyler, Y. Tufail, M. Finsterwald, M. L. Tauchmann, E. J. Olson and C. Majestic, "Remote excitation of neuronal circuits using low-intensity, low-frequency ultrasound," *PLoS One,* vol. 3, no. 10, p. e3511, 2008.

[44] H. L. Liu, M. Y. Hua, P. Y. Chen, P. C. Chu, C. H. Pan, H. W. Yang, C. Y. Huang, J. J. Wang, T. Yen and K. C. Wei, "Blood-brain barrier disruption with focused ultrasound enhances delivery of chemotherapeutic drugs for glioblastoma treatment," *Radiology,* vol. 255, no. 2, pp. 415-25, 2010.

[45] A. Kyriakou, E. Neufeld, B. Werner, M. M. Paulides, G. Szekely and N. Kuster, "A review of numerical and experimental compensation techniques for skull-induced phase aberrations in transcranial focused ultrasound," *International Journal of Hyperthermia,* vol. 30, no. 1, pp. 36-46, 2014.

[46] GBD 2015 Neurological Disorders Collaborator Group, "Global, regional, and national burden of neurological disorders during 1990–2015: a systematic analysis for the Global Burden of Disease Study 2015," *The Lancet Neurology,* vol. 16, no. 11, p. 877–897, 2017.

[47] World Health Organization, "Depression and Other: Global Health Estimates," 2017.

[48] OECD/EU, *Health at a Glance: Europe 2018: State of Health in the EU Cycle,* Paris: OECD Publishing, 2018.

[49] H. Kim, S. D. Lee, A. Chiu, S. S. Yoo and S. Park, "Estimation of the spatial profile of neuromodulation and the temporal latency in motor responses induced by focused ultrasound brain stimulation," *Neuroreport,* vol. 25, no. 7, p. 475–479, 2014.

[50] L. E. Kinsler, A. R. C. A. B. Frey and J. V. Sanders, Fundamentals of Acoustics, NewYork: John Wiley 6 Sons, Inc, 2000.

[51] R. S. C. Cobbold, Foundations of Biomedical Ultrasound, New York: Oxford University Press, 2007.

[52] V. F. Humphrey, "Ultrasound and matter–physical interactions.," *Progress in Biophysics & Molecular Biology,* vol. 93, no. 1-3, pp. 195-211, 2007.

[53] F. A. Jolesz and K. H. Hynynen, MRI-Guided Focused Ultrasound Surgery, New York: CRC Print, 2008.

[54] Olympus, *Ultrasonic Transducers Technical Notes,* Olympus NDT, 2006.

[55] H. W. Persson and C. Hertz, "Acoustic impedance matching of medical ultrasound transducers," *Ultrasonics,* vol. 23, no. 2, pp. 83-89, 1985.

[56] R. L. King, J. R. Brown, W. T. Newsome and K. B. Pauly, "Effective parameters for ultrasound-induced in vivo neurostimulation," *Ultrasound in Medicine & Biology ,* vol. 39, no. 2, pp. 312-331, 2013.

[57] W. D. O'Brien, "Ultrasound-biophysics mechanisms," *Progress in Biophysics & Molecular Biology,* vol. 93, no. 1-3, pp. 212-55, 2007.

[58] G. ter Haar, "Ultrasound bioeffects and safety," *Proceedings of the Institution of Mechanical Engineers,* vol. 224, no. 2, pp. 363-73, 2010.

[59] C. Amador, S. Aristizabal, J. F. Greenleaf and M. W. Urban, "Phase Aberration and Attenuation Effects on Acoustic Radiation Force-Based Shear Wave Generation," *IEEE Transactions on Ultrasonics, Ferroelectrics, and Frequency,* 2017.

[60] L. di Biase, F. E. and V. Di Lazzaro, "Transcranial Focused Ultrasound (tFUS) and Transcranial Unfocused Ultrasound (tUS) Neuromodulation: From Theoretical Principles to Stimulation Practices.," *Frontiers in Neurology,* vol. 10, no. 549, 2019.

[61] A. Fomenko, C. Neudorfer, R. F. Dallapiazza, S. K. Kalia and L. A. M. , "Low-intensity ultrasound neuromodulation: An overview of mechanisms and emerging human applications," *Brain Stimulation ,* vol. 11, no. 6, pp. 1209-1217, 2018.

[62] T. R. Nelson, J. B. Fowlkes, J. S. Abramowicz and C. C. Church, "Ultrasound biosafety considerations for the practicing sonographer and sonologist," *Journal of Ultrasound in Medicine,* vol. 28, no. 2, pp. 139-50, 2009.

[63] United States of America Food and Drug Administration, *Marketing Clearance of Diagnostic Ultrasound Systems and Transducers. Guidance for Industry and Food and Drug Administration Staff,* 2017.

[64] F. J. Fry, H. W. Ades and W. J. Fry, "Production of Reversible Changes in the Central Nervous System by Ultrasound," *Science,* vol. 127, no. 3289, p. 83–84, 1958.

[65] P. Rinaldi, J. P. Jones, F. Reines and L. R. Price, "Modification by focused ultrasound pulses of electrically evoked responses from an in vitro hippocampal preparation," *Brain Research,* vol. 558, no. 1, pp. 36-42, 1991.

[66] M. R. Bachtold, P. C. Rinaldi, J. P. Jones, F. Reines and L. R. Price, "Focused ultrasound modifications of neural circuit activity in a mammalian brain," *Ultrasound in Medicine & Biology,* vol. 24, no. 4, p. 557–565, 1998.

[67] P. H. Tsui, S. H. Wang and C. C. Huang, "In vitro effects of ultrasound with different energies on the conduction properties of neural tissue," *Ultrasonics,* vol. 43, no. 7, pp. 560-565, 2005.

[68] S. S. Yoo, H. Kim, B. K. Min, E. Franck and S. Park, "Transcranial focused ultrasound to the thalamus alters anesthesia time in rats," *Neuroreport,* vol. 22, no. 15, pp. 783-787, 2011.

[69] Y. Younan, T. Deffieux, B. Larrat, M. Fink, M. Tanter and J. F. Aubry, "Influence of the pressure field distribution in transcranial ultrasonic neurostimulation," *Medical Physics,* vol. 40, no. 8, p. 082902, 2013.

[70] T. Deffieux, Y. Younan, N. Wattiez, M. Tanter, P. Pouget and J. Aubry, "Low-Intensity Focused Ultrasound Modulates Monkey Visuomotor Behavior," *Current Biology,* vol. 23, no. 23, pp. 2430-2433, 2013.

[71] W. Lee, S. D. Lee, M. Y. Park, L. Foley, E. Purcell-Estabrook, H. Kim, K. Fischer, L. S. Maeng and Y. S. S. , "Image-Guided Focused Ultrasound-Mediated Regional Brain Stimulation in Sheep," *Ultrasound in Medicine and Biology,* vol. 42, no. 2, p. 459–470, 2016.

[72] R. F. Dallapiazza, K. F. Timbie, S. Holmberg, J. Gatesman, M. B. Lopes, P. R. J. G. W. Miller and W. J. Elias, "Noninvasive neuromodulation and thalamic mapping with low-intensity focused ultrasound," *Journal of Neurosurgery,* vol. 128, no. 3, pp. 875-884, 2018.

[73] P. P. Ye, J. R. Brown and K. B. Pauly, "Frequency Dependence of Ultrasound Neurostimulation in the Mouse Brain," *Ultrasound in Medicine & Biology,* vol. 42, no. 7, p. 1512–1530, 2016.

[74] H. Baek, K. J. Pahk, M. J. Kim, Y. I. and H. Kim, "Modulation of Cerebellar Cortical Plasticity Using Low-Intensity Focused Ultrasound for Poststroke Sensorimotor Function Recovery," *Neurorehabilitation and Neural Repair,* vol. 32, no. 9, pp. 777-787, 2018.

[75] W. Lee, S. D. Lee, M. Y. Park, L. Foley, E. Purcell-Estabrook, H. Kim, K. Fischer and L. S. Y. S. S. Maeng, "Image-Guided Focused Ultrasound-Mediated Regional Brain Stimulation in Sheep," *Ultrasound in Medicine & Biology,* vol. 42, no. 2, pp. 459-70, 2016.

[76] W. Lee, Y. A. Chung, Y. Jung, S. I. U. and S. S. Yoo, "Simultaneous acoustic stimulation of human primary and secondary somatosensory cortices using transcranial focused ultrasound," *BMC Neuroscience,* vol. 17, no. 1, p. 68, 2016.

[77] V. Colucci, G. Strichartz, F. Jolesz, N. Vykhodtseva and K. Hynynen, "Focused ultrasound effects on nerve action potential in vitro," *Ultrasound in Medicine & Biology,* vol. 35, no. 10, p. 1737–1747, 2009.

[78] J. Kubanek, P. Shukla, A. Das, S. A. Baccus and M. B. Goodman, "Ultrasound Elicits Behavioral Responses through Mechanical Effects on Neurons and Ion Channels in a Simple Nervous System," *The Journal of Neuroscience,* vol. 12, no. 3081–3091, p. 38, 2018.

[79] A. G. Petrov, "Flexoelectric Model For Active Transport," *Physical and Chemical Bases of Biological Information Transfer,* p. 111–125, 1975.

[80] T. Heimburg and A. D. Jackson, "On soliton propagation in biomembranes and nerves," *Proceedings of the National Academy of Sciences,* vol. 102, no. 28, pp. 9790-9795, 2005.

[81] B. Krasovitski, V. Frenkel, S. Shoham and E. Kimmel, "Intramembrane cavitation as a unifying mechanism for ultrasound-induced bioeffects," *Proceedings of the National Academy of Sciences,* vol. 108, no. 8, pp. 3258-3263, 2011.

[82] M. Plaksin, S. Shoham and E. Kimmel, "Intramembrane cavitation as a predictive bio-piezoelectric mechanism for ultrasonic brain stimulation," *Physical Review X,* vol. 4, no. 1, p. 1–10, 2014.

[83] M. Plaksin, E. Kimmel and S. Shoham, "Cell-Type-Selective Effects of Intramembrane Cavitation as a Unifying Theoretical Framework for Ultrasonic Neuromodulation," *eNeuro,* vol. 3, no. 3, 2016.

[84] H. Guo, M. Hamilton, S. J. Offutt, C. D. Gloeckner, T. Li, Y. Kim, W. Legon, J. K. Alford and H. H. Lim, "Ultrasound Produces Extensive Brain Activation via a Cochlear Pathway," *Neuron,* vol. 98, no. 5, pp. 1020-1030, 2018.

[85] T. Sato, M. G. Shapiro and D. Y. Tsao, "Ultrasonic Neuromodulation Causes Widespread Cortical Activation via an Indirect Auditory Mechanism," *Neuron,* vol. 98, no. 5, pp. 1031-1041, 2018.

[86] M. Mohammadjavadi, P. P. Ye, A. Xia, J. Brown, G. Popelka and K. B. Pauly, "Elimination of peripheral auditory pathway activation does not affect motor responses from ultrasound neuromodulation," *Brain Stimulation,* vol. 12, no. 4, pp. 901-910, 2019.

[87] W. Legon, T. F. Sato, A. Opitz, J. Mueller, A. Barbour, A. Williams and W. J. Tyler, "Transcranial focused ultrasound modulates the activity of primary somatosensory cortex in humans," *Nature Neuroscience,* vol. 17, no. 2, pp. 322-329, 2014.

[88] W. Lee, H. C. Kim, Y. Jung, Y. A. Chung, I. U. Song, J. H. Lee and S. S. Yoo, "Transcranial focused ultrasound stimulation of human primary visual cortex," *Scientific Reports,* vol. 6, no. 34026, 2016.

[89] M. M. Monti, C. Schnakers, A. S. Korb, A. Bystritsky and P. M. Vespa, "Non-Invasive Ultrasonic Thalamic Stimulation in Disorders of Consciousness after Severe Brain Injury: A First-in-Man Report," *Brain Stimulation,* vol. 9, no. 6, pp. 940-941, 2016.

[90] W. Legon, P. Bansal, R. Tyshynsky, L. Ai and J. K. Mueller, "Transcranial focused ultrasound neuromodulation of the human primary motor cortex," *Scientific Reports,* vol. 8, no. 10007, 2018.

[91] NEMA, *Acoustic Output Measurement Standard For Diagnostic Ultrasound Equipment,* National Electrical Manufacturers Association, 2004.

[92] S. Hippenmeyer, E. Vrieseling, M. Sigrist, T. Portmann, C. Laengle, D. R. Ladle and S. Arber, "A Developmental Switch in the Response of DRG Neurons to ETS Transcription Factor Signaling," *PLoS Biology,* vol. 3, no. 5, p. e159, 2005.

[93] L. Madisen, T. Mao, H. Koch, J. Zhuo, A. Berenyi , S. Fujisawa, Y. A. Hsu, A. J. Garcia III, X. Gu, S. Zanella, J. Kidney, H. Gu, Y. Mao, B. M. Hooks, E. S. Boyden, G. Buzsáki, J. M. Ramirez, A. R. Jones, X. Han4, X. Han, E. E. Turner and H. Zeng, "A toolbox of Cre-dependent optogenetic transgenic mice for light-induced activation and silencing," *Nature Neuroscience,* vol. 15, no. 5, pp. 793-802, 2012.

[94] H. Taniguchi , M. He, P. Wu, S. Kim, R. Paik, K. Sugino, D. Kvitsiani , Y. Fu, J. Lu, Y. Lin, G. Miyoshi, Y. Shima, G. Fishell, S. B. Nelson and Z. J. Huang, "A Resource of Cre Driver Lines for Genetic Targeting of GABAergic Neurons in Cerebral Cortex," *Neuron,* vol. 71, no. 6, pp. 995-1013, 2011.

[95] G. J. Gage, D. R. Kipke and W. Shain, "Whole Animal Perfusion Fixation for Rodents," *Journal of Visualized Experiments,* vol. e3564, no. 65, p. 1–9, 2012.

[96] J. T. Ting, T. L. Daigle, Q. Chen and G. Feng, "Acute Brain Slice Methods for Adult and Aging Animals: Application of Targeted Patch Clamp Analysis and Optogenetics," *Patch-Clamp Methods and Protocols, Methods in Molecular Biology,* vol. 1183, pp. 221-242, 2014.

[97] S. Huang and M. Uusisaari, "Physiological temperature during brain slicing enhances the quality of acute slice preparations," *Frontiers in Cellular Neuroscience,* vol. 7, no. 48, pp. 1-8, 2013.

[98] J. H. Siegle, A. C. López, Y. A. Patel, K. Abramov, S. Ohayon and J. Voigts, "Open Ephys: An open-source, plugin-based platform for multichannel electrophysiology," *Journal of Neural Engineering,* vol. 14, no. 4, 2017.

[99] J. H. Siegle, . A. C. López, Y. A. Patel, K. Abramov, O. S. and J. Voigts, "Open Ephys: An open-source, plugin-based platform for multichannel electrophysiology," *Journal of Neural Engineering,* vol. 14, no. 4, 2017.

[100] E. H. Chang, S. A. Frattini, S. Robbiati and P. T. Huerta, "Construction of microdrive arrays for chronic neural recordings in awake behaving mice," *Journal of Visualized Experiments,* no. 77, p. 1–8, 2013.

[101] D. P. Nguyen, S. P. Layton, G. Hale, S. N. Gomperts, T. J. Davidson, F. Kloosterman and M. A. Wilson, "Micro-drive array for chronic in vivo recording: tetrode assembly," *Journal of Visualized Experiments,* no. 26, p. 7–9, 2009.

[102] J. E. Ferguson, C. Boldt and A. D. Redish, "Creating low-impedance tetrodes by electroplating with additives," *Sensors and Actuators A: Physical,* vol. 156, no. 2, p. 388–393, 2009.

[103] Neuralynx, *Neuralynx Plating Solutions and Protocols User Manual,* Neuralynx, Inc., 2015.

[104] R. Q. Quiroga and Z. Nadasdy, "Unsupervised Spike Detection and Sorting with Wavelets and Superparamagnetic Clustering," *Neural Computation,* vol. 16, p. 1661–1687, 2004.

[105] M. S. Lewicki, "A review of methods for spike sorting: the detection and classification of neural action potentials," *Network: Computation in Neural Systems,* vol. 9, p. R53–R78, 1988.

[106] S. Takahashi, Y. Anzai and Y. Sakurai, "A new approach to spike sorting for multi-neuronal activities recorded with a tetrode–how ICA can be practical," *Neuroscience Research,* vol. 46, no. 3, pp. 265-72, 2003.

# Appendices

## Appendix I – Publications

**Title:**

"Low Intensity Focused Ultrasound Modulation of Neural Circuits Activity"

**Authors:**

Francisca Machado, Ricardo Magalhães, Paulo M. Mendes, Nuno Sousa

**Published in:**

IEEE 6th Portuguese Meeting on Bioengineering (ENBENG)

**Year:**

2019

**Abstract:**

Ultrasound neuromodulation (UNMOD) has gained popularity as a new state-of-the-art technique for the research and treatment of neurological and psychiatric illnesses. Ultrasounds (US) can be transmitted in a noninvasive manner to deep-brain regions with a focus of a few millimeters in size. In this review, we perform an analysis of literature describing the mechanical effects underlying focused ultrasound stimulation (FUS) and their effective modulation of neural functions. We also review distinct stimulation parameters, experimental set-ups and protocols to better understand the current limits and challenges of this technique.

**DOI:**

10.1109/ENBENG.2019.8692516

# Low Intensity Focused Ultrasound Modulation of Neural Circuits Activity

Francisca Machado[1,2], Ricardo Magalhães[1,2], Paulo M. Mendes[3] and Nuno Sousa[1,2]

[1] *Life and Health Sciences Research Institute (ICVS), School of Medicine, University of Minho, Braga, Portugal,* [2] *ICVS/3B's - PT Government Associate Laboratory, Braga, Portugal,* [3]*CMEMS -UMinho, University of Minho, Guimarães, Portugal.*

***Abstract— Ultrasound neuromodulation (UNMOD) has gained popularity as a new state-of-the-art technique for the research and treatment of neurological and psychiatric illnesses. Ultrasounds (US) can be transmitted in a non-invasive manner to deep-brain regions with a focus of a few millimeters in size. In this review, we perform an analysis of literature describing the mechanical effects underlying focused ultrasound stimulation (FUS) and their effective modulation of neural functions. We also review distinct stimulation parameters, experimental set-ups and protocols to better understand the current limits and challenges of this technique.***

**Index Terms —Ultrasound Neuromodulation (UNMOD), Focused Ultrasound Stimulation (FUS), Low Intensity Focused Ultrasound (LIFU).**

## I. INTRODUCTION

According to recent studies (1), millions of people world-wide suffer from a neurological or psychiatric disorder. Hence, for the past few decades there has been a growing interest and need for the development of novel neuromodulation techniques as a route of treatment for such illnesses of both central and peripheral nervous systems. Conventional techniques like deep brain stimulation (DBS) (2) have been widely employed as efficient therapeutic approaches for the relief of neurological chronic diseases, yet they require invasive interventions and, consequently hazardous side effects can arise. On the other hand, non-invasive methods such as transcranial magnetic stimulation (TMS) and transcranial direct current stimulation (tDCS) are characterized by insufficient spatial resolution (3; 4). Furthermore, optogenetic techniques have also exhibited the ability of changing brain activity through photostimulation, but the demand for genetic modifications and the inclusion of light sensitive-proteins (opsins) through surgery constitute severe hurdles for its application in humans (5).

Focused ultrasound stimulation (FUS) is a cutting-edge neurostimulation tool, which has emerged as a potential substitute for the aforementioned methods by providing a transcranial modulation of specific cortical functions, removing the need for surgical intervention. The acoustic energy is focally delivered until reaching the desire target regions, facilitating the stimulation of superficial or deep neuronal activity with a high spatial-accuracy (on the order of millimeters in diameter) and without affecting the surrounding areas of the sonicated regions (6). Furthermore, through the integration of a compatible sonication setup with excellent temporal and spatial resolution imaging techniques, like magnetic resonance imaging (MRI), it is possible to achieve a brain-mapping system, namely an MRI-guided focused ultrasound (MRgFUS). This system enables an enhanced precision and real-time targeting and monitorization of the sonicated structures, but in order to obtain both anatomical and functional information, a functional magnetic resonance imaging (fMRI) acquisition should be coupled with the experimental setup (7). Thus, clinical results of sonication can be characterized by blood oxygenation level-dependent (BOLD) signals, which are connected to the activation or suppression of neuronal activity (8). Previously stated techniques are loosing momentum to FUS, since methodologies like DBS and TMS have a deficient compatibility with MRI and can produce unwanted effects, either by the use of implantable stimulating electrodes or electromagnetic coils, respectively, that interfere with the electromagnetic field of the MRI scanner during the stimulation process (9; 10).

Therapeutic ultrasound is capable of producing different interactions with the sonicated regions, namely thermal and non-thermal (acoustic streaming, cavitation and radiation) effects. One of the most common uses for thermal energy deposition is the stereotactic ablation of tissue, performed with a high intensity focused ultrasound (HIFU), mainly for the treatment of tumor of the kidney, thyroid and brain, among others (11). By using a thermal energy below the ablation threshold, HIFU can produce an effective modulation for the treatment of neurological diseases such as essential tremor (ET) (12). Contrarily, low intensity focused ultrasound (LIFU), in pulsed mode, has a low risk of provoking irreversible cell damage or apoptosis while still being able of penetrating the skull barrier, thus being the main focus of late UNMOD studies (4). Nevertheless, transcranial FUS is not without hurdles. One of the biggest obstacles in *in vivo* experiments for therapeutic UNMOD is the subject's skull. This barrier triggers phenomena like phase aberration in the focusing and a lower efficiency energy transmission. This issue can be overcome by numerical and experimental compensation techniques such as multi-element transducers, compensation software (CT correction algorithms) and simulations, for example (13).

## II. FUS NEUROMODULATION

In an important study, by way of confocal imaging and electrophysiological recordings in *in vitro* hippocampal slice cultures, Tyler *et al.* (14) showed that low frequency, low intensity ultrasound pulsations are capable of directly evoking electrical neural activity (action potentials (APs) and synaptic transmissions) in the CNS, possibly by triggering voltage-gated sodium and calcium channels. These results triggered a series of experimental trials that targeted the cortex of anesthetized rodents (15; 16; 17; 18; 6), rabbits (7), pigs (19) and non-human

primates (20), aiming to discover the optimal acoustic stimulation parameters and pulsing protocols that enable an efficient *in vivo* neuromodulation. In fact, the same research group reported motor responses as a result of modulating intact mouse brains with transcranial pulsed US, along with a specific protocol for *in vivo* neurostimulation, including both continuous and pulsed stimulus (15; 21). Moreover, with a compatible fMRI monitorization and electromyography (EMG) recordings, Yoo *et al*. verified via BOLD fMRI signals that FUS (0.05-50 ms of 0.69 MHz US, $I_{SPPA}$ = 3.3-12.6 W/cm$^2$) can evoke and suppress neural activity (bimodal modulation) in the cortex of rabbits (visual and motor), without provoking histological tissue or blood-brain barrier (BBB) damage (7). This group also found that FUS can decrease the emergence time of voluntary limb movement from general anesthesia, by applying US pulses (0.5 ms of 650 MHz US, $I_{SPPA}$ = 3.3 W/cm$^2$) to the thalamus of anesthetized rats (16). Further investigations were conducted by shifting the US parameters and gathering of experimental data of motor responses, indicating that the efficacy of the stimulation increases as a function of the US duration and intensity, weakening with a deeper anesthesia and a higher frequency US carrier (18). Therefore, the anesthesia level influences the US modulatory effects (16; 18; 6).

Concerning large brain animal models, Deffieux *et al.* (20) conducted short pulsed LIFU (100 ms of 0.32 MHz US, $I_{SPTA}$ = 4 ± 1.1 W/cm$^2$) sonications in the frontal eye field (FEF) of awake nonhuman primates (during a visual task), revealing that LIFU has the ability to modulate anti-saccade (AS) latencies. Furthermore, Dallapiazza and colleagues (19) found that pulsed LIFU is able to modulate deep-brain functions in the pig thalamus, concluding that longer duration pulses and sonication durations can reduce neural activity, without damaging the targeted brain areas. Regarding human trials, studies revealed that transcranial FUS can modulate the human primary somatosensory (S1) (500 ms of 0.5 MHz US, $I_{SPPA}$=23.87 W/cm$_2$) (22) and visual (V1) cortex (23), as shown by evoked potentials recorded by EEG and fMRI acquisitions. In other up-to-date researches, miniaturized and compact UNMOD systems have been developed, namely a portable ultrasound neuro-stimulation system (24) and a miniaturized transducer (25), that revealed a successful neuromodulation in intact mouse brains with minimal invasive procedures.

In spite of the abundant findings of the aforementioned studies, the precise mechanisms behind UNMOD, at a cellular and molecular scale, are still elusive. One hypothesis is the modulation of neural tissue through heating (as a result of acoustic energy absorption); however, this has been contradicted by data showing that the activation of brain regions was associated with minor temperature increases (15). Another theory is the modulation of neural activity via US-induced mechanical (non-thermal) effects, namely cavitation, acoustic streaming, and radiation forces or a combination of these effects (19; 26; 4). For example, according to Tyler *et al.* (14), the activation of voltage-gated ion-channels evokes action potentials and synaptic transmissions when delivering LIFU to neural regions, considering that the mechanical modification of mechano-sensitive voltage-gated ion-channels results in the modulation of the ion channel's kinetic state.

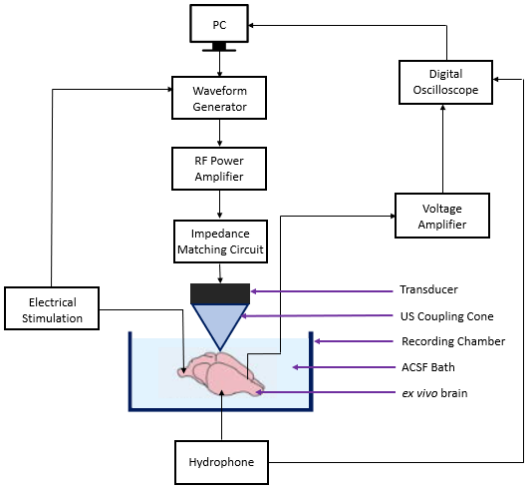


*Figure 1- Schematic diagram of the experimental sonication set-up.*

## III. Low Intensity Focused Ultrasound Experimental Set-Up

In this sub-chapter, we will describe our LIFU set-up. The designed experimental sonication set-up, described in Figure 1, is based upon earlier *in vitro* studies (27; 28; 14) and later transcranial neuromodulation researches (16; 17). For instance, the *ex vivo* brain was placed amid the focal zone of the ultrasound transducer, in a recording chamber with an artificial cerebral spinal fluid (ACSF) bath that ensures the viability of the tissue in study. Furthermore, bipolar stimulating and recording electrodes were immobilized and partly submerged, with the purpose of evoking a compound action potential (CAP – illustrates the algebraic sum of individual action potentials) signal and consequently eliciting activity in the different regions of the hippocampal slices, which is subsequently amplified and displayed in a digital oscilloscope.

### *A. Waveform Generation*

Regarding the transducer's supply, an ultrasonic wave can be obtained through a signal generator, ideally connected to a control system that enables the operator to adjust parameters of the US wave and the stimulation of several target neural areas (24). The transducer is operated through high voltage pulses (square waves). As a consequence, a radio-frequency (RF) power amplifier must be connected to the waveform generator to control the electric pulse (27). A matching impedance layer must be incorporated in the set-up, as to improve the signal-to--noise ratio (SNR) as well as to match the transducer's electrical impedance with the power amplifier's output impedance (24).

### *B. Transducer*

To minimize signal reflection and improve the transducer performance, a λ/4 thick matching layer with a similar acoustic impedance to the piezoelectric crystal can be used to achieve an optimal impedance matching. Additionally, the single element transducer should be air-backed in order to accomplish a minimal energy loss neuromodulation (24). As observed in Figure 1, a coupling cone, filled with degassed water (which di-minishes the absorption and distortion of the ultrasonic waves), was placed between the FUS transducers and the hippocampal slices, securing the ultrasonic coupling between the transducer

*Table 1 - Ultrasound neuromodulation parameters from selected papers.*

| Author/Year | Region | Frequency (MHz) | PRF (Hz) | Duration | Energy |
|---|---|---|---|---|---|
| Tyler *et al.*, 2008 (14) | *In vitro*: Mice hippocampal slice cultures | 0.44-0.66 | 0-100 | Tone-burst duration:0.0223-0.18 ms;<br>Cycles per tone-burst:10;<br>Number of tone-burst:3-250 | $I_{SPTA}$=0.023 W/cm$^2$<br>$I_{SSPA}$= 2.9 W/cm$^2$ |
| Tufail *et al.*, 2010 (15) | Mouse motor cortex<br>Mouse hippocampus | 0.25–0.50 | 1200-3000 | Pulse duration:0.16–0.57ms<br>Cycles per pulse: 80- 225<br>Stimulus duration:26-333 ms | $I_{SPTA}$=0.021–0.163 W/cm$^2$<br>$I_{SSPA}$=0.075–0.229 W/cm$^2$ |
| Younan *et al.*, 2013 (17) | Rat motor cortex | 0.32 | 2000 | Pulse duration:230 µs<br>Cycles per pulse:75<br>Total Burst duration:250 ms | $I_{SPPA}$=17.5 ± 7.5 W/cm$^2$ |
| Lee *et al.*, 2016 (23) | Human primary visual cortex | 0.27 | 500 | Sonication duration:300 ms<br>Tone Burst duration:1 ms | $I_{SPPA}$=0.7-6.6 W/cm$^2$ |
| Dallapiaza *et al.*, 2018 (19) | Pig thalamus | 0.22-1.14 | 10 | Pulse duration:43.7 ms | $I_{SA}$= 25-30 W/cm$^2$ |

and the target region (28). Nevertheless, ultrasonic gel should be placed upon the transducer's surface with the purpose of avoiding bubble adhesion during the set-up assemblage process (18).

**Transducer Calibration**

The transducer calibration can be accomplished through the use of a calibrated hydrophone mounted on a *xyz*-manipulator, being that it should be faced parallel to and vertically over the centre of the transducer (location of maximal pressure). Henceforth, through the characterization of US pressure profiles within the acoustic field, it is possible to determine the transducer's focal point and its properties, such as its shape, position and acoustic intensity (spatial-average intensity ($I_{SA}$), maximum spatial-peak pulse-average intensity ($I_{SPPA}$) and spatial-peak temporal- average intensity ($I_{SPTA}$)) (7) (21).

**Sonication Parameters Selection**

The stimulation of specific brain regions can be optimized by adjusting the US wave parameters (transmission mode, acoustic frequency, pulse duration, pulse repetition frequency, acoustic intensity and exposure time, among others).

According to King *et al.* (18), both Continuous-wave (CW) and Pulsed-wave (PW) transmission modes are capable of eliciting brain activity, provided that the $I_{SPTA}$ are equated. However, in this paper, we opted for a modulation with pulsed bursts, considering that short US pulses avoid hazards such as tissue overheating and the decrease of neural function, being employed by many neuromodulation studies (15; 20; 23). Regarding the acoustic frequency, a low intensity ultrasound wave operating at a fundamental frequency lower than 1 MHz can be used to stimulate brain activity through an undamaged skull. Lower frequencies diminish the attenuation of the acoustic energy when it interacts with tissue, yet the penetration depth is also reduced and the focal point width enhanced (18). In resemblance to previous *in vitro* trials (27; 28) , we selected a transducer with a fundamental frequency ($f_0$) of 500 kHz, knowing that a bandwidth of 440-700 kHz presents the most favourable gains between FUS transmission through skull bone and brain absorption (7). Likewise, according to Tufail *et al.* (21) the optimal acoustic frequencies for eliciting brain activity in intact mice brains lie between 0.25 and 0.65 MHz, which once more reinforces our parameters choice.

On the aspect of biosafety the chosen acoustic output levels must be in agreement with the specified maximum acoustic intensities by the FDA for diagnosis imaging purposes. This entity stipulates an $I_{SPPA}$ and $I_{SPTA}$ of 720 mW/cm$^2$ and 190 W/cm$^2$ or less, respectively (29). FUS pulses with $I_{SPPA}$ values below 3 W/cm$^2$ have been proven by Tyler et al. (14) capable of activating voltage-gated sodium and calcium channels, while Yoo *et al.* (7) demonstrated that excitatory effects in rabbits can be elicited through the transmission of FUS pulses with a 3.3 W/cm$^2$ $I_{SPPA}$ and a 160 W/cm$^2$ $I_{SPTA}$, which are below the FDA limits. Table 1 presents a sample of ultrasound parameters in the literature, employed as a base framework.

## IV. Future Work

The present work's objective is to investigate and successfully modulate the activity of in *in vitro* brain tissue and characterize the neurophysiological mechanisms triggered by ultrasound. Furthermore, we aim to ascertain the optimal ultrasound intensity or pressure threshold through a broader variation of the acoustic parameters (frequency, pulse repetition frequency), that empower a favourable targeting and stimulation of neural regions, without the risk of ablating or damaging brain tissue. To achieve such a purpose the main tasks will consist in:

- assembling and characterizing a low intensity FUS experimental set-up (similar to the aforementioned);
- electrical stimulation and measurement of the *ex vivo* brain compound action potentials (CAPs) before and during each tissue sonication procedure;
- construction and transmission of pulsed ultrasound into the target nervous areas;
- exploration and selection of the optimal acoustic parameters through the application of different stimuli, based on the revised literature. Hence, we aim to test and analyse the influence of US parameters in the neuromodulation process;
- experimental validation of the stimulation paradigm with electrophysiological studies and assessment of the US-induced effects (thermal or mechanical) accountable for the modification of neuronal activity.

## V. Conclusion

The reviewed literature confirms the promising potential of US as a therapeutic method in neurosciences, creating an opportunity for the replacement of techniques such as DBS,

TMS and tDCS in the treatment of neurologic diseases. Ergo, low-intensity FUS enables a new procedure to modulate brain activity in a non-invasive and undamaging approach. Nonetheless, further investigation in mammalian neuronal function is still necessary in order to unravel the mechanisms responsible for the US modulatory effects, as well as the optimal *in vivo* neurostimulation acoustic parameters.

## VI. Acknowledgments

This work and FM were funded by the Fundação Calouste Gulbenkian (Portugal) (Contract grant number: P-139977; project "Better mental health during ageing based on temporal prediction of individual brain ageing trajectories (TEMPO)"), and co-financed by the Portuguese North Regional Operational Program (ON.2 – O Novo Norte), under the National Strategic Reference Framework (QREN), through the European Regional Development Fund (FEDER).

## VII. References

1. **GBD 2015 Neurological Disorders Collaborator Group.** Global, regional, and national burden of neurological disorders during 1990–2015: a systematic analysis for the Global Burden of Disease Study 2015. *Lancet Neurology.* s.l. : Elsevier, 2015. Vols. 16: 877–97.

2. **Benabid, A. L ., et al.** Deep brain stimulation of the subthalamic nucleus for the treatment of Parkinson's disease. *The Lancet: Neurology.* 2009. Vol. 8, (1):67-81.

3. **Miniussi, C., et al.** Efficacy of repetitive transcranial magnetic stimulation/transcranial direct current stimulation in cognitive neurorehabilitation. *Brain Stimulation.* s.l. : Elsevier, 2008. Vol. 1, (4):326–36.

4. **Tyler, W. J., Lani, S. W. and Hwang, G. M.** Ultrasonic modulation of neural circuit activity. *Current Opinion in Neurobiology.* s.l. : Elsevier, 2018. Vols. 50:222-231.

5. **Mahmoudi, P., Veladi, H. and Pakde, F. G.** Optogenetics, Tools and Applications in Neurobiology. *Journal of Medical Signals and Sensors.* 2017. Vol. 7, (2):71–79.

6. **Kim, H., et al.** Estimation of the spatial profile of neuromodulation and the temporal latency in motor responses induced by focused ultrasound brain stimulation. *Neurophysiology.* s.l. : Neuroreport, 2014. Vol. 25, (7):475–479.

7. **Yoo, S. S., et al.** Focused ultrasound modulates region-specific brain activity. *NeuroImage.* s.l. : Elsevier, 2011. 56: 1267–1275.

8. **Soares, J., et al.** A Hitchhiker's Guide to Functional Magnetic Resonance Imaging . *Frontiers in Neuroscience.* 2016. Vol. 10, 515.

9. **Dormont, D., et al.** Neuroimaging and Deep Brain Stimulation. s.l. : AJNR Am. J. Neuroradiol., 2010. Vol. 31, (1):15-23.

10. **Bohning, D. E., et al.** A combined TMS/fMRI study of intensity-dependent TMS over motor cortex. s.l. : Society of Biological Psychiatry, 1999. Vol. 45, (4):385-394.

11. **Zhou, Y. F.** High intensity focused ultrasound in clinical tumor ablation. *World Journal of Clinical Oncology.* s.l. : Baishideng Publishing Group Co., 2011. Vol. 2, (1): 8–27.

12. **Elias, W. J., et al.** A Randomized Trial of Focused Ultrasound Thalamotomy for Essential Tremor. *The New England Journal of Medicine.* s.l. : Massachusetts Medical Society, 2016. Vol. 375, (8):730-9.

13. **Kyriakou, A., et al.** A review of numerical and experimental compensation techniques for skull-induced phase aberrations in transcranial focused ultrasound. *International Journal of Hyperthermia.* 2013. Vol. 30, (1):36-46.

14. **Tyler, W. J., et al.** Remote Excitation of Neuronal Circuits Using Low-Intensity, Low-Frequency Ultrasound. *PLoS One.* 2008. Vol. 3, (10):e3511.

15. **Tufail, Y., et al.** Transcranial Pulsed Ultrasound Stimulates Intact Brain Circuits. *Neuron.* s.l. : Elsevier, 2010. Vol. 66, (5):681-94.

16. **Yoo, S. S., et al.** Transcranial focused ultrasound to the thalamus alters anesthesia time in rats. *Neuroreport.* 2011. Vol. 22, (15):783.

17. **Younan , Y., et al.** Influence of the pressure field distribution in transcranial ultrasonic neurostimulation. *Medical Physics.* s.l. : The American Association of Physicists in Medicine, 2013. Vol. 40, (8):082902.

18. **King, R. L., et al.** Effective parameters for ultrasound-induced in vivo neurostimulation. *Ultrasound in Medicine & Biology.* s.l. : Elsevier, 2013. Vol. 39, (2):312–331.

19. **Dallapiazza, R.F., et al.** Noninvasive neuromodulation and thalamic mapping with low-intensity focused ultrasound. *Journal of Neurosurgery.* s.l. : American Association of Neurological Surgeons, 2018. Vol. 128, (3):875-884.

20. **Deffieux, T., et al.** Low-Intensity Focused Ultrasound Modulates Monkey Visuomotor Behavior. *Current Biology.* 2013. Vol. 23, (23):2430-3.

21. **Tufail, Y., et al.** Ultrasonic neuromodulation by brain stimulation with transcranial ultrasound. *Nature Protocols.* s.l. : Nature America, 2011. Vol. 6, (9):1453-1470.

22. **Legon, W., et al.** Transcranial focused ultrasound modulates the activity of primary somatosensory cortex in humans. *Nature Neuroscience.* s.l. : PLOS ONE, 2014. Vol. 17, (2):322-9.

23. **Lee, W., et al.** Transcranial focused ultrasound stimulation of human primary visual cortex. *Scientific Reports.* 2016. Vol. 6, 34026.

24. **Qiu, W., et al.** A Portable Ultrasound System for Non-Invasive Ultrasonic Neuro-Stimulation. *Neural Systems and Rehabilitation Engineering.* s.l. : IEEE Transactions, 2017. 1534-4320.

25. **Kim, H., Kim, S. and Lee, H. J.** Capacitive Micromachined Ultrasonic Transducer (CMUT) ring array for transcranial ultrasound neuromodulation. *Annual International Conference of the IEEE Engineering in Medicine and Biology Society.* s.l. : IEEE Engineering in Medicine and Biology Society, 2018. 2675-2678.

26. **Kubanek, J., et al.** Ultrasound elicits behavioral responses through mechanical effects on neurons and ion channels in a simple nervous system. *Journal of Neuroscience.* 2018. Vol. 38, (12):3081-3091.

27. **Bachtold, M. R., et al.** Focused ultrasound modifications of neural circuit activity in a mammalian brain. *Ultrasound in Medicine & Biology.* s.l. : Elsevier, 1998. Vol. 24, (4):557-565.

28. **Tsui , P. H., Wang , S. H. and Huang, C. C.** In vitro effects of ultrasound with different energies on the conduction properties of neural tissue. *Ultrasonics.* s.l. : Elsevier, 2005. Vol. 43, (7):560-5.

29. **American Institute of Ultrasound in Medicine.** How to Interpret the Ultrasound Output Display Standard for Higher Acoustic Output Diagnostic Ultrasound Devices. *Journal of Ultrasound in Medicine.* 2004. (23):723–726.

# Appendix II – Spike Detection and Sorting Algorithms

```
% input arguments: data = 4xdata array with the signals from 1 tetrode
%                  multiplier = estimation of the noise standard deviation's multiplier
%                  time_window = minimum peak-to-peak distance
%                  t = time vector
function [time,time_stamps_all] = spikedetection(data,multiplier,time_window,t)
% amplitude threshold
ss = [];
% for each channel of a tetrode
for i = 1:size(data,1)
    s = [];
    % estimation of the noise standard deviation
    sdt = median(abs(data(i,:)/0.6745));
    % threshold
    th = multiplier*sdt;
    for j = 2:size(data(i,:),2)-1
        if data(i,j)> 0 && data(i,j)-data(i,j-1)> 0 && data(i,j)-data(i,j+1)> 0 && data(i,j)>th
            % saves the time_stamps of a single channel in a array
            s =[s,j];
            % saves the time_stamps of all channels in a array
            ss = [ss,j];
        end
    end
    % cell array with all the time_stamps per channel
    stamps(i,:) = {s};
end

% peak-to-peak threshold
for i = 1:size(data,1)
    stamp = cell2mat(stamps(i,:));
    time_stamps = stamp(1,1);
    % peak-to-peak distance threshold
    for j = 2:size(stamp,2)-1
        if (stamp(1,j)-stamp(1,j-1))>time_window && (stamp(1,j+1)-stamp(1,j))>time_window
            time_stamps = [time_stamps,stamp(1,j)];
        end
    end
    time_stamps = [time_stamps,stamp(1,end)];
    % cell array with all the time_stamps per channel
    time(i,:) = {time_stamps};

    % peak-to-peak threshold
    stamps_all = unique(ss);
    time_stamps_all = stamps_all(1,1);
    % peak-to-peak distance threshold
    for j = 2:size(stamps_all,2)-1
        if (stamps_all(1,j)-stamps_all(1,j-1))>time_window && (stamps_all(1,j+1)-stamps_all(1,j))>time_window
            time_stamps_all = [time_stamps_all,stamps_all(1,j)];
        end
    end
    time_stamps_all = [time_stamps_all,stamps_all(1,end)];

end
```

Figure 1 – Spike detection algorithm using amplitude and peak-to-peak distance thresholds, developed with MATLAB software.

```
for k = 2:kmax
    figure()
    suptitle(join(['k = ',num2str(k)]))
    a = 0;
    b = 1;
    for i = 1:(size(X,2)/2)
        % idx = vector of predicted cluster indices
        [idx] = kmeans(X(:,i+a:i+i),k);
        % silhouette plot - check if the correct number of clusters is being used
        silh = silhouette(X(:,i+a:i+i),idx,'Euclidean');

        idx_all(:,b) = idx;
        mean_silh(:,b) = mean(silh);

        subplot(2,3,i)
        gscatter(X(:,i+a),X(:,i+i),idx)
        legend('off')
        % mean silh value plot
        title(join(['mean silh = ',num2str(mean(silh))]))
        hold on

        a = a+1;
        b = b+1;

    end
    hold off
    % multidimensional vector with all the idx per projection (x12) per cluster (x4)
    idx_allclusters(:,:,k-1) = idx_all;
    mean_silhall(k-1,:) = mean_silh;
end
```

Figure 2 – K-means clustering algorithm , developed with MATLAB software.

# Appendix III – Extracellular Neuronal Activity Processing and Analysis of Evoked Activity

## Semi-supervised spike sorting

Figure 1 to 3 illustrate the clustering results for the remaining tested number of clusters.

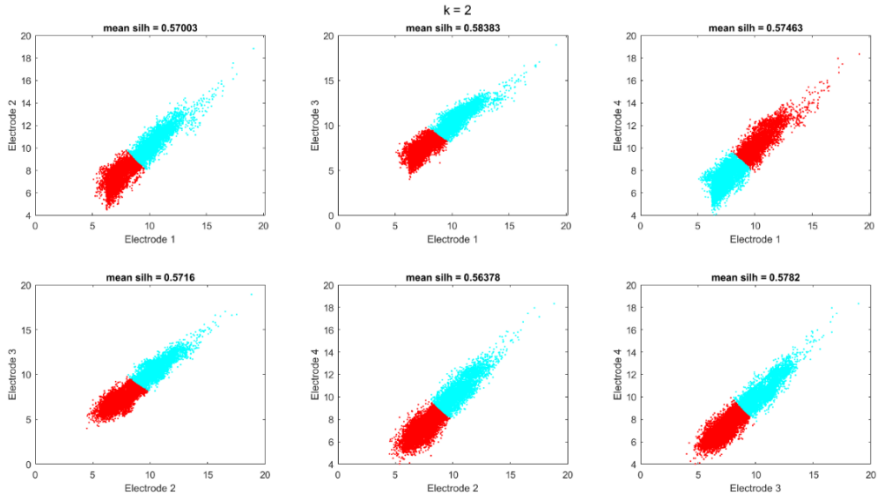


Figure 1 – K-means ($k$=2) clustering results along with the correspondent average silhouette values, visualized by plotting spike peak amplitudes recorded from pairs of electrodes of one tetrode against each other (2D projections).

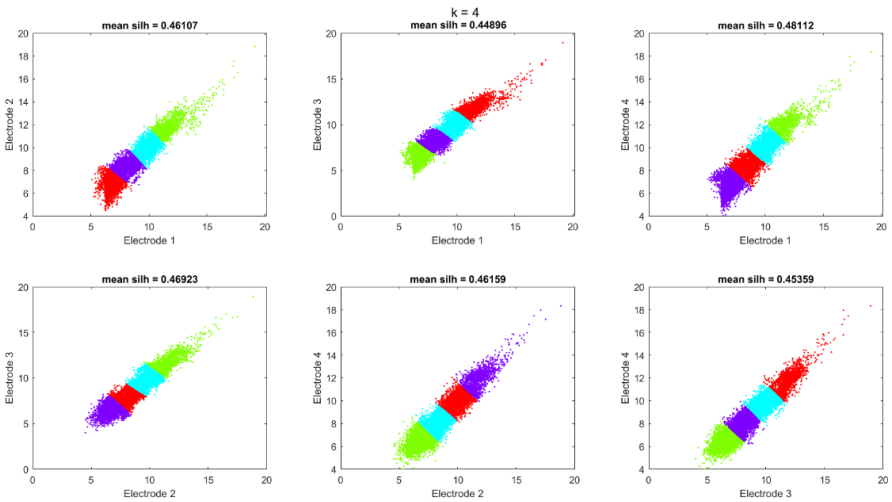


Figure 2 – K-means ($k$=4) clustering results along with the correspondent average silhouette values, visualized by plotting spike peak amplitudes recorded from pairs of electrodes of one tetrode against each other (2D projections).

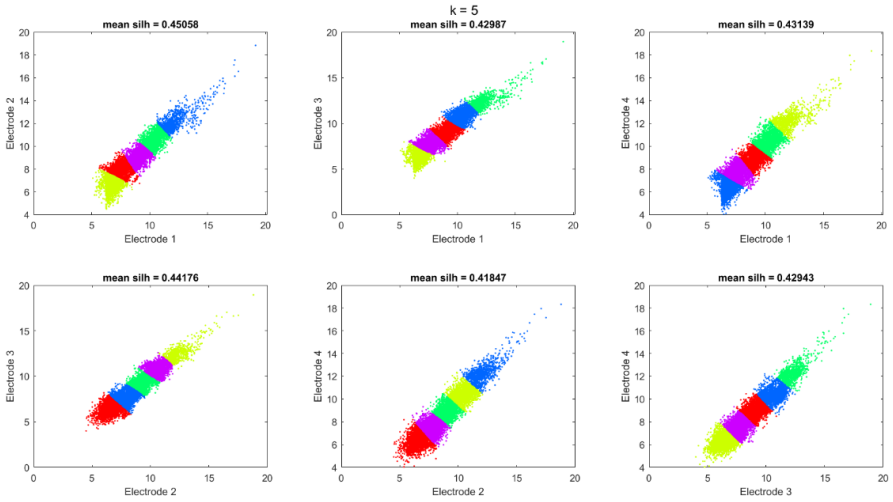


Figure 3 – K-means ($k$=5) clustering results along with the correspondent average silhouette values, visualized by plotting spike peak amplitudes recorded from pairs of electrodes of one tetrode against each other (2D projections).

An automated spike detection and sorting of extracellular activity in hippocampal coronal brain slices was also performed using the open-source toolbox "WaveClus" as to compare the previously obtained results and to validate the new semi-supervised algorithm developed in this dissertation. As displayed in Figure 4, a higher amount of single-units were separated in comparison to the ones obtained with the semi-supervised spike sorting algorithm. Yet many of these potential neurons ("cluster 2", "cluster 6", "cluster 7" and "cluster 8") were dismissed as a result of their waveforms which were contaminated with overlapping spikes. This may be a result of the simultaneous firing of distinct single units, resulting in the alteration of the cluster's waveform by the action potential of other neurons (overlapping spikes).

The single-unit activity of the selected clusters is illustrated in Figure 5 to 8. The single unit classified as cluster 5 presented a similar activity to the one isolated with the semi-supervised spike sorting algorithm created in the current work, changing from a baseline activity with a mean firing rate of approximately 20 Hz to an activity approximately above 30 Hz upon opto stimulation.

By comparing all the isolated single units' activity, the neurons assigned to cluster 3 and 4 where the ones the highest response to opto stimulation, changing from a baseline activity with a mean firing rate near to 0 Hz to an activity of 20 Hz and 10 Hz, respectively. Moreover, after stimulation the neurons become less excitable and returned to their baseline activity of a firing mean rate near to 0 Hz and thus, the delivered light pulses were able to evoke the activity of silent neuronal cells. This was also visualized though the raster plots of the spike events at each stimulation trial, which were almost absent before and

after opto stimulation. The remaining units (cluster 1 and cluster 5) did not displayed such strong modulation effects, being characterized by mean firing rates of approximately 60 Hz and 20-40 Hz.

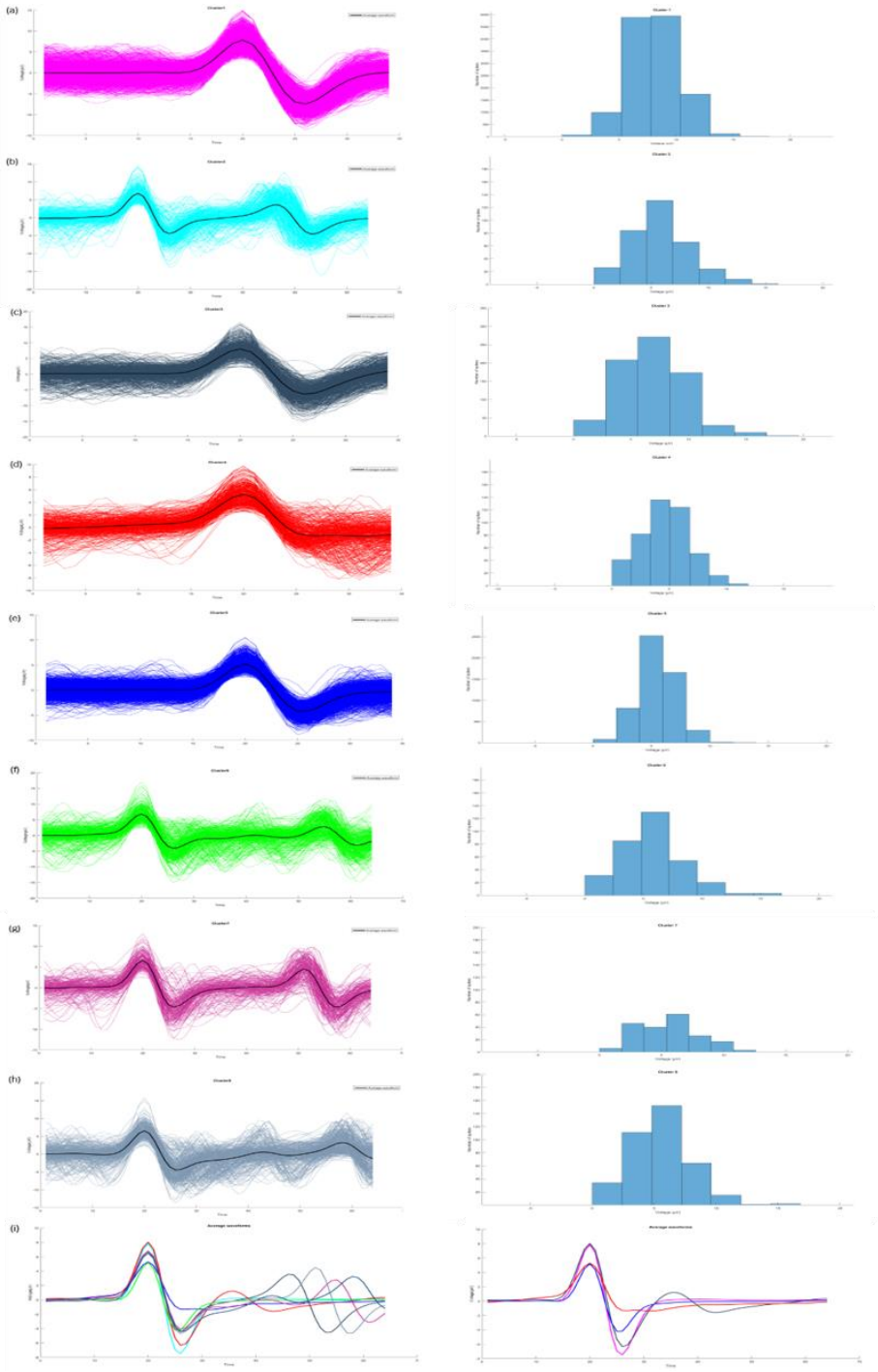

Figure 4 – Wave shapes of all detected spikes of each separated cluster obtained through Wave Clus clustering of extracellular activity with optogenetic stimulation (4 stimulation trials with a duration of 10 s each) in cerebellar slices (the x- and y-axis were differentially adjusted for visualization purposes). (a) – Cluster 1. (b) – Cluster 2. (c) – Cluster 3. (d) – Cluster 4. (e) – Cluster 5. (f) – Cluster 6. (g) – Cluster 7. (h) – Cluster 8. (i) – Average wave shape of all the separated clusters.

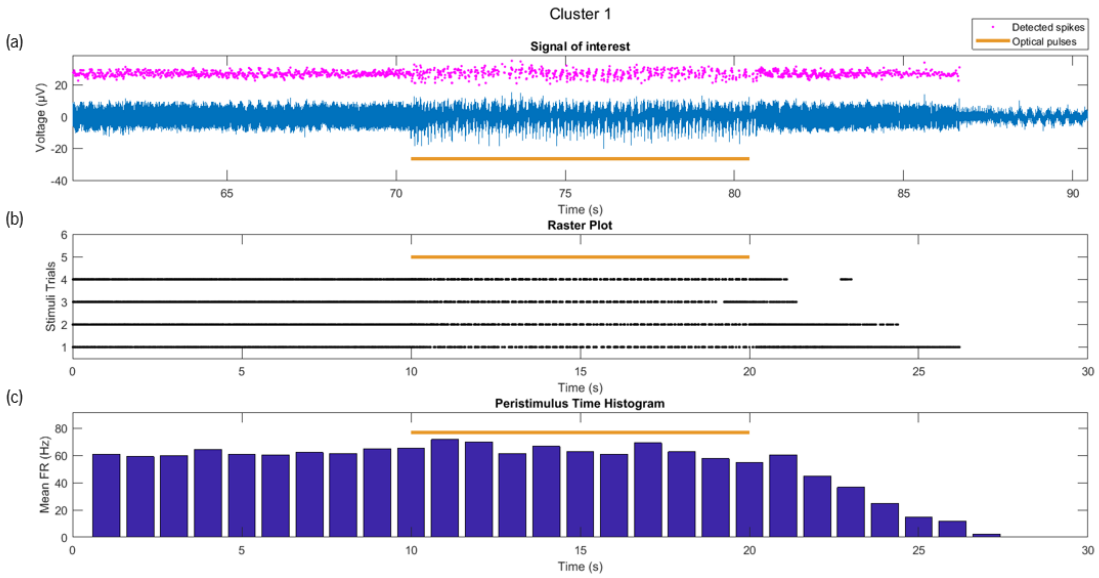


Figure 5 - Single-unit activity of the neuron correspondent to cluster 1, obtained through Wave Clus clustering of extracellular activity with optogenetic stimulation in cerebellar brain slices within a 30 s time window. (a) – Raw signal with the detected spikes. (b) – Raster plot of the neuron's activity. (c) – Peristimulus Time Histogram (PSTH) of the neuron's activity.

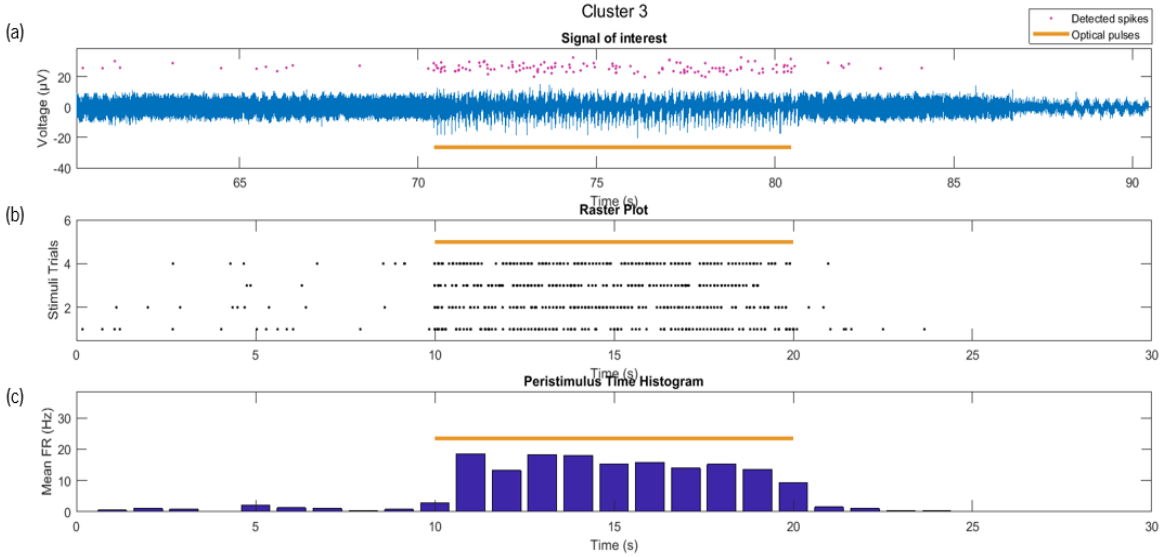


Figure 6 - Single-unit activity of the neuron correspondent to cluster 3, obtained through Wave Clus clustering of extracellular activity with optogenetic stimulation in cerebellar brain slices within a 30 s time window. (a) – Raw signal with the detected spikes, (b) – Raster plot of the neuron's activity. (c) – Peristimulus Time Histogram (PSTH) of the neuron's activity.

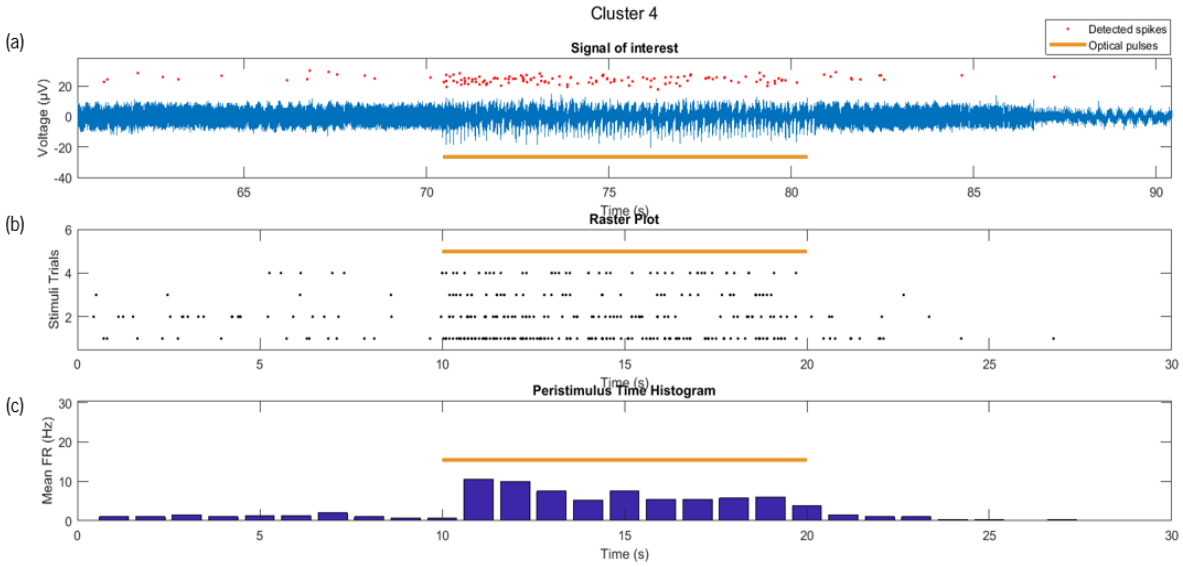


Figure 7 - Single-unit activity of the neuron correspondent to cluster 4, obtained through Wave Clus clustering of extracellular activity with optogenetic stimulation in cerebellar brain slices within a 30 s time window. (a) – Raw signal with the detected spikes. (b) – Raster plot of the neuron's activity. (c) – Peristimulus Time Histogram (PSTH) of the neuron's activity.

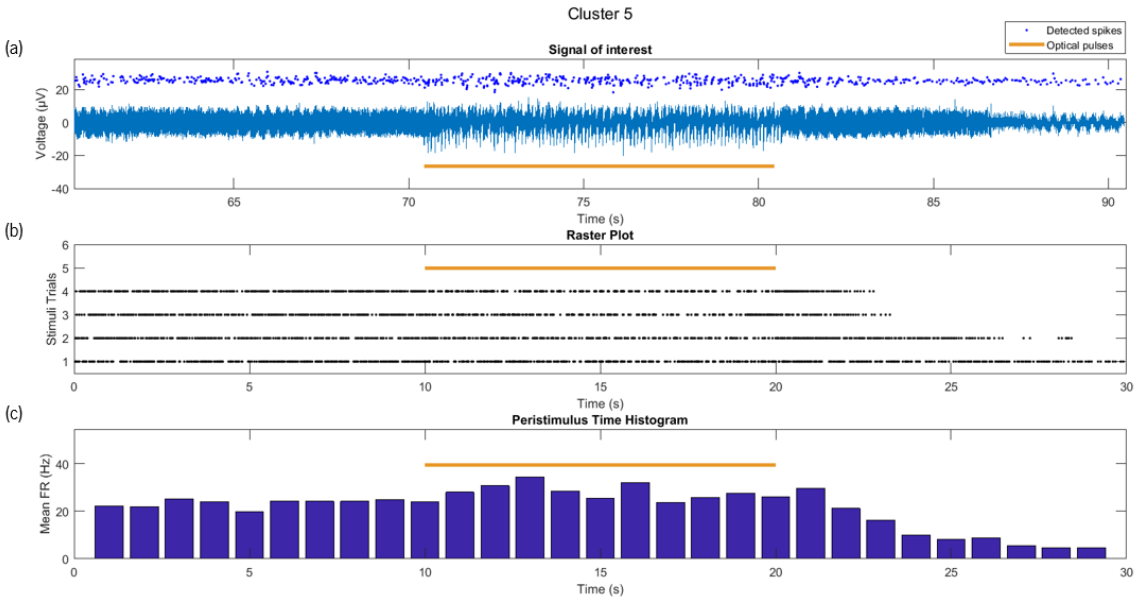


Figure 8 - Single-unit activity of the neuron correspondent to cluster 5, obtained through Wave Clus clustering of extracellular activity with optogenetic stimulation in cerebellar brain slices within a 30 s time window. (a) – Raw signal with the detected spikes. (b) – Raster plot of the neuron's activity. (c) – Peristimulus Time Histogram (PSTH) of the neuron's activity.

# Appendix IV – Extracellular Neuronal Activity Processing and Analysis of Spontaneous Activity

After spike detection, the spontaneous multi-unit activity in hippocampal brain slices was analyzed through temporal raster plots, which show the time distribution of spiking activity. Furthermore, the firing rate (Hz) of the neuronal population was evaluated through time histograms, which show the binned spike count per unit time (1 second). This analysis was conducted in both the hippocampus and habenula regions of coronal brain slices, illustrated in Figure 1 and 2 (respectively).

Though having higher peak amplitudes, the hippocampus brain region showed a lower frequency activity in comparison to the habenula brain region, as displayed in the raster plots of both figures.

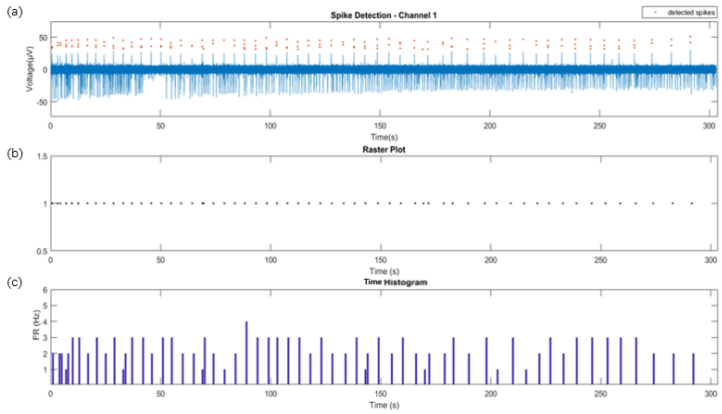


Figure 1 – Multi-unit activity in hippocampal brain slices within a 300 s time window of a single channel of the recording tetrode. (a) – Raw signal with the detected spikes. (b) – Raster plot of the detected spikes, (c) – Firing rate histogram of spiking activity.

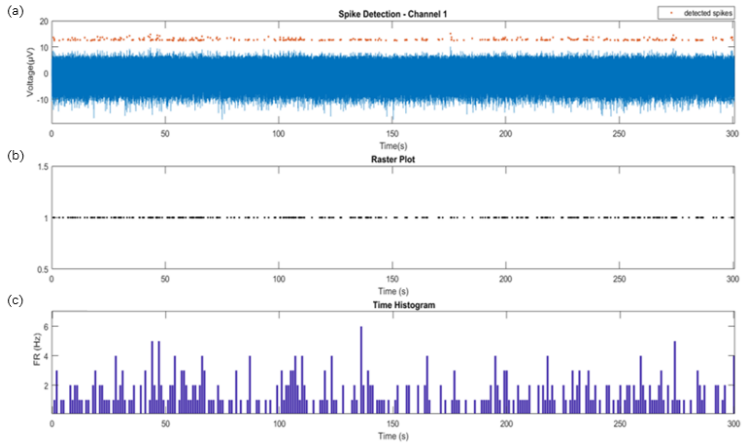


Figure 2 – Multi-unit activity in the habenula region of hippocampal brain slices within a 300 s time window of a single channel of the recording tetrode. (a) – Raw signal with the detected spikes. (b) - Raster plot of detected spikes. (c) – Firing rate histogram of spiking activity.

### Semi-supervised spike sorting

Figure 3 displays the partition results for the selected optimal number of clusters, $k$ = 2 (average silhouette value of approximately 0.67), in the present example. The clustering results for the remaining tested number of clusters are illustrated in Figures 4 to 6.

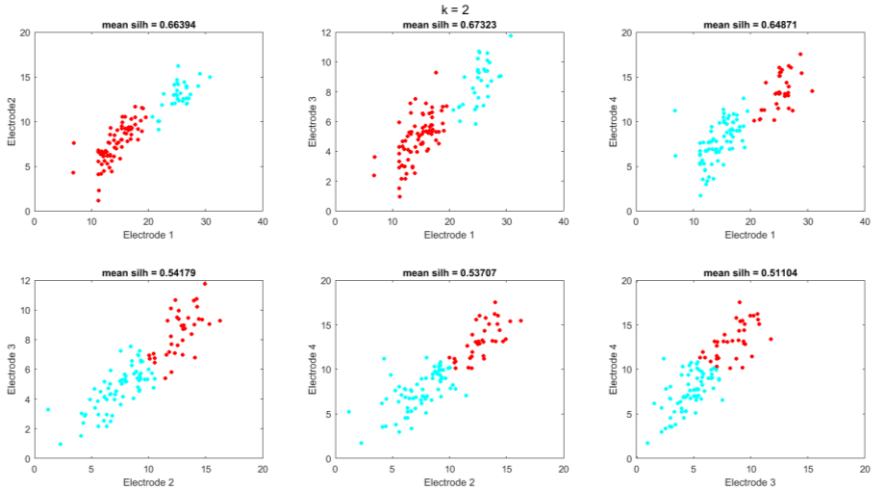


Figure 3 - K-means ($k$=2) clustering results along with the correspondent average silhouette values, visualized by plotting spike peak amplitudes recorded from pairs of electrodes of one tetrode against each other (2D projections).

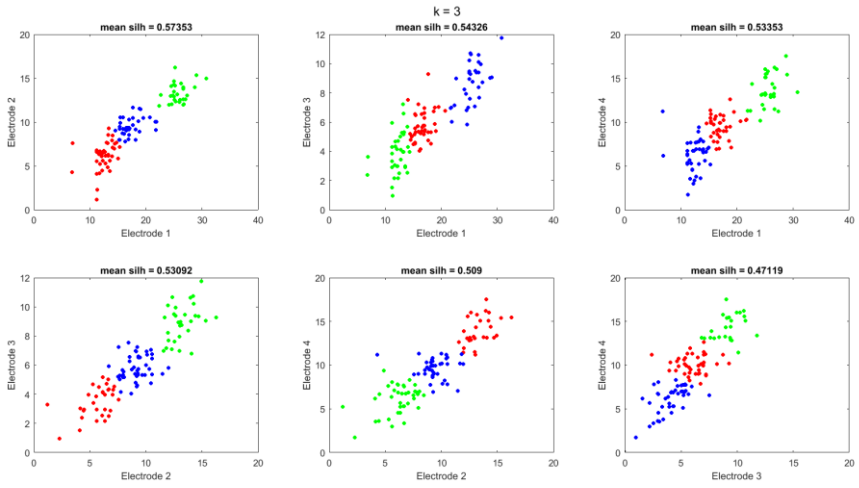


Figure 4 – K-means ($k$=3) clustering results along with the correspondent average silhouette values, visualized by plotting spike peak amplitudes recorded from pairs of electrodes of one tetrode against each other (2D projections).

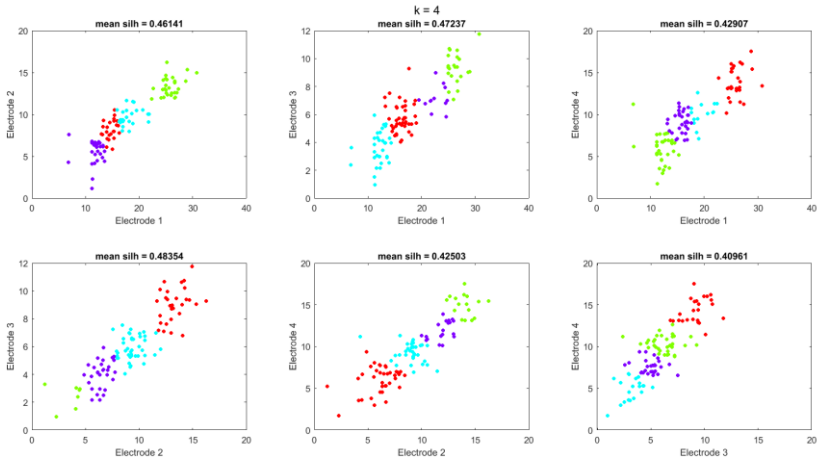


Figure 5 – K-means ($k$=4) clustering results along with the correspondent average silhouette values, visualized by plotting spike peak amplitudes recorded from pairs of electrodes of one tetrode against each other (2D projections).

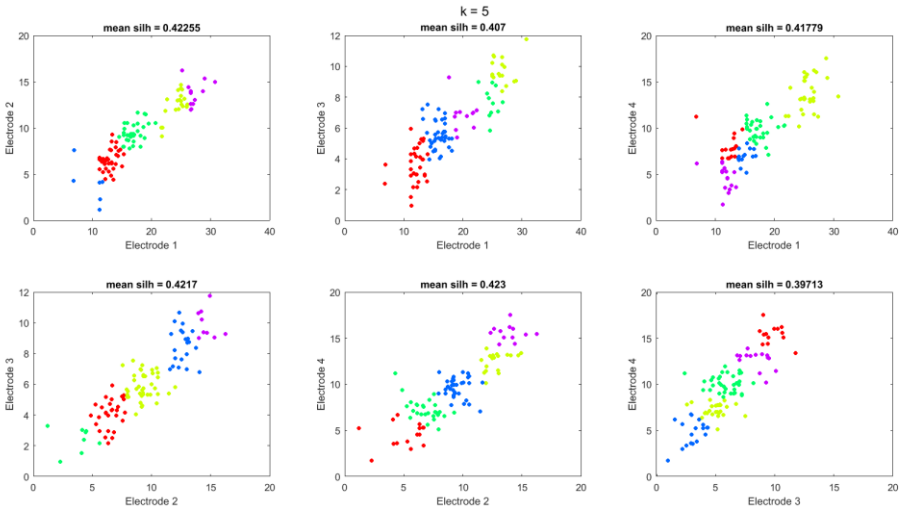


Figure 6 – K-means ($k$=5) clustering results along with the correspondent average silhouette values, visualized by plotting spike peak amplitudes recorded from pairs of electrodes of one tetrode against each other (2D projections).

The use of tetrodes with four recording channels instead of one recording electrode allows the inference of the spatial distribution of the isolated neurons in relation to the tetrode's electrodes, considering that the amplitude of the recorded spike decays rapidly as a function of distance between the electrode and the spiking neuron. Therefore, the spikes' time localization in one of the tetrode's channels (Figure 7) as well as the corresponding spike traces of each individual cluster in all the four electrodes (Figure 8) were analyzed. As illustrated in Figure 8, these spikes presented different amplitudes on each channel. Given that electrode A recorded the highest spike amplitudes, this means that both spiking

neurons (red and blue) were spatially closer to electrode A compared to the other recording electrodes. Electrode C had the lowest amplitudes and thus, was the furthest away from the neurons with action potential activity. The remaining signal (light grey) represents background activity (activity of close neurons which could not be classified and thus associated to the MUA.

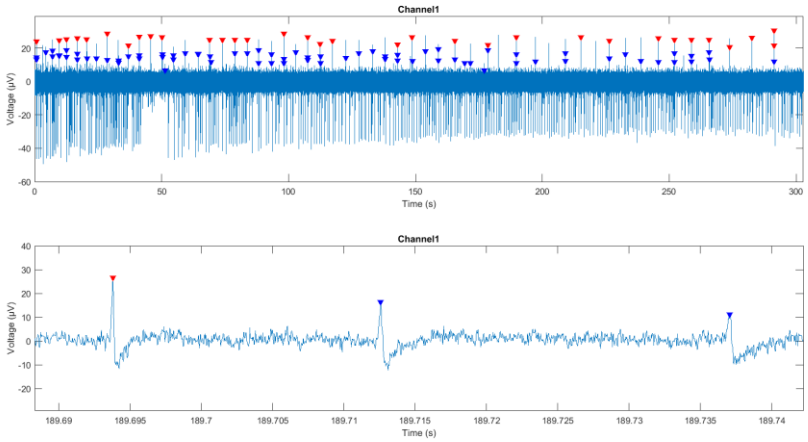


Figure 7- Spikes' time for each separated cluster, obtained through semi-supervised spike sorting of spontaneous extracellular activity in hippocampal brain slices. Each cluster is represented in a different color.

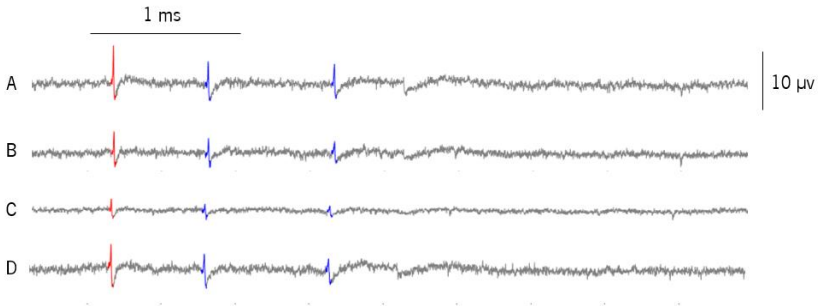


Figure 8 – Representative single-unit activity of the two neurons correspondent to cluster 1 (blue) and 2 (red) in the four channels of the recording tetrode, obtained through semi-supervised spike sorting of spontaneous activity in hippocampal brain slices. (A) – Tetrode's channel one. (b) – Tetrode's channel two. (C) – Tetrode's channel three. (D) – tetrode's channel four.

After spike sorting and clustering, each individual cluster was examined in terms of its spike waveforms and the distribution of the peak amplitudes (histogram). As observed in Figure 9, the neuron classified as cluster 1 presented a few spikes which were incorrectly attributed, as confirmed not only by the visual inspection of the waveforms that greatly deviate from the average waveform but also by the distribution of the spikes' amplitude that resulted in a bimodal histogram distribution.

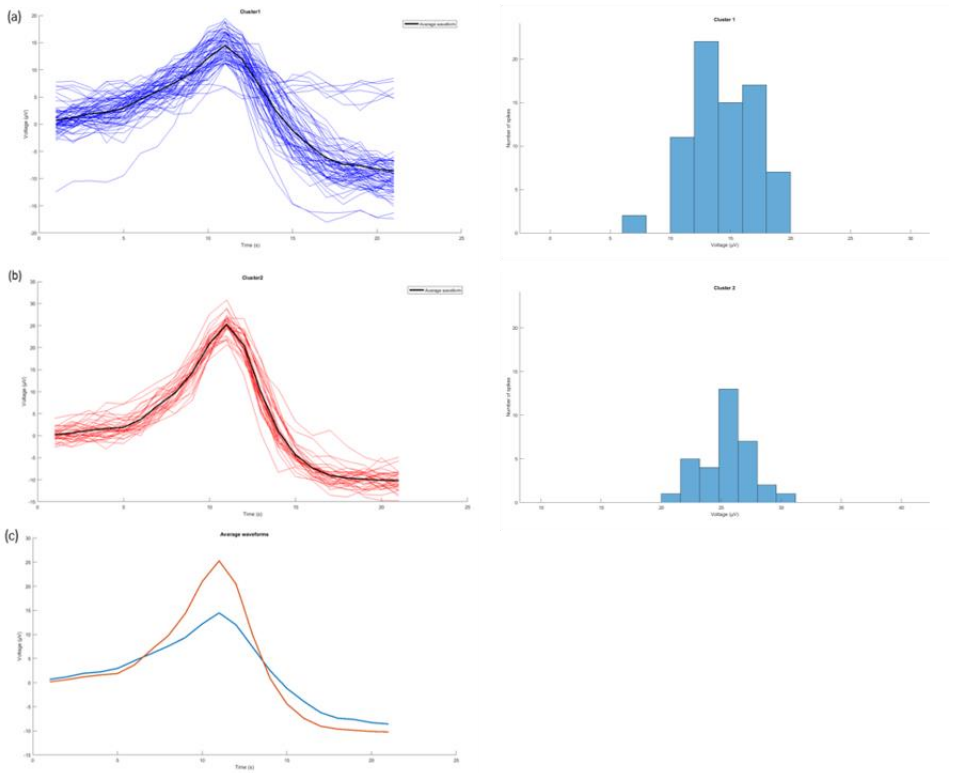


Figure 9 - Waveforms of all detected spikes of each separated cluster through semi-supervised spike sorting of spontaneous extracellular activity in hippocampal brain slices and correspondent amplitude histograms (the x- and y-axis were differentially adjusted for visualization purposes). (a) – Cluster 1. (b) – Cluster 2. (c) – Average wave shape of all the separated clusters.

Lastly, the single-unit activity of each classified cluster is showed in Figure 10 and 11, with the corresponding raster plot of its action potential activity and firing rate time histograms.

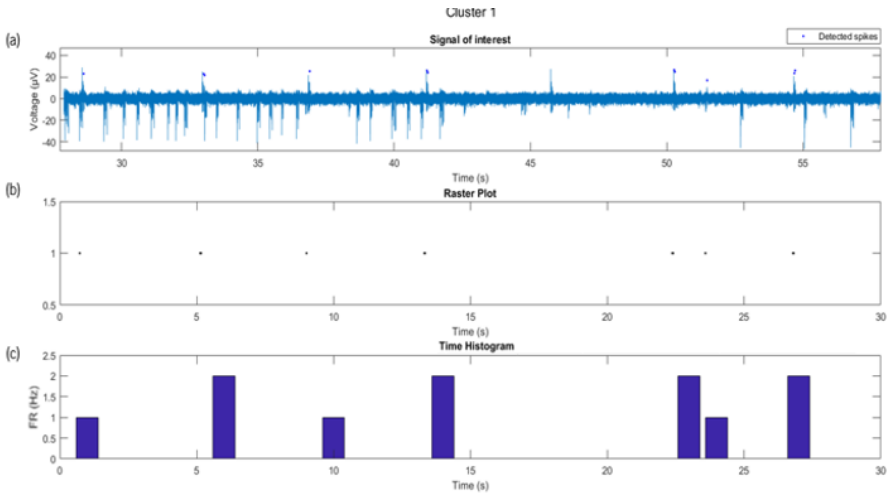


Figure 10 - Single-unit activity of the neuron correspondent to cluster 1, obtained through semi-supervised spike sorting of spontaneous activity in hippocampal brain slices within a 30 s time window. (a) – Raw signal with the detected spikes indicated by blue arrows. (b) – Raster plot of the neuron's activity. (c) – Firing rate histogram of the neuron's activity.

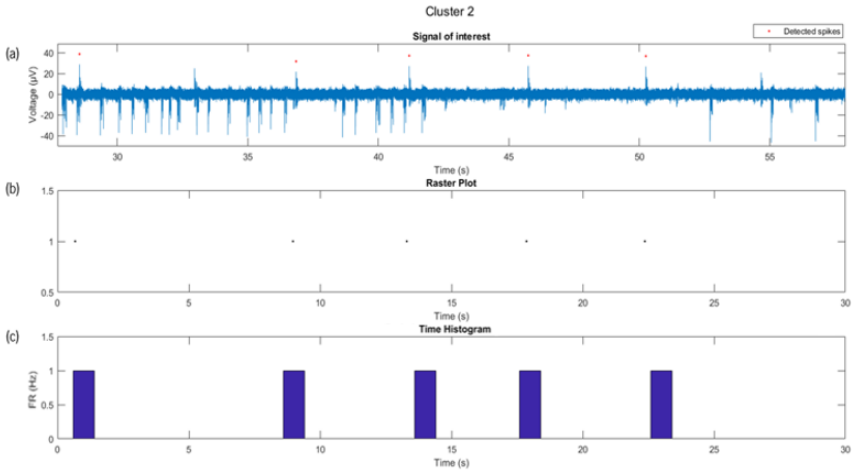


Figure 11 - Single-unit activity of the neuron correspondent to cluster 1, obtained through semi-supervised spike sorting of spontaneous activity in hippocampal brain slices within a 30 s time window. (a) – Raw signal with the detected spikes indicated by red arrows. (b) – Raster plot of the neuron's activity. (c) – Firing rate histogram of the neuron's activity.

To again validate the results obtained with our newly developed semi-supervised spike sorting algorithm, automated spike detection and sorting was also conducted using the toolbox "WaveClus".

As seen in Figure 12 and 13, several clusters were separated in comparison to the ones obtained with the semi-supervised spike sorting algorithm. However, many of these potential single units were discarded due to their waveforms which were corrupted with spikes wrongly classified ("cluster 3") and also due to their abnormal shape not compatible with an action potential shape ("cluster 1", "cluster 2"). The neurons isolated as cluster 4 and 6 presented similar waveforms as well as single-unit activity firing rates (Figure 14 and 15) similar to the ones obtained with the sorting algorithm developed in this dissertation.

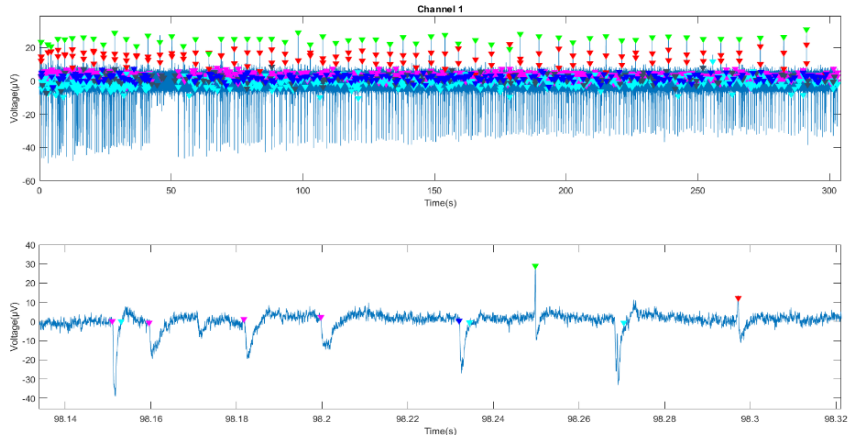


Figure 12 – Spikes' time for each separated cluster obtained through Wave Clus clustering of spontaneous extracellular activity of hippocampal brain slices. Each cluster is represented in a different color.

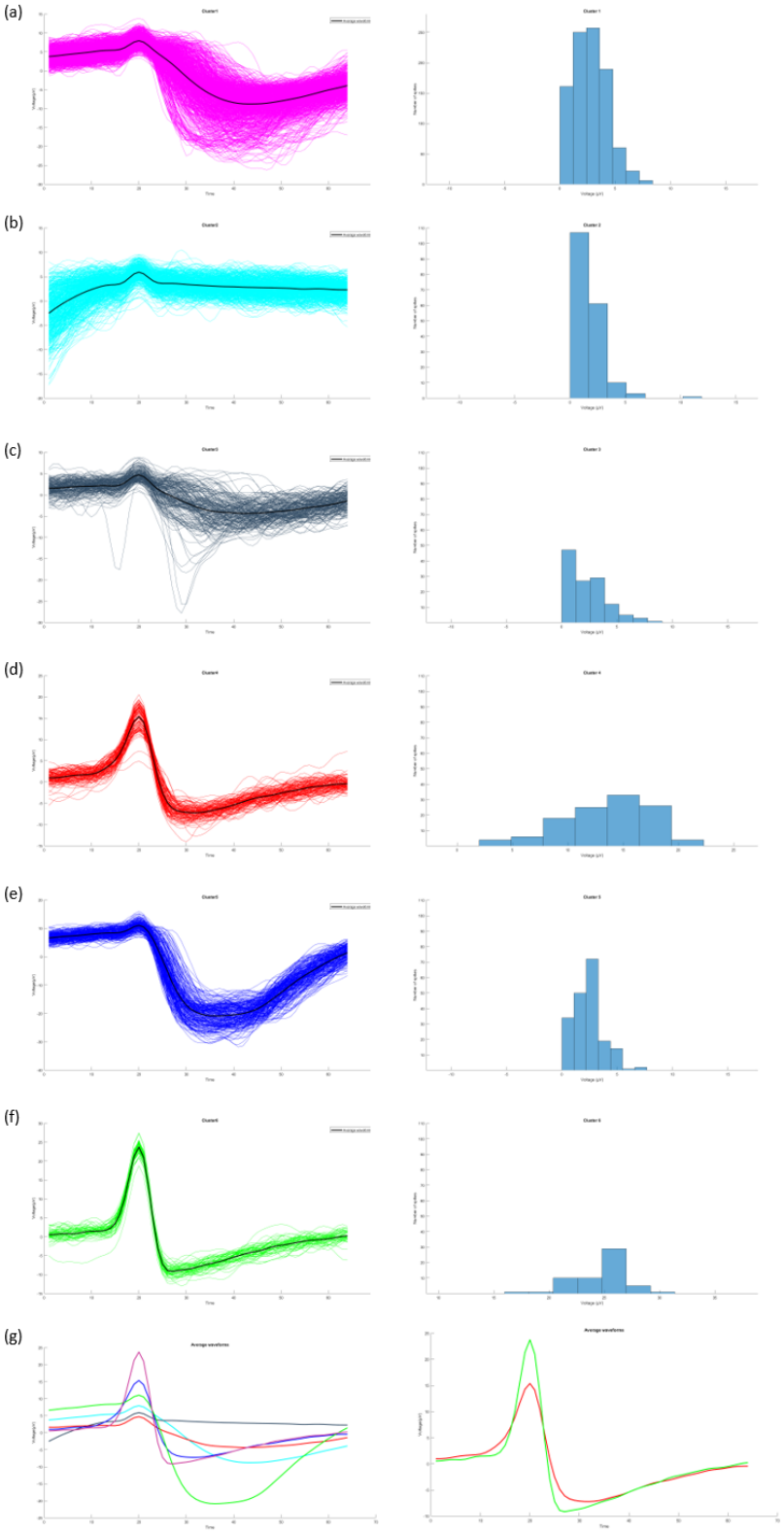


Figure 13 - Waveforms of all detected spikes of each separated cluster obtained through Wave Clus clustering of spontaneous extracellular activity in hippocampal brain slices and correspondent amplitude histograms (the xx and yy-axis were differentially adjusted for visualization purposes). (a) – Cluster 1. (b) – Cluster 2. (c) – Cluster 3. (d) – Cluster 4. (e) – Cluster 5. (f) – Cluster 6. (g) – Average waveforms of all the separated clusters (on the right are the average waveforms of the clusters selected as single-neurons in supervised manner).

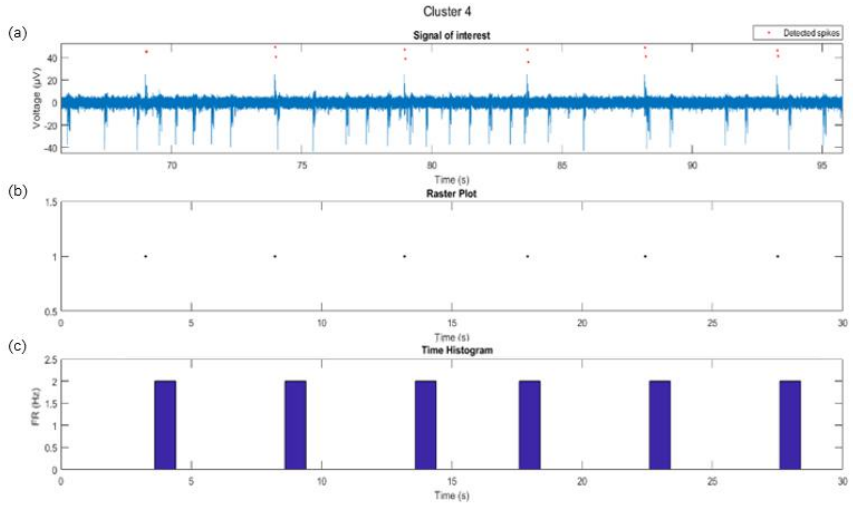


Figure 14– Single-unit activity of the neuron correspondent to cluster 4, obtained through Wave Clus clustering of spontaneous extracellular activity in hippocampal brain slices within a 30 s time window. (a) – Raw signal with the detected spikes. (b) – Raster plot of the neuron's activity. (c) – Firing rate histogram of the neuron's activity.

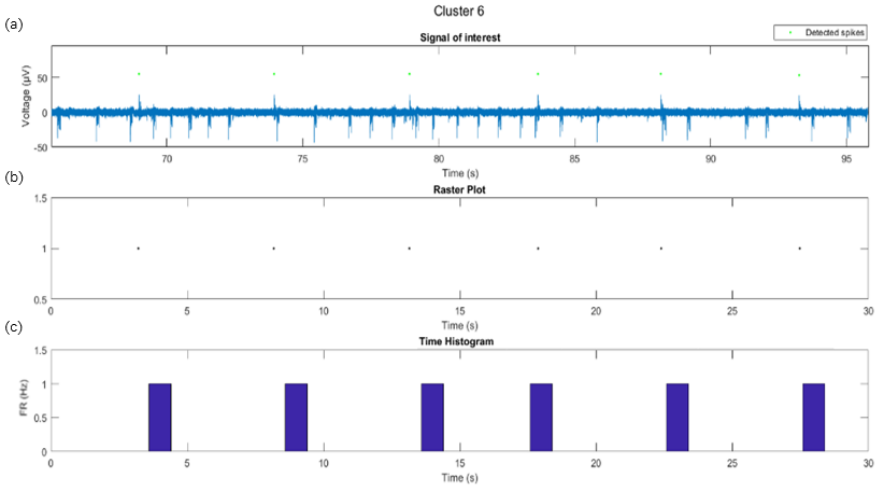


Figure 15 – Single-unit activity of the neuron correspondent to cluster 6, obtained through Wave Clus clustering of spontaneous extracellular activity in hippocampal brain slices within a 30 s time window. (a) – Raw signal with the detected spikes. (b) – Raster plot of the neuron's activity. (c) – Firing rate histogram of the neuron's activity.